Unclassified

AEDC-TR-79-54

ARCHIVE COPY
DO NOT LOAN

C-1

Experimental Study of the Plume Characteristics of a New Monopropellant Hydrazine Thruster

W. D. Williams, T. D. McCay, H. M. Powell,
and J. W. L. Lewis
ARO, Inc.

January 1980

Final Report for Period October 1,1977 — September 30, 1978

DOC_NUM SER CN
UNC30506-PDC A 1

Approved for public release; distribution unlimited.

Property of U. S. Air Force
AEDC LIBRARY
F40600-77-C-0003

AEDC TECHNICAL LIBRARY
5 0720 00034 4020

ARNOLD ENGINEERING DEVELOPMENT CENTER
ARNOLD AIR FORCE STATION, TENNESSEE
AIR FORCE SYSTEMS COMMAND
UNITED STATES AIR FORCE

Unclassified

Unclassified

NOTICES

When U. S. Government drawings, specifications, or other data are used for any purpose other than a definitely related Government procurement operation, the Government thereby incurs no responsibility nor any obligation whatsoever, and the fact that the Government may have formulated, furnished, or in any way supplied the said drawings, specifications, or other data, is not to be regarded by implication or otherwise, or in any manner licensing the holder or any other person or corporation, or conveying any rights or permission to manufacture, use, or sell any patented invention that may in any way be related thereto.

Qualified users may obtain copies of this report from the Defense Technical Information Center.

References to named commerical products in this report are not to be considered in any sense as an indorsement of the product by the United States Air Force or the Government.

This report has been reviewed by the Office of Public Affairs (PA) and is releasable to the National Technical Information Service (NTIS). At NTIS, it will be available to the general public, including foreign nations.

APPROVAL STATEMENT

This report has been reviewed and approved.

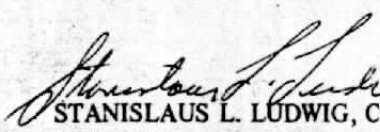

STANISLAUS L. LUDWIG, Captain (CF)
Project Manager
Directorate of Test Engineering

Approved for publication:

FOR THE COMMANDER

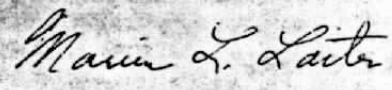

MARION L. LASTER
Director of Technology
Deputy for Operations

REPORT DOCUMENTATION PAGE		READ INSTRUCTIONS BEFORE COMPLETING FORM
1 REPORT NUMBER AEDC-TR-79-54	2 GOVT ACCESSION NO.	3 RECIPIENT'S CATALOG NUMBER
4 TITLE (and Subtitle) EXPERIMENTAL STUDY OF THE PLUME CHARACTERISTICS OF A NEW MONOPROPELLANT HYDRAZINE THRUSTER		5 TYPE OF REPORT & PERIOD COVERED Final Report-October 1, 1977 - September 30, 1978 6 PERFORMING ORG. REPORT NUMBER
7 AUTHOR(s) W. D. Williams, T. D. McCay, H. M. Powell, and J. W. L. Lewis, ARO, Inc., a Sverdrup Corporation Company		8 CONTRACT OR GRANT NUMBER(s)
9 PERFORMING ORGANIZATION NAME AND ADDRESS Arnold Engineering Development Center/DOT Air Force Systems Command Arnold Air Force Station, Tennessee 37389		10 PROGRAM ELEMENT, PROJECT, TASK AREA & WORK UNIT NUMBERS Program Element 62302F
11 CONTROLLING OFFICE NAME AND ADDRESS Arnold Engineering Development Center/DOS Air Force Systems Command Arnold Air Force Station, Tennessee 37389		12 REPORT DATE January 1980 13 NUMBER OF PAGES 117
14 MONITORING AGENCY NAME & ADDRESS(if different from Controlling Office)		15 SECURITY CLASS (of this report) UNCLASSIFIED 15a DECLASSIFICATION/DOWNGRADING SCHEDULE N/A

16 DISTRIBUTION STATEMENT (of this Report)

Approved for public release; distribution unlimited.

17 DISTRIBUTION STATEMENT (of the abstract entered in Block 20, if different from Report)

18 SUPPLEMENTARY NOTES

Available in Defense Technical Information Center (DTIC)

19 KEY WORDS (Continue on reverse side if necessary and identify by block number)

exhaust plumes	high vacuum	Rayleigh scattering
hydrazine	vacuum chambers	gas dynamics
liquid rocket propellants	mass spectrometers	physical properties
monopropellants	lasers	temperature
thrusters	Raman spectroscopy	mass

20 ABSTRACT (Continue on reverse side if necessary and identify by block number)

An experimental study of the exhaust plume of a 0.44-N (0.1-lbf), hydrazine monopropellant thruster with a refurbished catalyst bed has been performed to characterize both the gas-dynamic and contamination properties of the vacuum plume expansion. The thruster was operated in a high-vacuum chamber over a thrust range of 0.44 to 1.10 N (0.1 to 0.25 lbf) with a nominal 0.14-sec-on/9.86-sec-off duty cycle using initial catalyst bed temperatures

DD FORM 1 JAN 73 1473 EDITION OF 1 NOV 65 IS OBSOLETE

19. KEY WORDS (Continued)

deposition
particulates

20. ABSTRACT (Continued)

of 367 and 478°K (200 and 400°F. The exhaust plume diagnostic systems employed included a mass spectrometer probe, a quartz crystal microbalance (QCM), and a laser Raman/Rayleigh scattering system. These systems determined plume species number densities and temperatures, mass deposition rates, and the level of particulates in the plume. Traditional engine performance parameters were also determined in order to relate performance and exhaust plume properties.

AFSC
Arnold AFS Tenn

PREFACE

The work reported herein was conducted by the Arnold Engineering Development Center (AEDC), Air Force Systems Command (AFSC), for both the Air Force Rocket Propulsion Laboratory (AFRPL), AFSC, and NASA Jet Propulsion Laboratory (JPL). The results of the research were obtained by ARO, Inc., AEDC Division (a Sverdrup Corporation Company), operating contractor for the AEDC, AFSC, Arnold Air Force Station, Tennessee, under ARO Project No. V34S-R9A. Lieutenant Eric Lund was the project manager for AFRPL, Mr. Ken Baerwald, Jr., was the project manager for JPL, and Captain Stanislaus L. Ludwig (CF) was the Air Force project manager at AEDC. The data analysis was completed on September 21, 1978, and the manuscript was submitted for publication on June 6, 1979.

CONTENTS

ILLUSTRATIONS

Figure

Figure Page

Figure | Page

Figure Page

TABLES

1.0 INTRODUCTION

During Fiscal Year 1977, a multiple diagnostic program was completed which characterized the exhaust plume of a refurbished, 0.1-lbf* monopropellant hydrazine thruster (Ref. 1). The objectives of the program were to study plume condensation effects and contamination properties. Near the end of the experimental program a phenomenon occurred that was referred to in Ref. 1 as the thruster "catastrophe." Laser scattering revealed a sufficiently high concentration of particulate matter in the plume to allow visual observation of the laser beam passing through the plume. Before the catastrophe the laser beam could not be observed. Even with quartz crystal microbalance (QCM) temperatures as high as 160°K, the mass deposition on the QCM surface was so high that saturation occurred after only a few thruster pulses. Subsequent particle sampling measurements (Ref. 1) revealed that copious amounts of raw hydrazine were in the plume. Engine performance calibrations revealed, however, that the thruster was performing almost as well as it was when engine performance calibrations were made at the beginning of the program.

Therefore, the judgement was made that the thruster "catastrophe" might prove to be extremely useful if measurements identical to those made on the aged thruster could be performed on a new thruster. The aged thruster was returned to the manufacturer, Hamilton Standard, where the catalyst bed was refurbished and calibration tests were conducted. This refurbished engine was subsequently returned to AEDC for continued experimentation. It must be emphasized that the new thruster (hereafter, referred to as the refurbished thruster) is the aged thruster; the only difference is the addition of the refurbished catalyst bed.

This report presents a description of the experiments with the new thruster. Exemplary data are presented, and comparisons are made to the refurbished thruster results and CONTAM II predictions (Ref. 2). Table 1 presents a matrix of the test conditions and data obtained during these experiments. Eight two-day test periods were required to complete the experimental study. The engine was pulsed approximately 10,650 times.

*Although the metric system of units is used in this report, several of the performance parameters of the engine are presented using engineering units. This mixture of systems is desirable because both the existing data and the computational base to which the results of this work will be compared use engineering units. The metric equivalent will be given for the first appearance of a quantity for which engineering units are desirable, but subsequent usage will be nonmetric.

2.0 DESCRIPTION OF TEST CELL, ROCKET ENGINE, AND FUEL SYSTEM

2.1 4- by 10-FT RESEARCH VACUUM CHAMBER

The thruster was contained within the 4- by 10-ft Research Vacuum Chamber (RVC), a stainless steel vacuum chamber with a blank-off pressure of approximately 1×10^{-7} torr. A mechanical pump provided rough pumping, and a diffusion pump provided intermediate pumping. Final pumping was achieved with a 20°K gaseous-helium (GHe) cryoliner with a liquid-nitrogen (LN_2) radiation shield and a 37-liter-capacity liquid-helium (LHe)-filled cryopump, also with LN_2-cooled radiation shields. The thruster was mounted on a traversing table with three linear degrees of freedom to permit stationary flow-field instrumentation. Figure 1 is a schematic of the RVC and the engine installation. Complete details of the chamber, engine installation, and chamber operational procedure may be found in Ref. 1.

2.2 THRUSTER

The thruster used in this experimental program was a Hamilton-Standard REA/CTS 10-18 monopropellant hydrazine thruster. This thruster is the same as that used in experiments described in Ref. 1 except that the catalyst bed was refurbished for the experiments reported here. In addition, the internal catalyst bed heater for this refurbished thruster was operational, whereas on the aged thruster it was inoperational, therefore requiring the use of an external heater. Unfortunately, with the thruster mounted in the cold environment of the RVC, the internal catalyst bed heater was incapable of bringing the initial catalyst bed temperature to 589°K (600°F), and this eliminated three test conditions that were used in the aged thruster experiments. Complete details of the thruster including design specifications can be found in Ref. 1.

2.3 FUEL SYSTEM

The propellant system used in these experiments was not the same as that employed for the aged thruster experiments. However, it was the same system used by the Jet Propulsion Laboratory (JPL) (Ref. 3) in contamination experiments with the thruster. As a result of stricter Air Force safety regulations, extensive modifications had to be made to this system. Figure 2 is a schematic diagram of the modified system. Preparation and operation of the system were practically the same as those described in Ref. 1 for the aged thruster. The fuel used for the present experiments came from the same drum of standard monopropellant-grade hydrazine, MIL-P-26536C, as used previously.

2.4 THRUSTER OPERATION

Normally the thruster was operated in a pulse mode with a nominal 0.14-sec-on/9.86-sec-off duty cycle and a nominal 30-pulse sequence. The prepulse catalyst bed temperature, T_{CATB}, was set at either 367°K (200°F) or 478°K (400°F), and the thruster chamber pressure, P_c, was systematically varied from 85 to 205 psia (5.78 to 13.95 atm). Table 1 should be consulted for the matrix of thruster test conditions and for their nomenclature as used throughout this report.

The only exception to pulse mode operation occurred whenever mass flow-rate measurements were made. In this case the engine was operated in a 60-sec continuous-burn mode.

3.0 DESCRIPTION OF SPECIAL DIAGNOSTIC SYSTEMS

3.1 LASER SYSTEM

The experimental arrangement for all special diagnostic instrumentation is shown schematically in Fig. 3. The thruster plume flow is into the plane of the figure. An electron beam system is shown mounted in the RVC instrumentation spoolpiece, but it was not used in these experiments. The laser system is shown mounted at 45 degrees from the top. The laser was a Holobeam 620 series, pulsed ruby system which was used to provide excitation for Raman and Rayleigh/Mie scattering. A 15.2- by 1.3-cm (6- by 1/2-in.) ruby rod was used to provide a horizontally polarized beam; the laser was operated in the conventional mode that provided a pulse width of 1 msec and an energy of 70 J per pulse at 6,943 Å. After expansion in the ratio 3:1, the laser beam was focused by a 1,000-mm-focal-length lens onto the thruster axial centerline.

Behind the laser an energy monitor system was installed to correct the scattered-light intensity for laser energy variations. Essentially the same system was used as was used previously (Ref. 1), but the photodiode detector was replaced with a 1P28 photomultiplier tube. The photomultiplier provided a larger detector area which permitted more realistic determination of laser energy variation. Additional neutral density filtering had to be used, of course, to prevent saturation of the photomultiplier tube.

Beam alignment procedure as well as more details on the laser system may be found in Ref. 1.

3.2 SPECTROMETER SYSTEM

Light collection for the laser scattering system was provided by a 7.6-cm (3-in.)-diam, 30.5-cm (12-in.)-focal-length lens mounted on an optical rail inside the RVC. The lens was located approximately 30.5 cm (12 in.) from the axial centerline of the RVC and provided a nearly collimated light beam out to the imaging lens which was 7.6 cm (3 in.) in diameter and 50.8 cm (20 in.) in focal length. The image of the laser beam focal volume was positioned on the entrance slit of the spectrometer, and an iris aperture was adjusted to obtain a 2.75-mm-long laser beam. (The slit width was always set at 1.0 mm.) The spectrometer was a 0.5-m-focal-length double spectrometer, the same instrument used during the aged thruster experiments. Detection of the laser scattered radiation was made with a cooled RCA® C31034A photomultiplier tube. At -26°C and with 2,200 v DC, the dark count rate of the tube and Ortec photon-counting system was approximately 90 counts per second. The photon-counting electronics used for processing the Raman signals were the same as those of Ref. 1. Whenever the Rayleigh scattered intensities were monitored, an amplifier/gated integrator system was used to process the signals from the PMT. Additionally, neutral density filters and a sheet of HN22 Polaroid®, oriented for passage of horizontally polarized light, were placed in the collection optics system between the two lenses. Further details of the spectrometer system may be found in Ref. 1.

3.3 MASS SPECTROMETER SYSTEM

The cryogenically pumped mass spectrometer system used in these experiments was the same as that used for the refurbished thruster measurements (Ref. 1). The only mechanical change involved a different valving arrangement that was added for the present experiments to improve CO_2 addition to the probe. The probe was accurately aligned on the thruster axial centerline at a distance of 26.7 cm (10.5 in.) from the thruster exit plane when the thruster was in the axial zero position. Alignment, calibration, and operation of the mass spectrometer system are described in Ref. 1.

The data acquisition system for the mass spectrometer was improved to permit intrapulse sampling over a larger mass range than was previously possible and to permit digital acquisition (as opposed to the analog, oscillograph method that was used for the aged thruster measurements).

3.4 QUARTZ CRYSTAL MICROBALANCE

A QCM was used to determine mass deposition rates on a cryogenic surface. The experimental configuration for the QCM is shown in Fig. 4. In all test periods except the

last, the QCM was positioned so that the crystal surface was 38.7 cm (15.25 in.) from the center of the thruster exit plane, at an angle of 30 deg from the chamber centerline when the thruster axis was coincident with the chamber centerline with the thruster located in the foremost (or axial zero) position. During the last test period the QCM was repositioned so that the surface was 38.7 cm (15.5 in.) from the exit plane and so that the QCM surface was at a 42-deg angle from the thruster axis with the thruster in the axial zero position.

Cooling was provided by thermal contact with the RVC GHe cryoheader. The QCM resistance heaters, controlled by the thermocouple at the crystal surface, maintained the unit operating temperature.

Both the operational principle and operation of the QCM have been discussed in detail in Ref. 1, and data acquisition and reduction techniques were exactly the same as those used for the experiments of Ref. 1. It should be noted, however, that the QCM used in the present experiments was not the same as that used for the aged thruster. Differences in calibration constants were unknown; therefore, all data have been reduced using the calibration constant employed for the aged thruster results.

4.0 PRESENTATION AND DISCUSSION OF DATA

4.1 RAMAN/RAYLEIGH DATA

The local species number densities of N_2, NH_3, and H_2, as well as the gas temperature, were measured using Raman scattering at the axial position $\hat{x} = 28.5$. Rayleigh scattering measurements were performed to detect the presence of contaminating particulates and/or condensation in the expansion flow field; these measurements span the axial range of $28.5 \leq \hat{x} \leq 280$. Although the variation of the Rayleigh scatterring with engine pulse number was observed in a few cases, most of the Rayleigh data and all of the Raman data were acquired as cumulative signals over the last 25 pulses of a 30-pulse sequence. Also, the data were acquired over a 1-msec data gate width which occurred 90 msec into the thrust interval. Consequently, the data represent an average of 25 data pulses each of which has a 1-msec time resolution. The details of the data acquisition system, data reduction procedures, and corrections applied to the experimental data are given in Ref. 1 and will not be repeated in this report.

Table 2 is a summary of the results obtained using the laser-Raman technique, and Table 3 presents the averaged results for test conditions (TC's) 2S and 2A for which complete data were obtained. Figure 5 presents both (1) the method of characteristics solution (MOCS) predicted axial variation of the temperature and number density and (2) the temperatures

and total number densities measured at the $\hat{x} = 28.5$ axial position. A more detailed discussion of the MOCS results will be presented in a later section.

The Rayleigh scattering photon rate, S_i, for molecular species, i, of number density, n_i, can be shown to be

$$S_i = K \cdot \sigma_i \cdot n_i \tag{1}$$

where σ_i is the total Rayleigh cross section for species i. The coefficient K (proportionality constant) is given by

$$K = \left(\bar{P}_o / h\nu_o\right) L \iint_{\Delta\Omega} F(\theta,\phi)\, d\Omega \Big/ \int_0^{\pi}\int_0^{2\pi} F(\theta,\phi)\, d\Omega \tag{2}$$

where $\bar{P}_o$ is the incident laser power of frequency, ν_o, which illuminates the cylindrical focal volume of length, L. The collection optics subtends at the scattering volume a solid angle, $\Delta\Omega$, at the spherical polar angles, θ and ϕ. Finally, the angular dependence of the Rayleigh differential cross section, $d\sigma/d\Omega$, has been written as $F(\theta,\phi)$; i.e.,

$$(d\sigma/d\Omega)_i = \sigma_i F(\theta,\phi) \Big/ \int_0^{\pi}\int_0^{2\pi} F(\theta,\phi)\, d\Omega \tag{3}$$

Therefore, for a gas mixture of J species

$$S = \sum_{i=1}^{J} S_i = K \sum_{i=1}^{J} n_i \sigma_i = K\, n_T \sum_{i=1}^{J} X_i \sigma_i \tag{4}$$

where the mole fraction, X_i, is defined to be n_i/n_T, and

$$n_T = \sum_{i=1}^{J} n_i$$

For a flow-field expansion with reservoir number density, n_o, S can be written as

$$S = K n_o \hat{n}_T \sum_{i=1}^{J} X_i \sigma_i \tag{5}$$

where $\hat{n}_T = n_T/n_o$, which is a calculable quantity characteristic of the expansion process.

The nondimensional Rayleigh ratio, $\hat{I}_{RY}$, is defined as

$$\hat{I}_{RY} = S/K n_o \sigma_{N_2} = \hat{n}_T \sum_{i=1}^{J} X_i \left(\sigma_i/\sigma_{N_2}\right) \tag{6}$$

so that $\hat{I}_{RY}$ is directly proportional to $\hat{n}_T$. If the chemistry of the expansion is frozen, $\sum_{i=1}^{J} X_i \sigma_i$ is a constant throughout the expansion, neglecting temperature effects of σ_i.

The coefficient K was evaluated by measuring S_{N_2} for N_2 at 285°K and 200 torr and using Eq. (1). The calibration quantities are noted with a superscript "cal" in the following equation:

$$\hat{I}_{RY} = \left(S/n_o\right)\Big/\left(S_{N_2}^{cal}/n_{N_2}^{cal}\right) \tag{7}$$

Table 4 lists the measured values of $\hat{I}_{RY}$ obtained during test period (TP) 25 at the axial position $\hat{x} = 45.2$. Figure 6 shows the relative behavior of $\hat{I}_{RY}$ for the initial three pulses of a 30-pulse sequence. These data correspond to the conditions of Table 4. The initial pulse is an order of magnitude larger in value than the average of Pulses 4 through 30. Further, by Pulse 4, the value of $\hat{I}_{RY}$ approaches a value that does not vary significantly during the remainder of the pulse train.

Table 5 presents the axial variations of $\hat{I}_{RY}$ obtained during TP 26. These data are graphed in Fig. 7. The estimated uncertainty levels for the Raman and Rayleigh scattering measurements were determined in the manner described in Ref. 1, and the results are shown in Table 6.

Comparison of the measured Rayleigh ratio, $\hat{I}_{RY}$, with the predicted value requires knowledge of the mole fractions, X_i, and the cross sections, σ_i; however, the latter set

of quantities, σ_i, is not well known. To obtain an approximate value for the set σ_i, the electronic polarizabilities, α_{ie}, were obtained using the molar refractivity, r, values of Ref. 4. By using the relations

$$\alpha_{ie} = \left(1/2\pi n_i\right)\left(\bar{n}_i - 1\right)$$

and

$$r_i = 10^6\left(\bar{n}_i - 1\right)$$

where $\bar{n}_i$ is the index of refraction of species i at frequency ν_0 and the electronic polarizability of species i, α_{ie}, was found. The Rayleigh cross section was approximated as

$$\sigma_i \propto \alpha_i^2$$

so

$$\sigma_i/\sigma_{N_2} = \left(\alpha i/\alpha N_2\right)^2$$

and Eq. (6) becomes

$$\hat{I}_{RY} = \hat{n}_T \sum_{i=1}^{J} X_i \left(\alpha i/\alpha N_2\right)^2 \tag{8}$$

The values used for the ratios of Rayleigh cross sections, σ_i/σ_{N_2}, are 0.219, 0.7185, and 1.598 for H_2, H_2O, and NH_3, respectively.

Using the Raman measurements listed in Table 2, one finds that the predicted Rayleigh ratios, $\hat{I}_{RY}$, are

Condition 2S $\quad \hat{I}_{RY} = .1.02\ \hat{n}_T$

Condition 2A $\quad \hat{I}_{RY} = 1.025\ \hat{n}_T$

so that $\hat{I}_{RY} = \hat{n}_T$ to within the uncertainties of the approximations used. Shown in Fig. 7 are the axial variations of $\hat{n}_T$ for $\gamma = 1.2$ and for $\gamma = 1.3$ as determined by an MOCS. It has been assumed for this calculation that not only is the chemistry frozen but that the specific heat ratio is also constant throughout the expansion.

Figure 7a shows that the measured values of $\hat{I}_{RY}$ exceed the predicted values by a magnitude which inncreases with increasing $\hat{x}$. For example, at $\hat{x} = 28.5$, the ratio of measured and predicted values of $\hat{I}_{RY}$ varies from 5 to 10, depending on the reservoir condition. At $\hat{x} = 300$ this ratio is about 100. A function that is applicable to condensation processes involving such a spatially dependent excess intensity is defined as (Ref. 5)

$$f = \left(\hat{I}_{RY} - \hat{n}_T\right) \Big/ \hat{n}_T \tag{9}$$

where f will depend upon the γ chosen for computing n_T. The scattering function, f, for $\gamma = 1.2$ for the expansion is shown in Fig. 7b for part of the conditions presented in Fig. 7a. The test conditions 2A and 2B not shown in Fig. 7b have scattering function, f, values intermediate to the presented cases. Both TC's 2S and 2C possess an axial coordinate dependence that rapidly increases at the lower $\hat{x}$ values and becomes asymptotic at $f = 100$ for the far-field, large $\hat{x}$ region. Using Eqs. (6) and (9), one can express f as

$$f = \sum_{i=1}^{J} X_i \left(\sigma_i \Big/ \sigma_{N_2}\right) - 1 \tag{10}$$

so that, barring composition changes in the plume expansion, f should be constant and equal to $\sum_{i=1}^{J} X_i (\sigma_i/\sigma_{N_2}) - 1$. Further, for the flow fields studied in this work, it has been shown that

$$\sum_{i=1}^{J} X_i \left(\sigma_i \Big/ \sigma_{N_2}\right) = 1.02$$

so that, allowing for uncertainty in these estimates, f should be about ± 0.1. Figure 7b shows that the experimental value of f exceeds this value by an order of magnitude at $\hat{x} = 28.5$ and increases as $\hat{x}$ increases. Furthermore, a mere redistribution of the plume composition among the species N_2, H_2, and NH_3 will not explain the results, as one can easily show using Eq. (8) and cross-section ratios. Moreover, presence of either particulate matter or raw fuel droplets is not a satisfactory or consistent explanation of the results, for if such flow-borne particulate followed the flow-field expansion, f would be approximately constant. If the

material were concentrated along the axial streamtube, f would increase continually with $\hat{x}$. Finally, vibrational relaxation in the expansion is an unsatisfactory explanation of the axial dependence of f because, quite simply, it produces the opposite effect. The most probable explanation is the presence of condensation processes in the flow field that exhibit similar axial variations of the scattering function, f. The mathematical model and the physical interpretation of such behavior for f for condensing flow fields is presented in Ref. 5.

Finally, the Rayleigh ratio $\hat{I}_{RY}$ using the results presented in Tables 4 and 5 is shown in Fig. 7c as a function of the independent variable $P_o^{2.5}/T_o^5$, and for $T_{CATB} = 478°K$, it is seen that a linear variation results. A linear regression analysis shows that

$$\hat{I}_{RY} \times 10^3 \left(T_{CATB} = 478°K\right) = 4.02 - 4.34 \times 10^{-4} \left(P_o^{2.5}/T_o^5\right) \times 10^{12}$$

for $\hat{x} = 45.2$; the units of P_o and T_o are atm and °K, respectively. The correlation coefficient for this relation is -0.994, which points up the relations good fit. The dramatic difference in the value of $\hat{I}_{RY}$ for the lower value of T_{CATB} for the lower value of $P_o^{2.5}/T_o^5$ indicates that scaling of $\hat{I}_{RY}$ using only the reservoir parameters P_o and T_o is not possible.

4.2 MASS SPECTROMETER DATA

Four plume species of primary concern (N_2, NH_3, N_2H_4, H_2O) were successfully monitored as functions of pulse number and intrapulse time for several thruster test conditions. The results are graphed in Figs. 8 through 22. The dependence of the mole fraction ratios as functions of pulse number is shown for the four thruster test conditions with initial $T_{CATB} = 400°F$ in Figs. 8 through 11. The data correspond to 0.09 sec into the thruster pulse, which is the time at which laser-Raman data were taken. Noteworthy in the data are the larger hydrazine levels in the first few pulses for each thruster case. In addition, the increased NH_3 dissociation with pulse number can be readily observed. Even though the hydrazine levels for Pulse 1 exceed those of succeeding pulses by, in some cases, an order of magnitude, the resulting contamination of hydrazine from Pulse 1 is equalled in magnitude by the cumulative effects of the subsequent two to ten engine pulses. Therefore, hydrazine contamination, as evidenced by mass spectrometric sampling, cannot be attributed primarily to an engine start-up process.

Compiled in Table 7 are ammonia-to-nitrogen mole fraction ratios for Pulses 1, 5, 10, 20, and 30 for TC's 2S, 2A, 2B, and 2C. An average ammonia-to-nitrogen ratio for these pulses is also given in Table 7.

Intrapulse species variations are presented in Figs. 12 through 19. For the TC's 2S, 2A, 2B, and 2C, variations of ammonia-to-nitrogen and hydrazine-to-nitrogen ratios are shown in Figs. 12 through 15 and 16 through 19, respectively. The data demonstrate the combination of pressure buildup and heating effects within the combustion chamber. The spikes associated with both valve opening and closing are visible for the NH_3/N_2 data. The functional behavior is directly attributable to the change in ammonia dissociation with increasing interstitial temperature. The large hydrazine spike associated with valve opening is prominent for all thruster test conditions and increases with chamber pressure. As expected, no hydrazine spike was observed with valve closing. The drastic reduction in N_2H_4 concentration with pulse number is illustrated in Figs. 16 through 19.

Because the amount of hydrazine in the plume was of significant interest, a set of pulse sequences was run in which the influences of valve inlet pressure and initial catalyst bed temperature were examined. Regardless of valve inlet pressure and initial T_{CATB}, the hydrazine levels were minimal after approximately 10 pulses. For the first few pulses, however, there was significant variation. Figure 20a demonstrates the dependence of N_2H_4 level in the plume on inlet pressure for Pulses 1 and 10. The inconsistency of the Pulse 1 data is representative of the behavior of the first pulse throughout the experiments. At higher pressure levels, the hydrazine levels of even the tenth pulse are not insignificant. Although the data are in terms of pure signal, the results can be directly interpreted in terms of level of hydrazine in the plume. Similar data in terms of N_2H_4/N_2 mole fraction ratio are given in Fig. 20b. Figure 21 demonstrates the decrease in Pulse 1 hydrazine level as the initial catalyst bed temperature is increased. The increase in hydrazine levels for "cold" starts is much more pronounced than the increase in hydrazine concentration with increasing thrust level.

The chemical reaction scheme that describes the hydrazine dissociation process can be written as

$$N_2H_4 - \frac{Y}{3}\,H_2O \rightleftharpoons \frac{H}{3}(1-X)NH_3 + \frac{1}{3}\,(1-2X)\,N_2 + 2X\,H_2 + \frac{Y}{3}\,H_2O \qquad (11)$$

where H_2O is regarded as an inert constituent and χ is the degree of dissociation for the reaction

$$NH_3 \rightleftharpoons \frac{1}{2}N_2 + \frac{3}{2}\,H_2 \qquad (12)$$

Defining ϵ to be the degree of dissociation of N_2H_4 for the reaction

$$N_2H_4 \rightleftharpoons \frac{4}{3} NH_3 + \frac{1}{3} N_2 \tag{13}$$

it is shown easily that the mole fractions of the species are given by

$$X_{N_2} = \epsilon(1+2X)/\Phi \tag{14}$$

$$X_{NH_3} = 4\epsilon(1-X)/\Phi \tag{15}$$

$$X_{N_2H_4} = 3(1-\epsilon)/\Phi \tag{16}$$

and

$$X_{H_2} = 6\epsilon X/\Phi \tag{17}$$

where

$$\Phi = 3 + 2\epsilon(1+2X) \tag{17a}$$

Ratios of the mole fractions are given by the following:

$$X_{NH_3}/X_{N_2} = 4(1-X)/(1+2X) \tag{18}$$

$$X_{H_2}/X_{N_2} = 6X/(1+2X) \tag{19}$$

$$X_{N_2H_4}/X_{N_2} = 3(1-\epsilon)/\epsilon(1+2X) \tag{20}$$

Further, the ratios of the mass spectrometric signals, which are proportional to the mole fractions of the respective species, can be used to determine both χ and ϵ. Since H_2 was not measured with the mass spectrometer, the degree of dissociation, χ, of NH_3 was determined using Eq. (18). With this value of χ, the degree of dissociation, ϵ, of N_2H_4 is determined from Eq. (20). Finally, with these experimental determinations of χ and ϵ, Eqs. (14) through (16) are used to find the mole fractions of N_2, NH_3, and N_2H_4, respectively. X_{H_2} was found using

$$\sum X_i = 1$$

where H_2O mole fraction has been neglected because of its small value.

Figures 22a through h show the results of these computations for the various engine operational conditions. Shown in Figs. 22a through h are the variations of species mole fractions with pulse number in a 30-pulse train; also shown are the degrees of dissociation of N_2H_4 and NH_3. These results clearly show the increasing values of the degrees of dissociation of both N_2H_4 and NH_3, ϵ and χ, respectively. For N_2H_4, ϵ increases from 2 to 6 percent over the 30-pulse sequence, whereas the degree of dissociation, χ, for NH_3 increases by a factor of from 2 to 3 during the 30-pulse sequence. As a result, $X_{N_2H_4}$ decreases steadily with pulse number, reaching an asymptotic level 0 (10^{-3} - 10^{-2}), depending on thruster conditions. NH_3 is approximately two-thirds (by volume) of the plume exhaust for Pulse 1 and decreases to approximately one-half of the exhaust at the end of the pulse train. H_2 increases with pulse number from about 1 to 10 percent to approximately 25 percent of the exhaust. N_2 is, of course, less sensitive than H_2 and remains at 20 to 25 percent of the exhaust.

In regard to the data shown in Figs. 12 through 15, it should be noted that NH_3/N_2 ratios are reported which exceed 4.0 in value. Equation (18) shows quite clearly that the maximum NH_3/N_2 ratio is 4.0, occuring for $\chi = 0$. This is clear evidence that interference in the mass spectrometric signal has resulted from the dissociation of N_2N_4; i.e., the ionization process of N_2H_4

$$N_2H_4 + e \longrightarrow NH_3^+ + N \cdot H + e^-$$

has produced significant NH_3 signal, resulting in an excessive value of NH_3. For such cases, for the determination of the mole fraction X_i, the maximum value of 4.0 was used for NH_3/N_2.

It is of interest to compare the values of χ for the dissociation of NH_3, which are shown in Figs. 22a through h, with the equilibrium degree of dissociation, χ^{eq}. For the reaction of Eq. (12) the equilibrium reaction constant, K, is given by

$$K = \left(\hat{\gamma}_{N_2}^{1/2}\ \hat{\gamma}_{H_2}^{3/2} \Big/ \hat{\gamma}_{NH_3}\right)\left(P_{N_2}^{1/2}\ P_{H_2}^{3/2} \Big/ P_{NH_3}\right) \tag{21}$$

where γ_i and P_i are, respectively, the activity coefficient and partial pressure, of the ith species. With the data quoted by Barrow in Ref. 6 for 723°K and estimates of the fugacity data for the reaction species, the equilibrium mole fractions of NH_3, H_2, and N_2, as well as χ, were found according to the following relations

$$P_{N_2}^{1/2}\ P_{H_2}^{3/2} \Big/ P_{NH_3} = (27/4)\frac{(\chi^{eq})^2}{1-(\chi^{eq})^2} \cdot P \tag{22}$$

and

$$X_{NH_3}^{eq} = \left(1-\chi^{eq}\right) \Big/ \left(1+\chi^{eq}\right) \tag{23}$$

$$X_{N_2}^{eq} = \chi^{eq} \Big/ 2\left(1+\chi^{eq}\right) \tag{24}$$

$$X_{H_2}^{eq} = 3\chi^{eq} \Big/ 2\left(1+\chi^{eq}\right) \tag{25}$$

where P is the total pressure (atmosphere) of the mixture. The results were obtained for T = 723°K for $1 \leq P \leq 12$ atm and are shown in Fig. 22i. Note that $0.95 \leq \chi^{eq} \leq 0.98$ for the P range of 12 to 5 atm. This result should be contrasted with the experimental values of $\chi \leq 0.33$. Clearly, the engine reservoir does not resemble an equilibrium reaction system.

The mole fraction data shown in Figs. 22a through d can be used to infer a specific heat ratio, γ, for the expansion, assuming the presence of only gaseous species. The heat capacity data for NH_3, N_2, and H_2 of Ref. 6 were used along with the relation

$$\gamma = \sum_i \left(\tilde{C}_{Pi}/R\right) X_i \Big/ \left[\sum_i \left(\tilde{C}_{Pi}/R\right) - 1\right] \tag{26}$$

where $\tilde{C}_{Pi}$ is the constant pressure molar heat capacity for species i and R is the universal gas constant. With the results of Fig. 22d for Pulse 1 and Eq. 26, Fig. 22j shows γ as a function of T_o, the reservoir temperature. It is shown that γ ranges from 1.291 at T_o = 500°K to 1.245 for T_o = 800°K. Since the reservoir temperature is lower for the first pulses than for the later pulses in a pulse train, it is believed that $1.27 \leq \gamma \leq 1.29$ is a reasonable range. The results for Pulse 30 of the sequence show that γ ranges from 1.313 to 1.270. The value of 1.28 for γ is reasonable since $T_o \approx 700$°K. Consequently, γ is approximately 1.28 for the exhaust as can be inferred from the mass spectrometric data for TC 2C. Similar results were obtained for the other cases — i.e., $\gamma \geq 1.27$. The inclusion of N_2H_4 for the Pulse 1 data would tend to lower γ by no more than 0.015, and 0.010 is more likely. No significant effect on γ of N_2H_4 is expected for Pulse 10 and above.

In contrast, with the Raman results for density and temperature, the assumption of a frozen γ and frozen chemistry expansion, and

$$n_T/n_o = \left(T/T_o\right)^{1/\gamma - 1}$$

γ can be determined experimentally. For TC's 2S and 2A the Raman data for $\hat{x} = 28.5$ (Table 2) yield $\gamma = 1.22$. The individual mole fraction values of both Raman scattering and mass spectrometric measurements, using Eq. (26), enable the inferential determination of $\gamma = 1.30$ and 1.29 for TC's 2S and 2A, respectively. Clearly, there is a discrepancy in γ, and the difference is of no small concern.

An MOCS for the expansion was obtained using Whitfield's boundary-layer correction (Ref. 7) for the internal flow region, and the results for $\gamma = 1.2$ and 1.3 are shown in Fig. 22k as a function of axial distance. The mole fraction results indicate that the expansion follows the $\gamma = 1.3$ curves; however, with the assumption that $n_T/n_o = (T/T_o)^{1/\gamma - 1}$, it was found that $\gamma = 1.22$ described the expansion. Therefore, the Raman results for n_T/n_o and T/T_o at $\hat{x} = 28.5$ lie intermediate to the $\gamma = 1.2$ and 1.3 curves of Fig. 22k and closer to the 1.2 curve. The magnitude of the boundary-layer correction for this calculation should be noted, for it is significant for all cases. For T_o = 700°K, the effective exit area ratio varies from 41.1 to 50.7 for the range of P_o values studied. The geometric exit area ratio is 55.3.

It is suggested that the results which have been presented demonstrate convincingly that the $\gamma = 1.3$ expansion curve should be followed but that $\gamma = 1.22$ is the actual heat capacity

ratio. This situation is indicative of significant condensation in the flow field; Fig. 13 of the work of Lewis and Williams (Ref. 5) regarding N_2 condensation shows just such expansion history and behavior. Further, comparison of the magnitude of the scattering function, f, of Figs. 7a and 14 of Ref. 5 further supports this contention.

4.3 QUARTZ CRYSTAL MICROBALANCE (QCM) DATA

Tables 8 through 15 are summaries of the average mass deposition rates averaged over the last ten pulses ($<\dot{m}>_{10}$) of a 30-pulse sequence. Values marked by an asterisk had a thruster pulse duration of 0.1 sec with 9.9-sec-off time. Values marked by a plus sign had a thruster pulse duration of 0.276 sec with 9.724-sec-off time.

Figures 23 and 24 show the variation of mass deposition rate, $\dot{m}$, detected by the QCM, as a function of thruster pulse number for TC's 2S, 2A, 2B, and 2C, and T_{QCM} = 100°K (Fig. 23) and 144°K (Fig. 24). As observed for the aged thruster, the mass deposition increases drastically as T_{QCM} is changed from 144 to 100°K. As the thruster test condition is changed, the mass deposition increases with increasing thrust level. The first 5 to 10 pulses always exhibit higher deposition rates than the last 10 pulses, but at T_{QCM} = 100°K the mass deposition is more uniform throughout the pulse sequence. Figure 25 shows a series of 8 pulse sequences for T_{QCM} = 144°K and TC 2A; the spread in $\dot{m}$ values can be readily observed.

Figures 26 and 27 present normalized mass deposition rates as functions of thruster inlet pressure for T_{QCM} = 100 and 144°K, respectively. It can be observed that both normalized first-pulse rates and $<\dot{m}>_{10}$ values are linear with inlet pressure. For each T_{QCM} value, the mass deposition rates are normalized to the value measured at TC 2A. Figure 28 also presents normalized mass deposition rates as functions of thruster inlet pressure for initial catalyst bed temperatures of 200 and 400°K. The increased mass deposition for the lower T_{CATB} value is readily observed.

Figure 29 presents mass deposition rate as a function of thruster pulse number for various values of the thruster horizontal position; this gives an effective variation of mass deposition rate with angular position of the thruster (see Fig. 4). The $<\dot{m}>_{10}$ values obtained from data such as shown in Fig. 29 are plotted as a function of effective θ in Fig. 30 for T_{QCM} = 144°K. The data are normalized to the θ = 30 deg value, and a plot of the Hill-Draper function (Ref. 5) is also shown with δ = 10.0. The experimental data fit the calculated curve very well for $0 < \theta < 30$ deg. However, as θ increases past 30 deg, the experimental values are increasingly higher than those predicted. Several values for T_{QCM} =

100°K are also shown. For this lower temperature the data do not exhibit as much dependence on the θ values as for T_{QCM} = 144°K; therefore, the Hill-Draper model with δ = 10.0 is inadequate for predicting the angular dependence of the mass deposition rate.

4.4 ENGINE PERFORMANCE DATA

A detailed discussion of the thruster calibration process has been presented in Ref. 1. Calibration of the refurbished thruster was performed using the method described in Ref. 1 during the second test period in which the thruster was installed (TP 20). The calibrations were checked during several subsequent test periods, and reasonable consistency was observed.

The pulsed-mode thruster calibrations are shown in Fig. 31. The ordinate in Fig. 31 is the peak pressure during Pulse 25 of a sequence. The initial catalyst bed temperature was held as near as possible to 400°F, but the internal catalyst bed heater was not very effective in controlling the bed temperature. The duty cycle for the engine was 0.138 sec on/9.862 sec off. Cost considerations prohibited a posttest calibration.

The refurbished (or new) thruster arrived at AEDC without thermocouples attached. Three Chromel®-Alumel® thermocouples were attached at AEDC. Two of the thermocouples were located near the original thermocouple locations — in the thruster chamber and at the throat. Figure 32 shows the external wall temperature of the catalyst bed chamber as a function of inlet pressure for Pulse 25 of a sequence.

The initial performances of the aged thruster and the refurbished thruster were approximately the same (Ref. 1). Therefore, the test matrix chosen for the refurbished thruster was essentially the same as that used for the aged thruster. The only difference was that the initial 600°F catalyst bed temperature cases had to be eliminated because of the inability of the internal heater to bring the bed to that temperature. The test matrix for the new thruster experiments is given in Table 1.

The pulse shape of the thruster was investigated for the conditions of interest by using the same close-coupled 250-psia pressure transducer as used for the aged thruster. The data were recorded for pulse sequences of 60 pulses each for the 400°F initial bed temperature cases. Typical results for Pulses 1 and 60 for each of these cases are shown in Figs. 33 through 36. Zero time corresponds to the initiation of valve current; valve closing begins at 138 msec. The first pulses of a sequence were not always consistent in behavior; an example of this is given in Fig. 36. The erratic behavior was uncommon, but it occasionally occurred for any thrust condition. The second pulse was generally back to normal; however, in one

instance three of these "chug" pulses were observed before normal start-up. The stair-step appearance of the data is an artifact of the digital data acquisition. The intrapulse variations of wall temperature will not be presented since only minute changes could be observed during a pulse.

Thruster operation during steady-state burns was also investigated. Figures 37 and 38 demonstrate the behavior of the combustion chamber pressure during a continuous, 60-sec firing for inlet pressures of 147 and 230 psia, respectively. Also included on the figures are the value of the final lower wall temperature and the steady mass flow rate for each case. Firings were not exactly 60 sec in duration because thruster operation was manually terminated for these firings. The mass flow measurements were made using a Lee viscojet as described in Ref. 1.

The pulse-to-pulse variation in thruster performance was a major concern of the experiment, and it was investigated for pulse sequences of 30 pulses in duration. The outer wall of the thrust chamber had two Chromel-Alumel thermocouples attached to it. One was labeled T_{CATB} and the other T_{COMB}. They were located approximately 1/8 in. apart. Results for the two temperature measurements as functions of pulse number are given for the four thrust conditions in Figs. 39 through 46. The variation of initial catalyst bed temperature for these data demonstrates the difficulty in maintaining a constant starting bed temperature using the internal heater. The variations in thrust chamber pressure with pulse number are demonstrated for the four thrust cases in Figs. 47 through 50. The ordinate of these figures is the maximum pressure that occurred at any point during the pulse. The pressure values are plotted on a scale with sufficient detail to show the minor variations from pulse to pulse.

The chamber performance during the refurbished thruster experiments was nominally the same as for the aged thruster. During engine operation the simulated altitude in the chamber was maintained at 90 to 100 km for test conditions except steady-state burns. For steady-state burns the vacuum chamber pressure reached a value of approximately 2×10^{-3} torr, or a simulated altitude of approximately 85 km, and remained basically constant throughout the burn.

5.0 COMPARISON OF REFURBISHED AND AGED THRUSTER RESULTS AND CONTAM II PREDICTIONS

5.1 COMPARISON OF SPECIES DENSITIES AND PLUME TEMPERATURES

Table 17 presents a comparison of average species density and temperature values obtained using laser-Raman scattering for both the aged and refurbished thruster. The data were obtained at the $\hat{x} = 28.5$ axial position (0.5 in. from the thruster exit plane) at TC's 2S and 2A. The data compare very well when the total measurement uncertainty is considered.

The aged thruster results do show higher $n(H_2)/n(N_2)$ and T_R/T_o values, and the values of γ obtained using the flow-field density and temperature data show $\gamma = 1.26$ for the aged thruster and $\gamma = 1.22$ for the refurbished thruster.

The CONTAM II subprogram N2H4 was run at AEDC for the monopropellant thruster; the results are shown in Table 18. The mole fractions are averaged over the last 20 pulses in a 25-pulse sequence; they are the values predicted to exist at 90 msec into the thruster pulse, which is the time at which laser-Raman data were obtained.

The CONTAM II subprogram MULTRAN was also run at AEDC to predict the axial variation of temperature and number density; the results are presented in Fig. 7. The axial variation of T/T_o as predicted by CONTAM II using $\gamma = 1.2$ is in good agreement with the $\gamma = 1.2$ MOCS prediction with the exception of the region near $\hat{x} = 26$. The refurbished thruster T_R/T_o values agree very well with the CONTAM II and $\gamma = 1.2$ MOCS predictions. The aged thruster T_R/T_o values fall between the MOCS predictions as expected from the γ values determined using species mole fractions. The agreement of CONTAM II with the MOCS result is not understood because the MOCS calculation included a significant correction caused by the nozzle boundary layer and the CONTAM II did not.

5.2 COMPARISON OF PLUME SPECIES MOLE FRACTION RATIOS

Intrapulse variation of $n(NH_3)/n(N_2)$ for TC 2A is shown in Fig. 13 for both the refurbished and aged thruster; the intrapulse behaviors are quite different. For the aged thruster the first-pulse $n(NH_3)/n(N_2)$ value remains high and steady throughout the pulse, whereas for the refurbished thruster the $n(NH_3)/n(N_2)$ values reach an early maximum associated with inlet vlave opening and declines rapidly throughout the remainder of the pulse until valve closing. For the aged thruster Pulse 25 exhibits a behavior very similar to Pulse 1 of the refurbished thruster. Pulse 30 of the refurbished thruster has $n(NH_3)/n(N_2)$ values that show a slight increase at valve opening and remain steady at a low level throughout the pulse until valve closing.

Pulse-to-pulse variations of mole fraction ratios of minor species exhibit perhaps the greatest difference between aged and refurbished thrusters. Figure 51 presents the variation of species mole fraction ratios as a function of pulse number for TC 2B. Again the $n(NH_3)/n(N_2)$ values for both thrusters are quite similar. However, the refurbished thruster shows plume N_2H_4 an order of magnitude less than the aged thruster.

5.3 COMPARISON OF RAYLEIGH SCATTERING LEVELS

Rayleigh scattering levels, $\hat{I}_{RY}$, measured in the two thruster plumes are compared in Table 20 for the TC's 2S and 2A. The scattering function, f, defined by Eq. (9), was

evaluated for $\gamma = 1.2$ and is also tabulated in Table 20. As observed in Table 20, the f factors for the aged thruster are approximately a factor of 50 greater than those for the refurbished thruster. Nevertheless, the Rayleigh scattering levels for the refurbished thruster remain more than an order of magnitude greater than expected (as can be observed in Table 20 and Fig. 7) for a noncondensing, particulate-free plume expansion.

To investigate these large levels of Rayleigh scattering, an experiment was designed, simulating the thruster plume expansion in the RVC. A nozzle assembly was fabricated to duplicate the nozzle of the thruster, and the assembly was attached to a GTE-Sylvania heated source as described in Ref. 4. A set of three mixtures was prepared by the AEDC Chemical Laboratory. The first two mixtures simulated a plume $\gamma = 1.2$, and the third mixture simulated a plume $\gamma = 1.25$. The first mixture was prepared using only N_2 and NH_3 with the NH_3 mole fraction set to equal that predicted by CONTAM II for TC 2S. The N_2 mole fraction was set equal to the sum of the H_2 and N_2 mole fractions predicted by CONTAM II for TC 2S. For the second mixture, the N_2, H_2, and NH_3 mole fractions were those predicted by CONTAM II for TC 2S. For the third mixture the mole fractions of N_2, H_2, and NH_3 were determined using Fig. 90 of Ref. 1.

The mixtures were permitted to flow steadily through the heated source/nozzle assembly, and the reservoir pressure and temperature were set to equal the values of TC 2S as given in Table 19. The flow could be maintained for approximately 60 sec when H_2 was a mixture constituent before the RVC pressure reached a level of 10 mtorr.

The collection optics, dispersion, and detection system was the same as that used for the thruster measurements. However, instead of a pulsed ruby laser, a continuous argon-ion laser was used as a light source at a wavelength of 5,145 Å.

Results of these experiments for $\hat{x} = 78.5$ are listed in Table 20. The $\gamma = 1.2$ and 1.25 mixtures of N_2-H_2-NH_3 have Rayleigh scattering levels that bracket those observed for the refurbished thruster. The f factor for the $\gamma = 1.2$ N_2-H_2-NH_3 mixture is approximately a factor of 2 higher, and the f factor for the $\gamma = 1.25$ N_2-H_2-NH_3 mixture is approximately a factor of 2 lower than the f factor for the refurbished thruster at TC 2S. It is believed that the high Rayleigh levels for the refurbished thruster are a direct result of species condensation in the plume flow field. Figure 52 is a pressure-temperature plot with the vapor pressure curves of N_2H_4, H_2O, NH_3, and N_2 as well as $\gamma = 1.2$ and 1.3 isentropes for TC 2S reservoir conditions. From the NH_3 isentrope intersections of the NH_3 vapor pressure curve and the $\gamma = 1.2$ and 1.3 axial variations of T/T_o, it can be seen that the NH_3 saturation occurs from $\hat{x} = 9.5$ ($\gamma = 1.3$) to $\hat{x} = 34$ ($\gamma = 1.2$). Note in Fig. 52 that H_2O and N_2H_4 begin condensing much earlier. Based on previous experiments with an N_2-CO_2 mixture (Ref. 6),

the H_2O and N_2H_4 condensate can provide nucleation sites that will bring about NH_3 condensation near the saturation point.

It is believed that the high Rayleigh scattering levels for the aged thruster resulted from raw fuel traveling down the axial centerline. This explanation is supported by the high mass deposition rate measured on the axial centerline, the particle sampling measurements, and the radial Rayleigh scattering profiles that reveal extremely high levels only on the axial centerline (see Ref. 1).

5.4 COMPARISON OF MASS DEPOSITION RATES

In general, throughout the testing of the aged thruster, the measured mass depositions steadily increased until the "thruster catastrophe" occurred, which resulted in saturation of the QCM with just a few thruster pulses. Comparisons of $<\dot{m}>_{10}$ values for the aged and new thruster averaged over each thruster's experimental period are presented in Table 21; the values are in fair agreement to within the estimated data uncertainty.

There are, however, two major differences between the aged and refurbished thrusters with regard to mass deposition rates. The Pulse 1 mass deposition rates for the refurbished thruster are, on the average, approximately a factor of 3 higher than the $<\dot{m}>_{10}$ values, whereas for the aged thruster Pulse 1, the rates are an order of magnitude, or more, greater than the $<\dot{m}>_{10}$ values. The aged thruster axial centerline mass deposition rates were approximately a factor of 2 higher than expected as indicated by the behavior of the angular variation of off-axis mass deposition rates which followed the Hill-Draper function very well. Although axial centerline mass depositions were not obtained for the refurbished thruster, the effective angular variations were made within 7 deg of the axis, and the results indicate that an abnormal mass deposition rate should not be expected on the axial centerline.

5.5 COMPARISON OF ENGINE PERFORMANCE

The thruster peak chamber pressure versus inlet pressure calibrations for the aged and refurbished thrusters agree very well. The intrapulse variations of thruster chamber pressure also agree well. The variations of the catalyst bed lower wall temperature (Pulse 25 of a sequence) versus inlet pressure reveal that the refurbished thruster was about 50 to 75°K hotter than the aged thruster after its "catastrophe." However, an earlier calibration of the aged thruster taken before the catastrophe shows good agreement between catalyst bed lower wall temperatures. Examination of the pulse-to-pulse variations of catalyst bed lower wall temperature also reveals that the refurbished thruster warmed up much more rapidly over the first ten pulses than the aged thruster did. Conversely, pulse-to-pulse variations of

thruster peak chamber pressure reveal that the aged thruster chamber pressure increased more rapidly over the first ten pulses did that of the refurbished thruster.

6.0 SUMMARY OF RESULTS

The final phase of a measurements program for a 0.1 lbf monopropellant thruster has been completed, and the thruster exhaust plume has been characterized by utilizing a variety of noninterfering plume diagnostic techniques. The conclusions that can be made with regard to the results of these measurements are listed as follows:

1. Laser-Raman measurements of species mole fractions are in reasonable (± 20 percent) agreement with mass spectrometric measurements for species for which data were acquired using both techniques. Further, these mole fractions are in reasonable agreement (± 20 percent) with the predictions of CONTAM II for mole fractions in the engine reservoir. This result confirms the assumption of chemically frozen flow.

2. Raman scattering data for n_T/n_o and T/T_o are in approximate (± 20 percent) agreement with an AEDC MOCS calculation with boundary-layer corrections that are significant for the expansions studied. Curiously, the MULTRAN subprogram of CONTAM II predicted acceptable T/T_o results (within ± 15 percent of MOCS) but grossly inaccurate n_T/n_o values (~ 50 percent lower than MOCS) and did this with no boundary-layer correction. Including the boundary layer in MULTRAN would have worsened the agreement with T/T_o and bettered the n_T/n_o predictions.

3. Rayleigh scattering measurements indicate a significant quantity of condensate in the thruster plume. This has been verified in a particulate-free simulated thruster plume. If a condensate diameter of 50 Å is assumed, the condensate mole fraction is calculated to be on the order of 10^{-5}. The results also indicate that any computer code (such as CONTAM II subprogram KINCON) that does not consider the kinetics of condensation processes and the condensation of multiple species will be inadequate.

4. Rayleigh scattering levels in the new thruster plume are more than an order of magnitude less than those observed for the aged thruster. This indicates fewer and/or smaller particulates in the new thruster plume. During the initial pulses of a pulse sequence, the Rayleigh scattering level is an order of magnitude higher than the average of the last 10 pulses in a 30-pulse sequence.

5. The mass spectrometer indicates large quantities of hydrazine (mole fraction = 0.02 to 0.05) in the forward-flow plume region for all operating conditions during the first few pulses of a pulse sequence. However, the amount of hydrazine is an order of magnitude less than that observed in the aged thruster plume.

6. QCM mass deposition measurements also indicate significant amounts of N_2H_4 and H_2O present in the initial pulses from a pulse sequence at all thruster operating conditions. However, the Pulse 1 mass deposition rates are only a factor of 3 higher than the average rate of the last 10 pulses, whereas for the aged thruster the Pulse 1 values were an order of magnitude or more greater than the average rate of the last 10 pulses.

7. The angular variation of the relative (not absolute) mass deposition rate as measured by the QCM at a temperature of 144°K is described within ±15 percent by the Hill-Draper model over the angular range of from 7 to 30 deg with a plume "slenderness" parameter $\delta = 10.0$. For 30 deg $\leq \theta \leq$ 44 deg, the mass flux exceeds the prediction by as much as an order of magnitude. However, for $T_{QCM} = 100°K$ the Hill-Draper prediction can be as much as a factor of 2 greater than measured values for $\delta = 10.0$. Consequently, this model is of limited use for prediction of mass flux.

8. QCM mass deposition measurements indicate a near linear variation with thruster inlet pressure, and initial catalyst bed temperature can increase the mass deposition rate by as much as 50 percent.

9. Laser-Raman and mass spectrometer mole fraction measurements indicate an average plume $\gamma = 1.27$ to 1.29, whereas for the aged thruster an average plume $\gamma = 1.25$ was measured.

10. To within experimental uncertainty, the average mass deposition rates of the last 10 pulses for the refurbished and aged thrusters are in agreement.

11. Engine performance measurements indicate that the only significant difference between the performances of the refurbished and aged thrusters is a higher catalyst bed lower wall temperature for the former. Consequently, engine performance parameters are not accurate indicators for flow-field and contamination characterization.

REFERENCES

1. Williams, W. D., McCay, T. D., Powell, H. M., Weaver, D. P., Price, L. L., Jones, J. H., and Lewis, J. W. L. "Experimental Study of the Plume Characteristics of an Aged Monopropellant Hydrazine Thruster." AEDC-TR-79-2 (ADA068326), April 1979.

2. Hoffman, R. F., Webber, W. T., and Cherry, S. S. "Plume Contamination Effects Prediction: The CONTAM Computer Program, Version II." AFRPL-TR-73-46 (AD768616), August 1973.

3. Williams, W. D. and Lewis, J. W. L. "Condensation Scaling Laws for Reservoir and Nozzle Parameters and Gas Species as Determined by Laser Scattering Experiments." AEDC-TR-76-67 (AD-A029733), September 1976.

4. Washburn, E. W., editor-in-chief. *International Critical Tables of Numerical Data, Physics, Chemistry, and Technology*, Vol. 7. McGraw-Hill Book Company, Inc., New York, 1930.

5. Lewis, J. W. L. and Williams, W. D. "Profile of an Anisentropic Nitrogen Nozzle Expansion." *Physics of Fluids*, Vol. 19, No. 7, July 1976, pp. 951-959.

6. Barrow, Gordon M. *Physical Chemistry*. McGraw-Hill Book Company, New York, 1973 (Third Edition).

7. Whitfield, David L. "Viscous Effects in Low-Density Nozzle Flows." AEDC-TR-73-52 (AD761489), June 1973.

8. Williams, W. D. and Lewis, J. W. L. "Experimental Study of the Reservoir Temperature Scaling of Condensation in a Conical Nozzle Flowfield." In *Progress in Astronautics and Aeronautics Rarefied Gas Dynamics*, Vol. 51. Part II. Edited by J. Leith Potter. American Institute of Aeronautics and Astronautics. MIT Press, Cambridge, Mass., 1977, pp. 1137-1151.

9. Hill, Jacques A. F. and Draper, James Stark. "Analytical Approximation for the Flow from a Nozzle into a Vacuum." *Journal of Spacecraft and Rockets*, Vol. 3, No. 10, Oct. 1966, pp. 1552-1554.

10. Lewis, J. W. L., Williams, W. D., and Powell, H. M. "Laser Diagnostics of a Condensing Binary Mixture Expansion Flow Field." In *Proceedings of the Ninth International Symposium on Rarefied Gas Dynamics*, Vol. 2. Edited by Manfred Becker and Martin Fiebig. DFVLR Press, Porz-Wahn, West Germany, 1974, pp. F.7-1 to F.7-8.

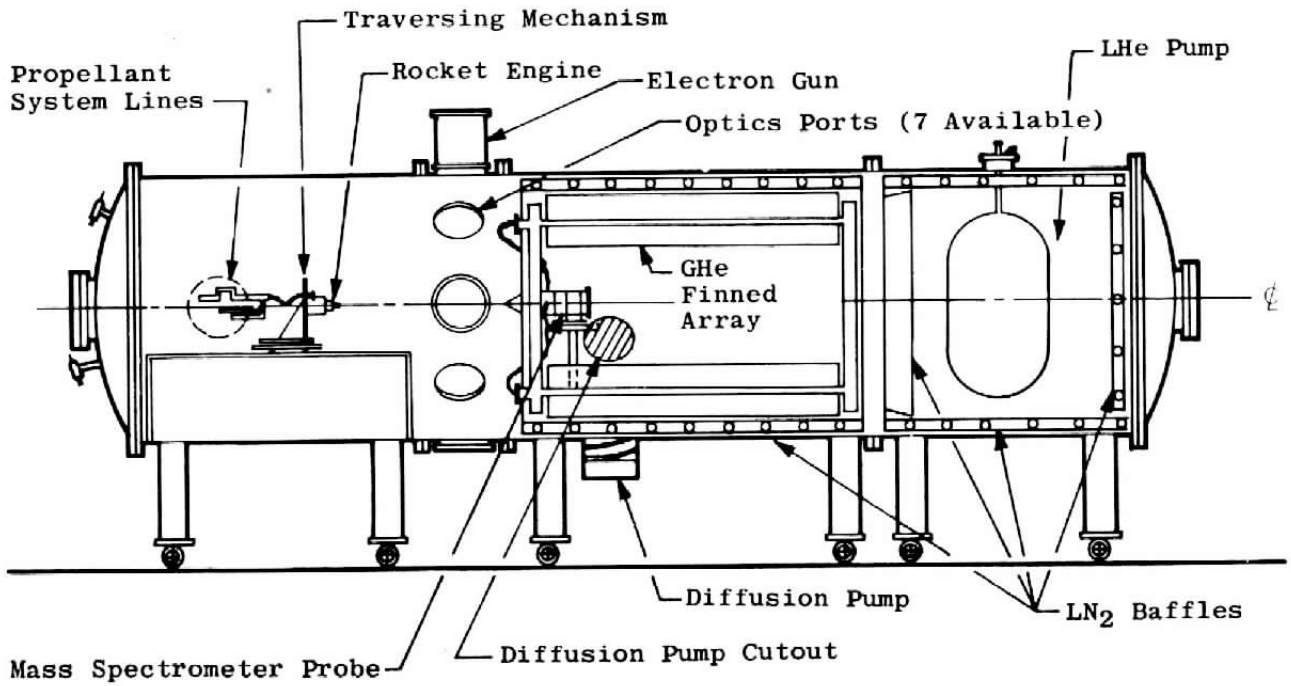

Figure 1. Thruster installation in the Research Vacuum Chamber.

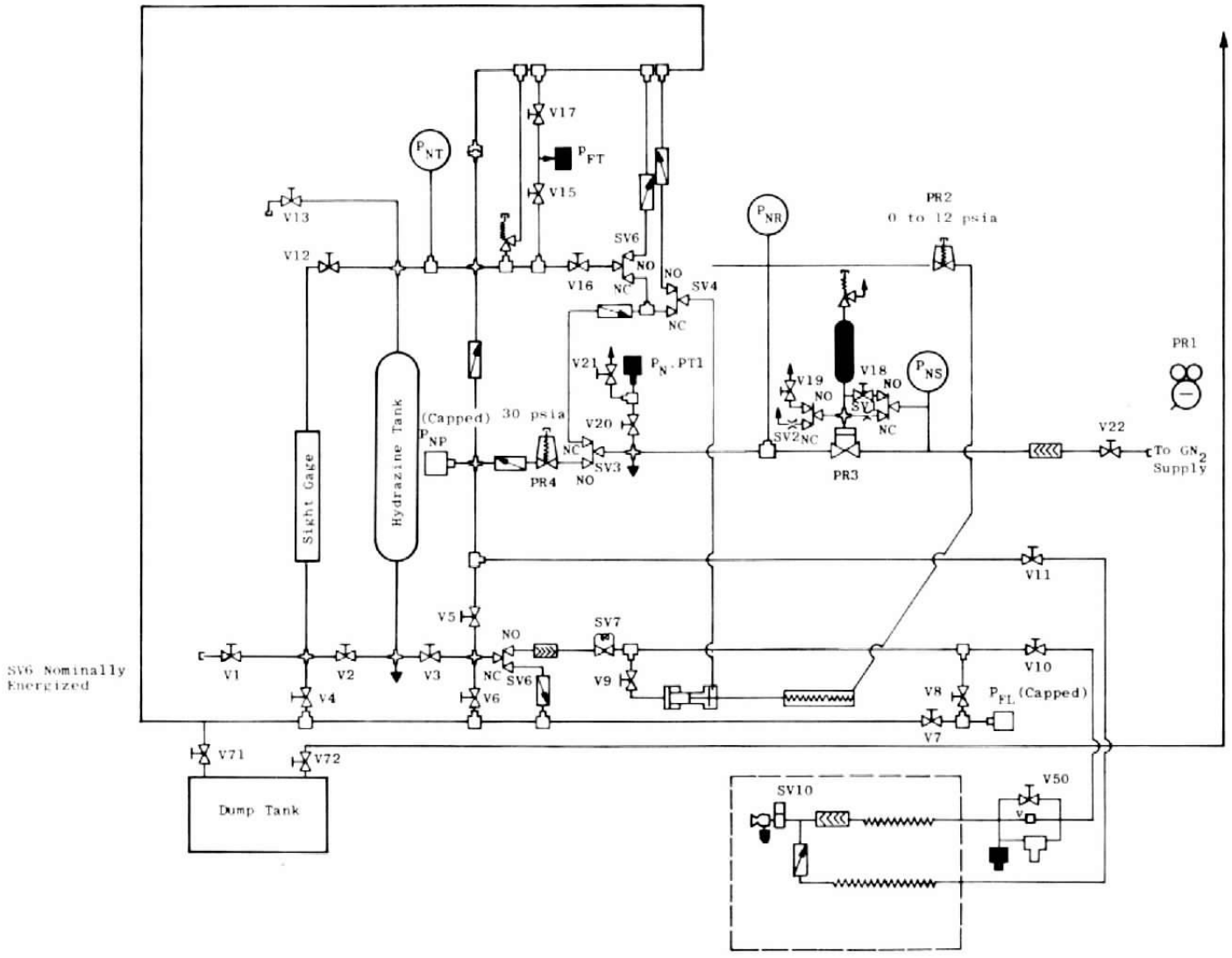

Figure 2. Hydrazine propellant system schematic.

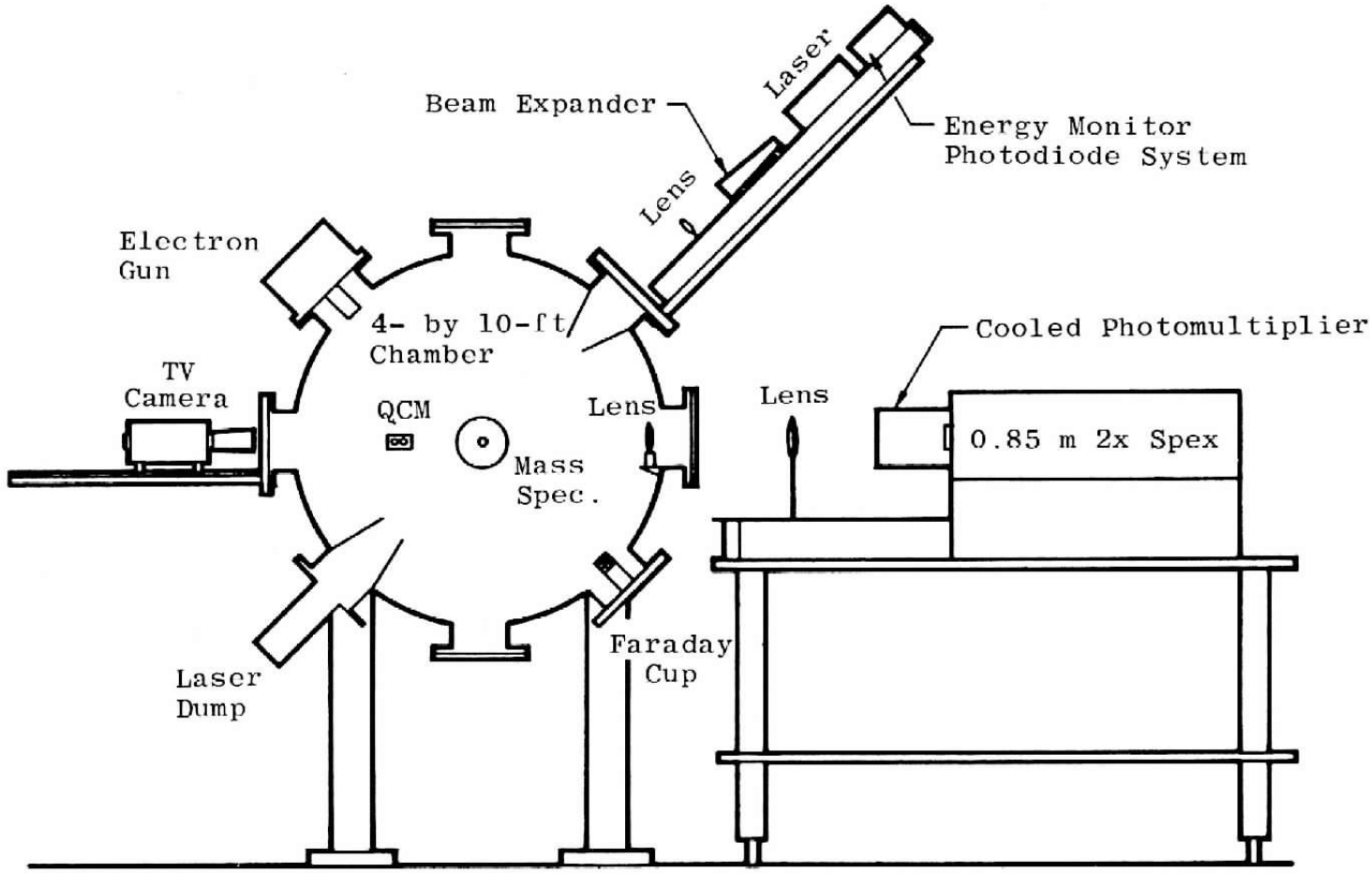

Figure 3. Experimental arrangement for special diagnostic instrumentation.

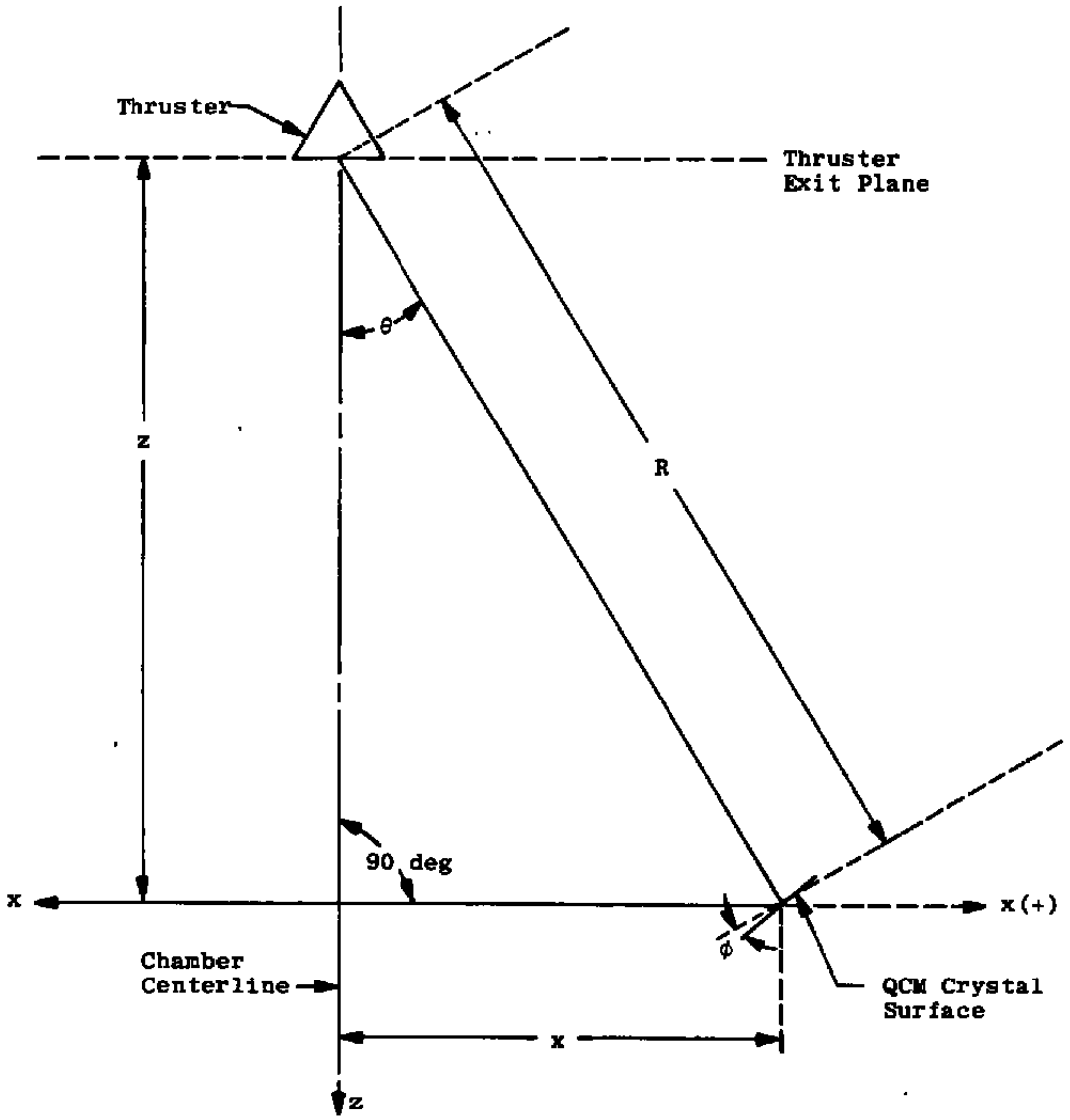

QCM position in thruster plume is given by (z,x) where
z - distance along the thruster/chamber center measured from nozzle exit plane.
x - perpendicular distance from thruster centerline to the center of the crystal surface. Note: x is positive in direction of crystal surface.
ϕ = 30 deg - θ

Figure 4. QCM reference position in thruster plume.

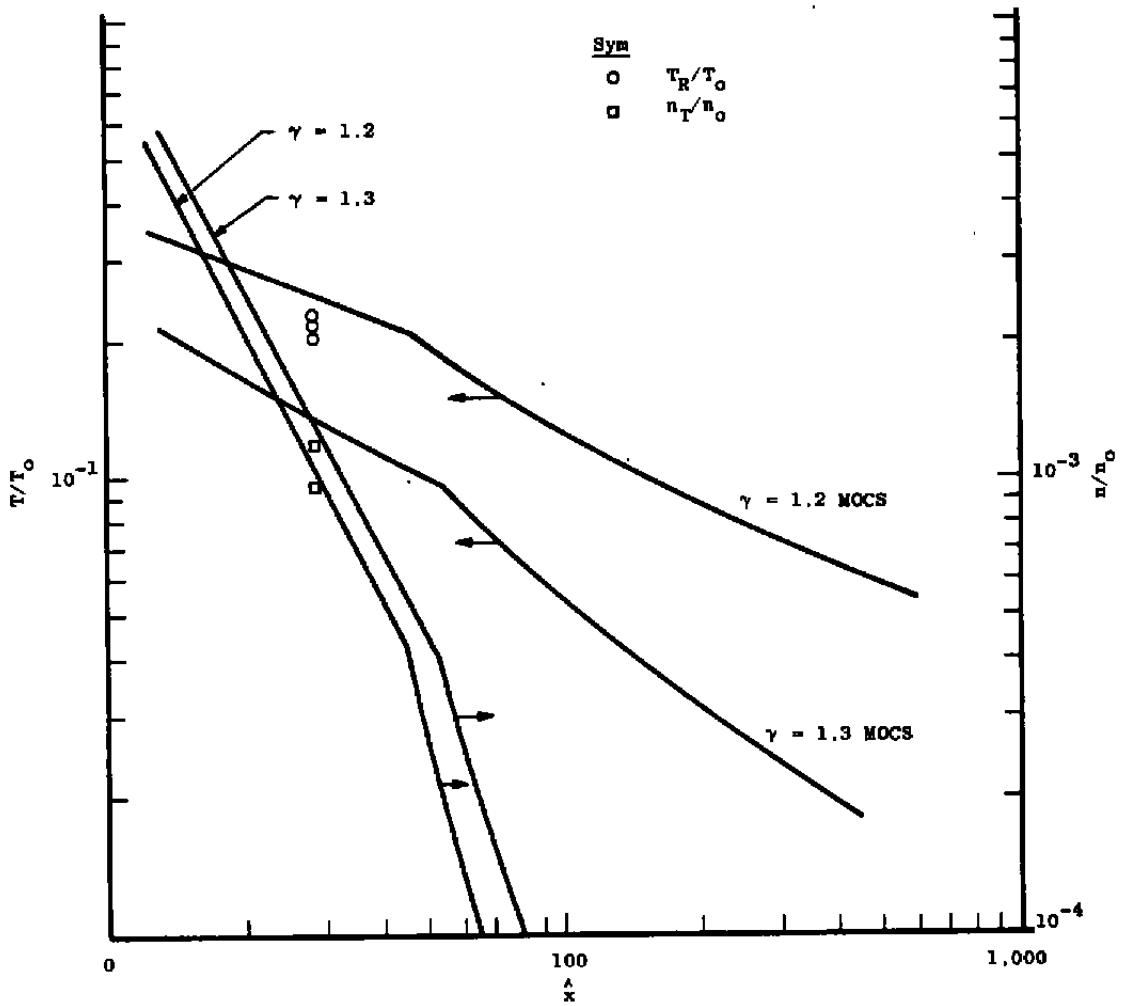

Figure 5. Axial variation of temperature and density.

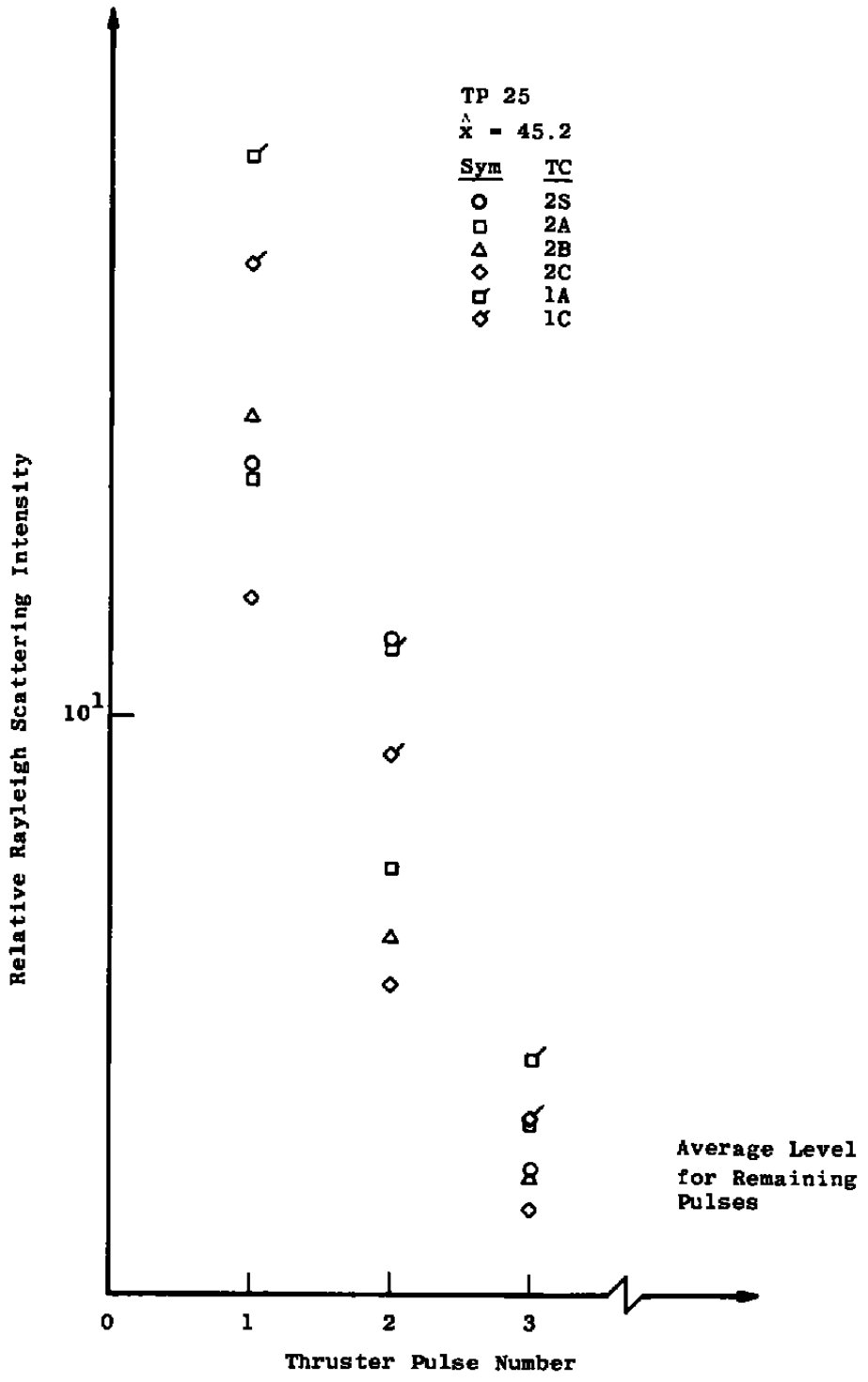

Figure 6. Variation of relative Rayleigh scattering intensity during first three pulses.

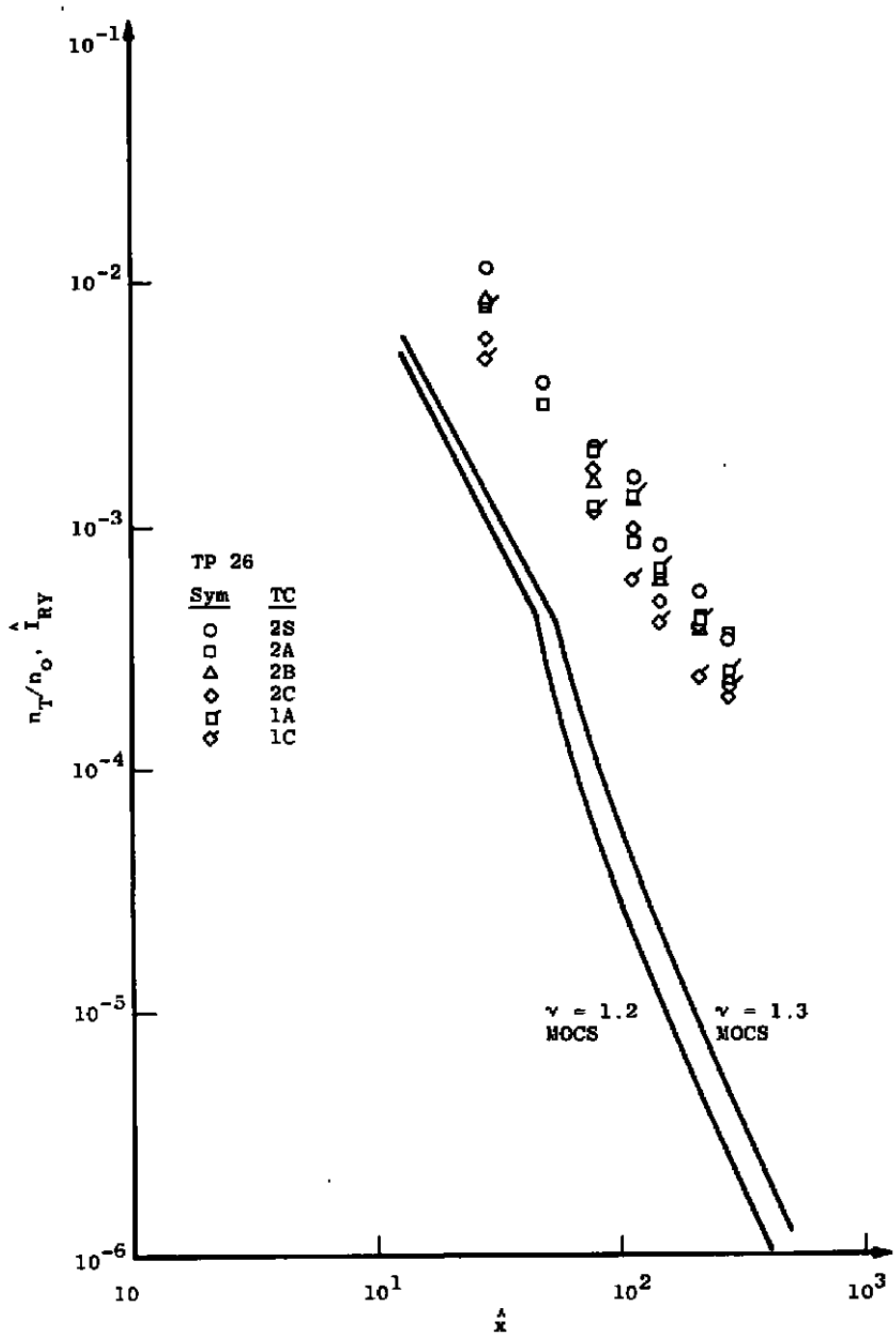

a. Axial variation of $\hat{I}_{RY}$ and n_T/n_o

Figure 7. Variation of scattering parameters with axial location and reservoir conditions.

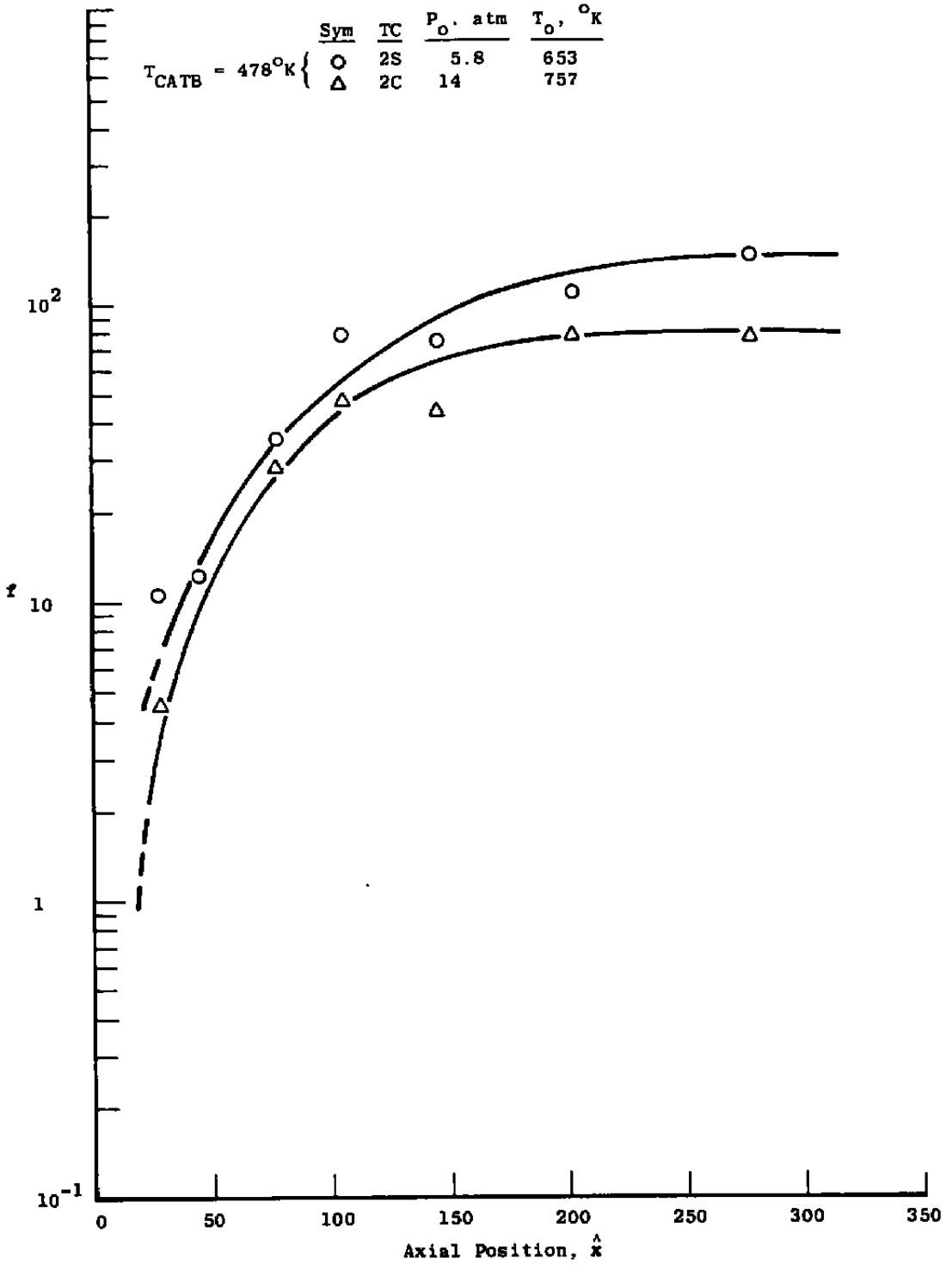

b. Axial variation of Rayleigh scattering function, f
Figure 7. Continued.

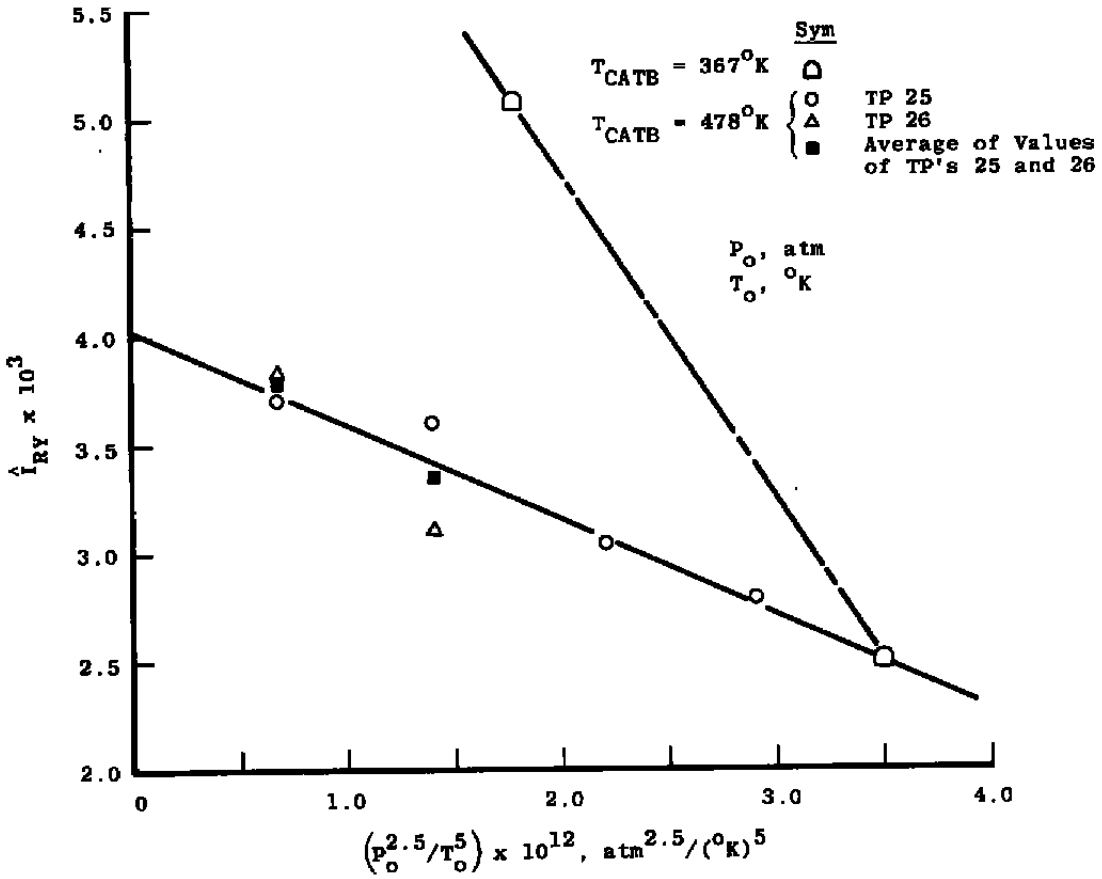

c. Variation of Rayleigh ratio with reservoir parameters and axial position $\hat{x}$ = 45.2

Figure 7. Concluded.

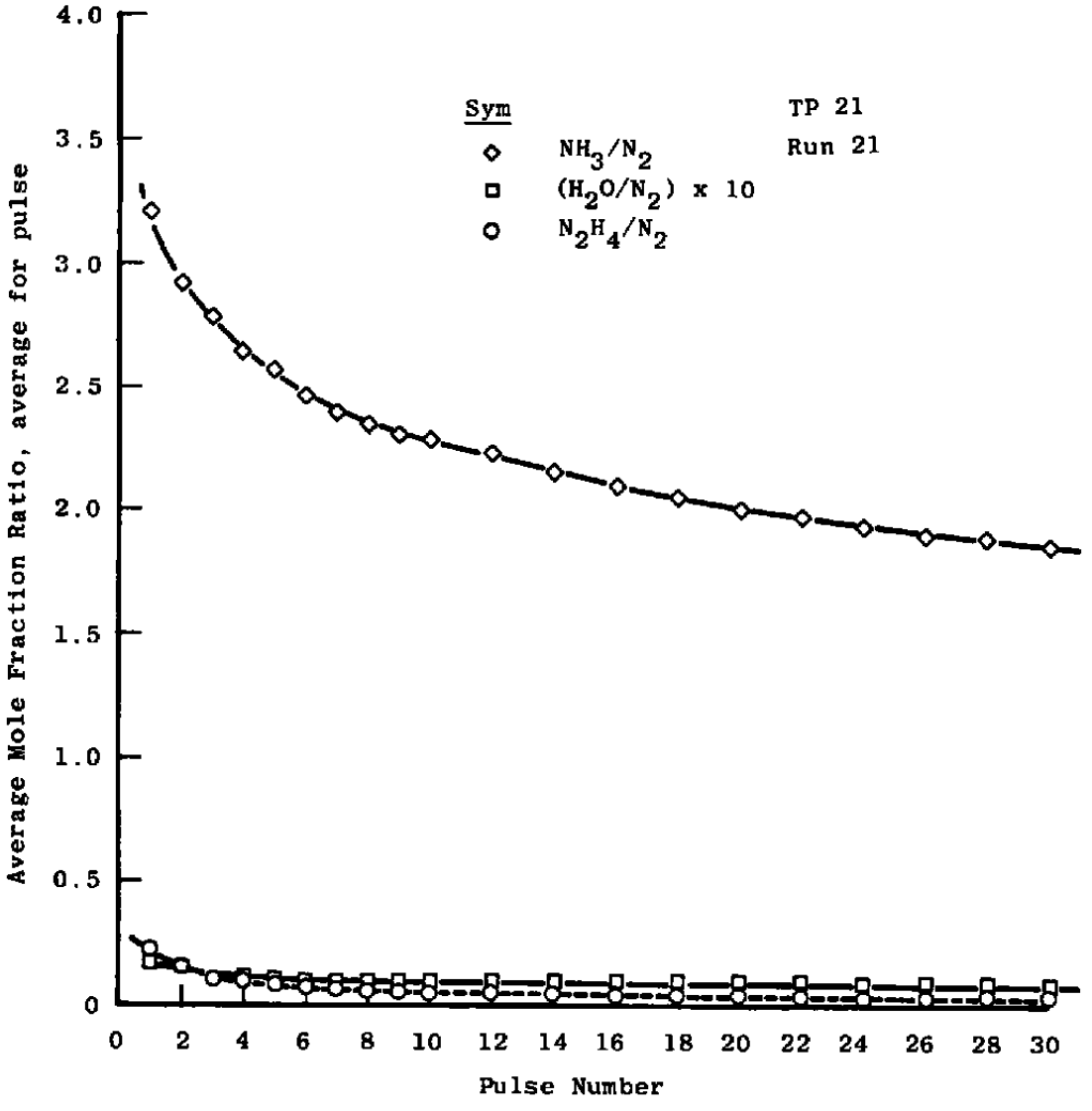

Figure 8. Species mole fraction ratios as a function of pulse number, TC 2S.

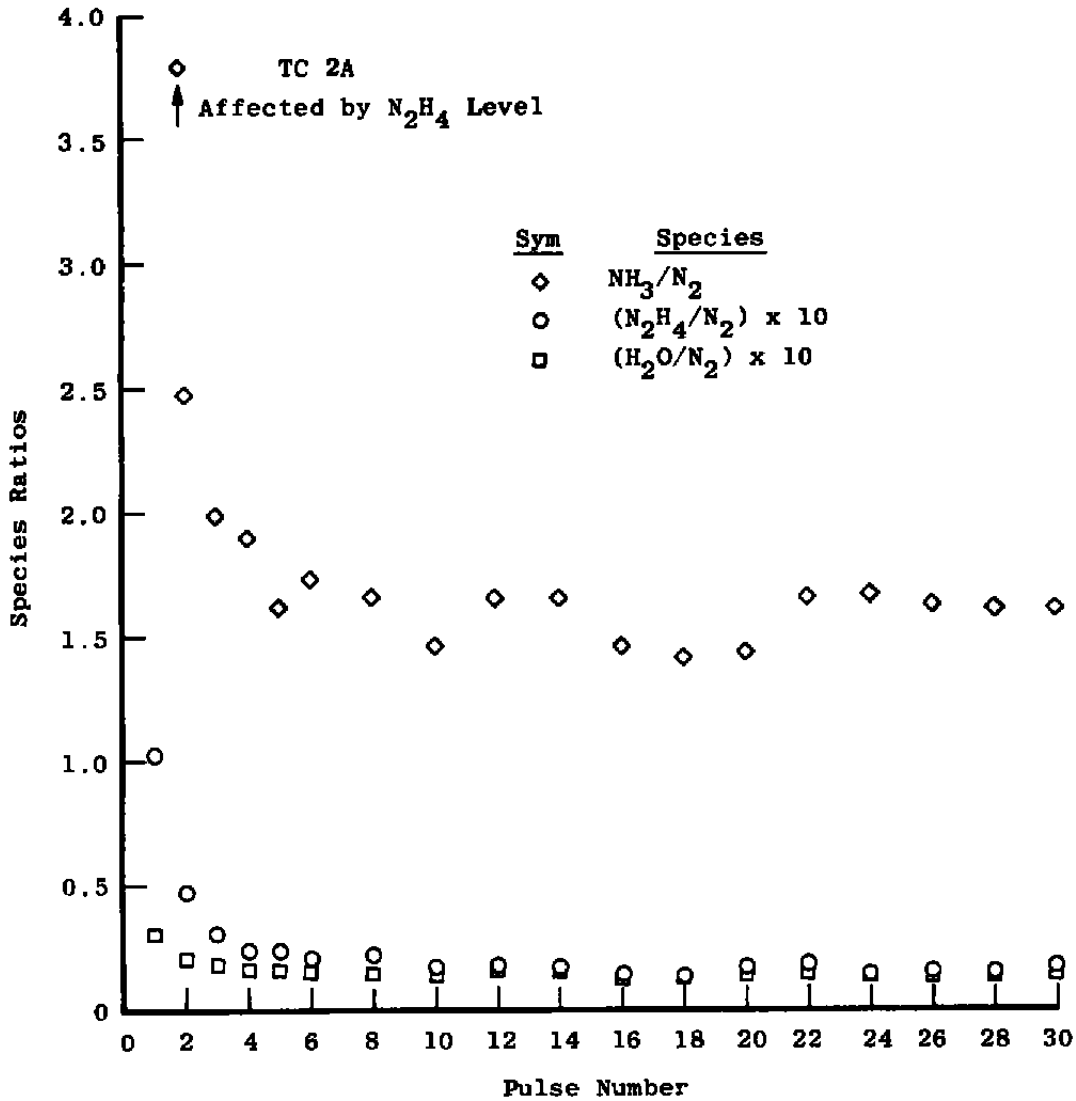

Figure 9. Species mole fraction ratios as a function of pulse number, TC 2A.

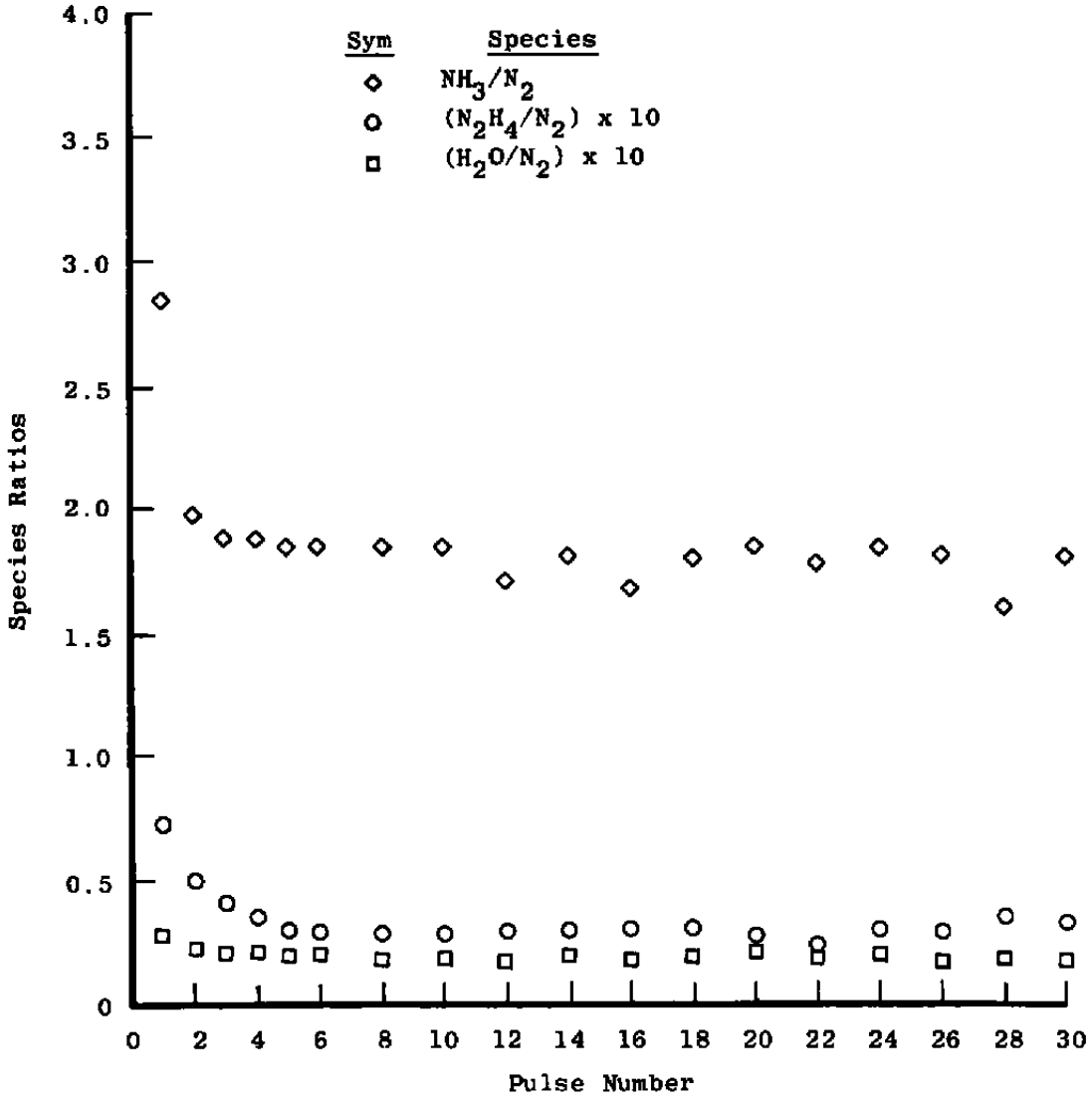

Figure 10. Species mole fraction ratios as a function of pulse number, TC 2B.

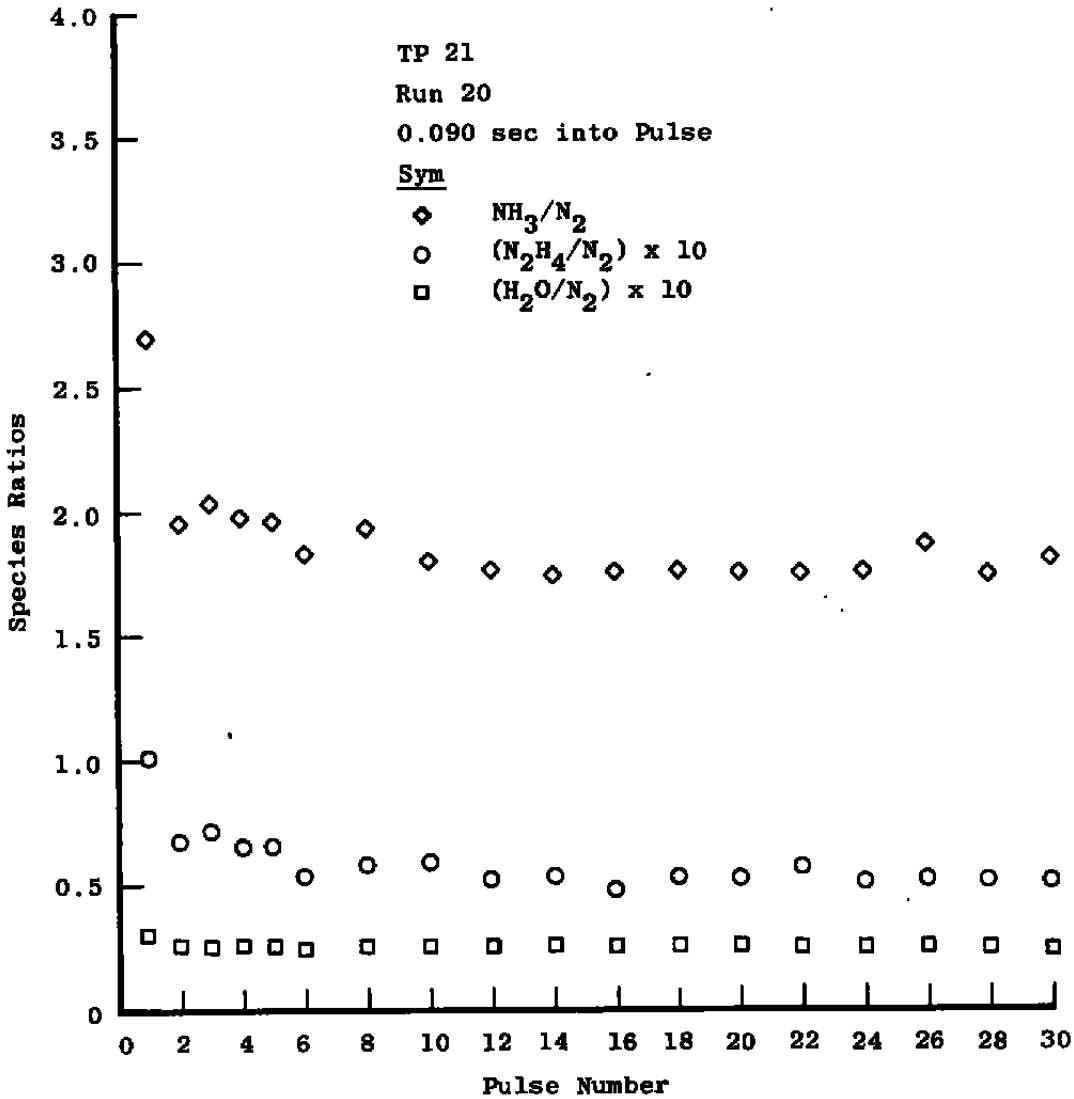

Figure 11. Species mole fraction ratios as a function of pulse number, TC 2C.

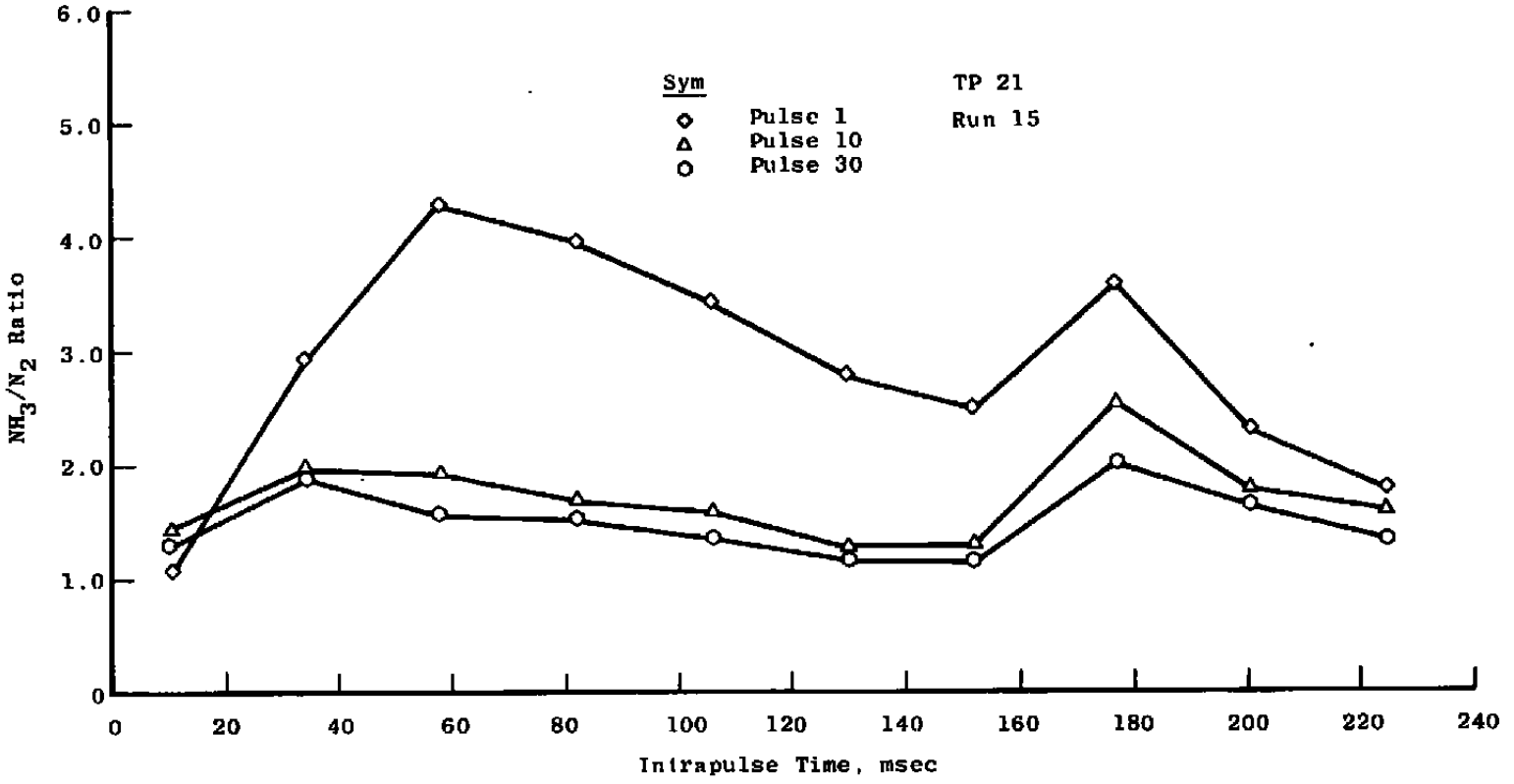

Figure 12. Intrapulse variation of the ammonia-to-nitrogen mole fraction ratio, TC 2S.

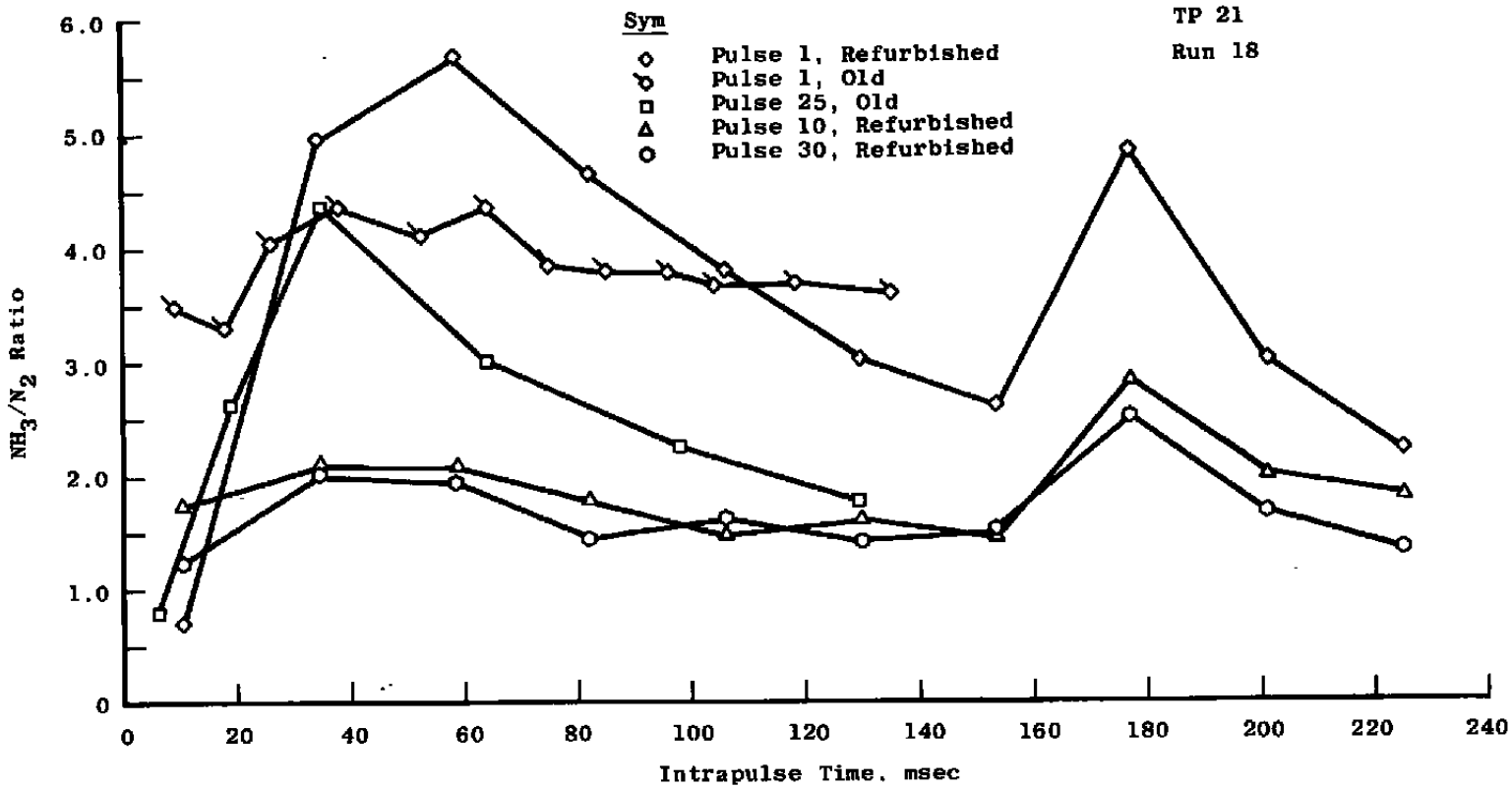

Figure 13. Intrapulse variation of the ammonia-to-nitrogen mole fraction ratio, TC 2A.

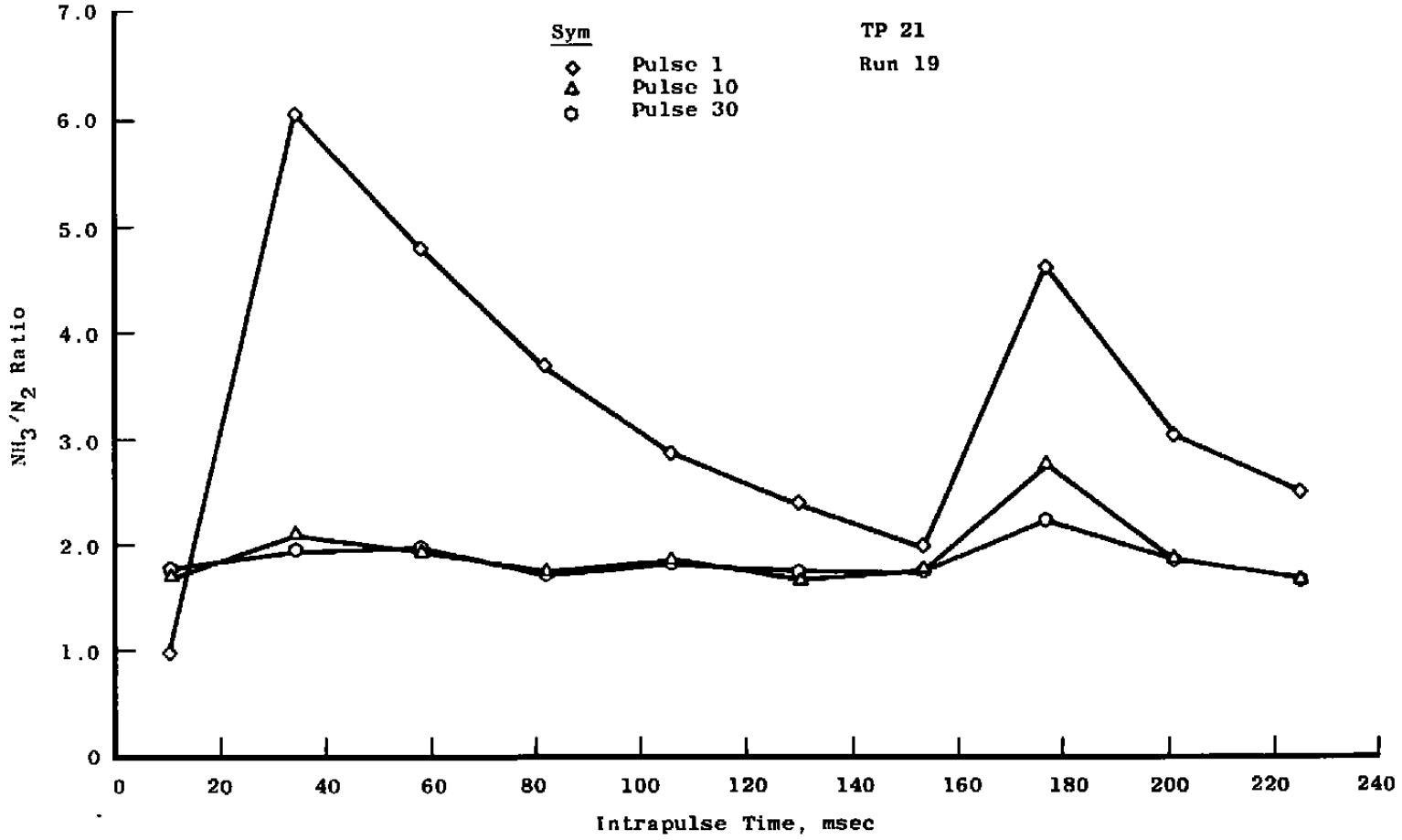

Figure 14. Intrapulse variation of the ammonia-to-nitrogen mole fraction ratio, TC 2B.

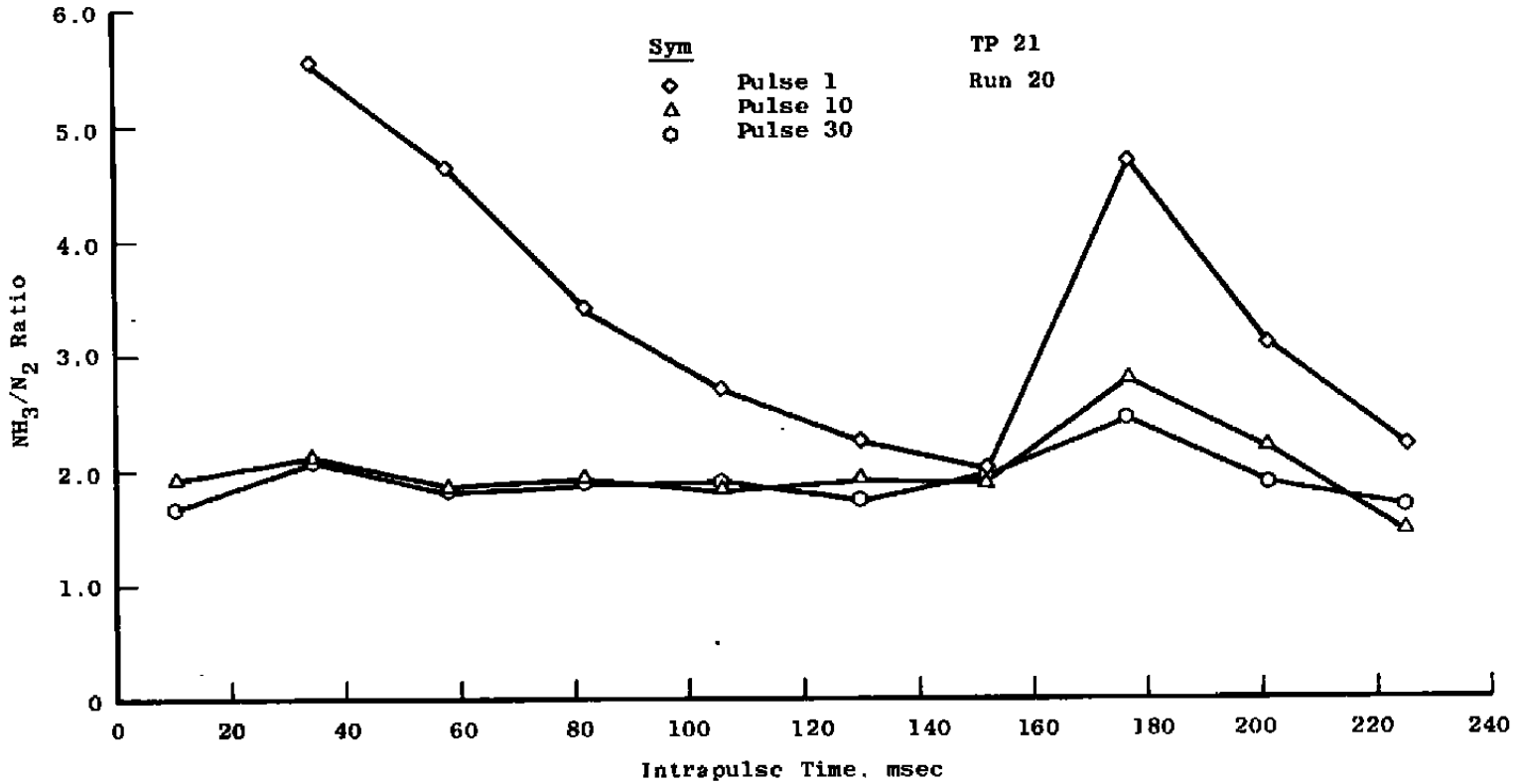

Figure 15. Intrapulse variation of the ammonia-to-nitrogen mole fraction ratio, TC 2C.

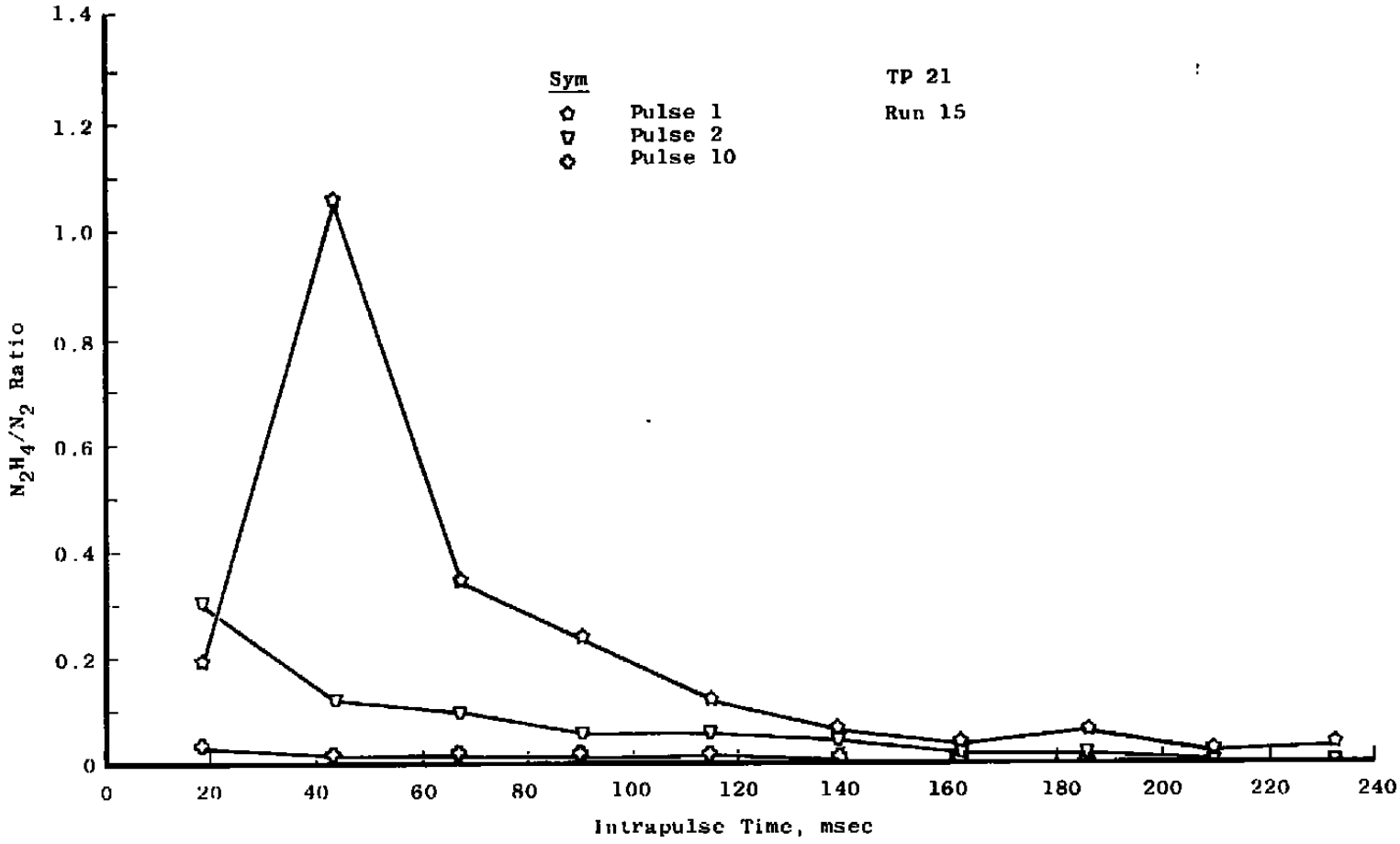

Figure 16. Intrapulse variation of the hydrazine-to-nitrogen mole fraction ratio, TC 2S.

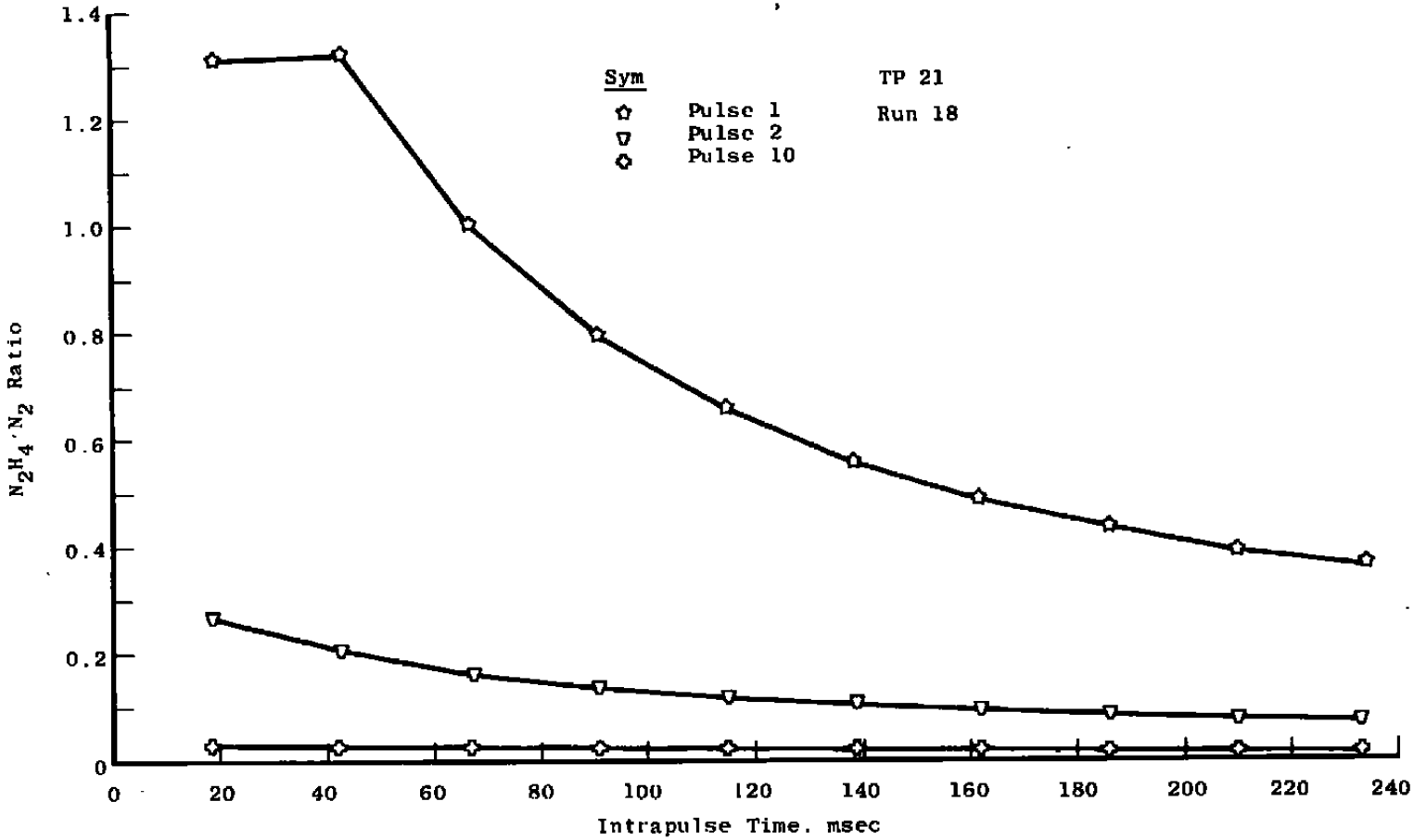

Figure 17. Intrapulse variation of the hydrazine-to-nitrogen mole fraction ratio, TC 2A..

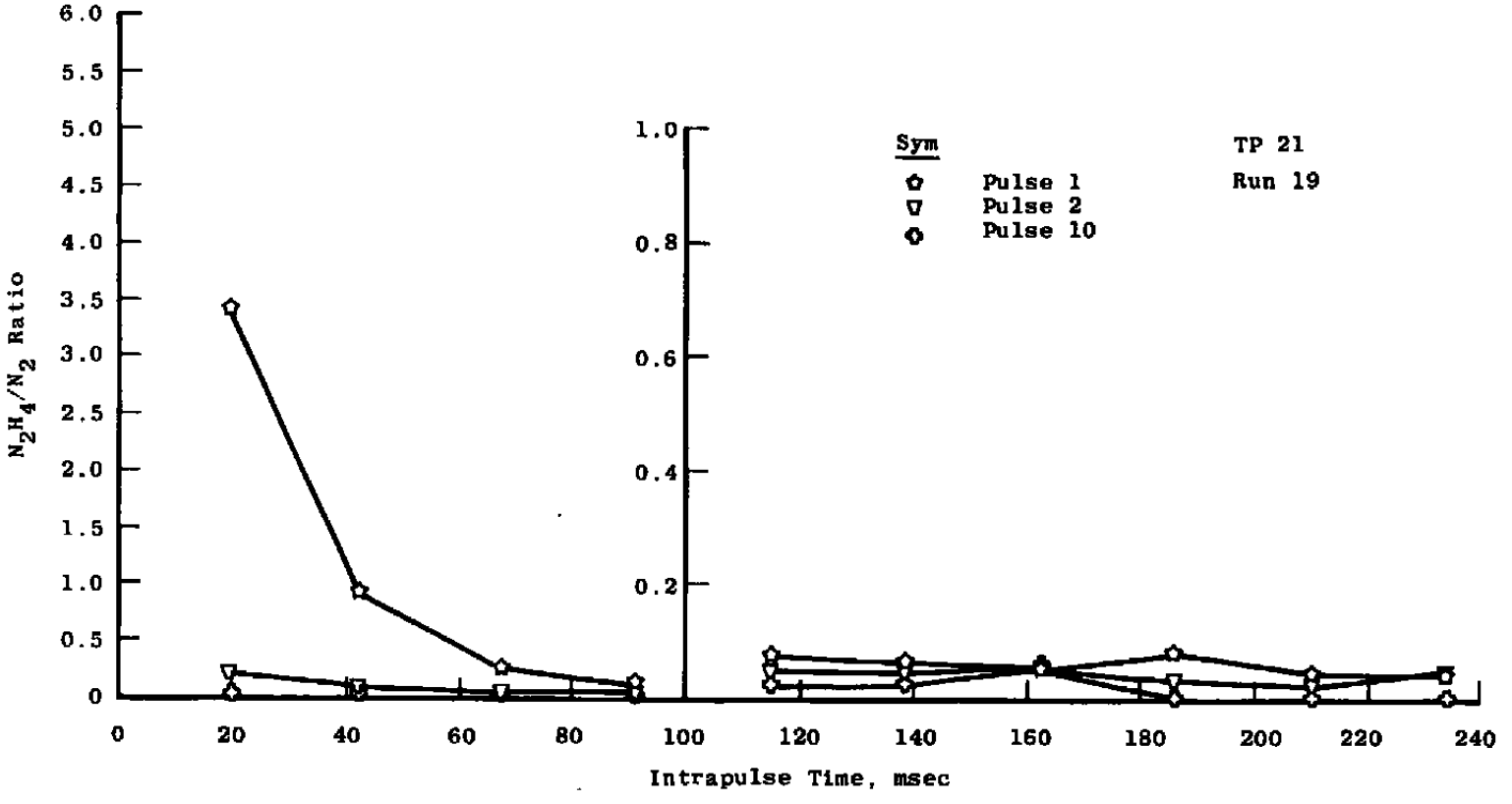

Figure 18. Intrapulse variation of the hydrazine-to-nitrogen mole fraction ratio, TC 2B.

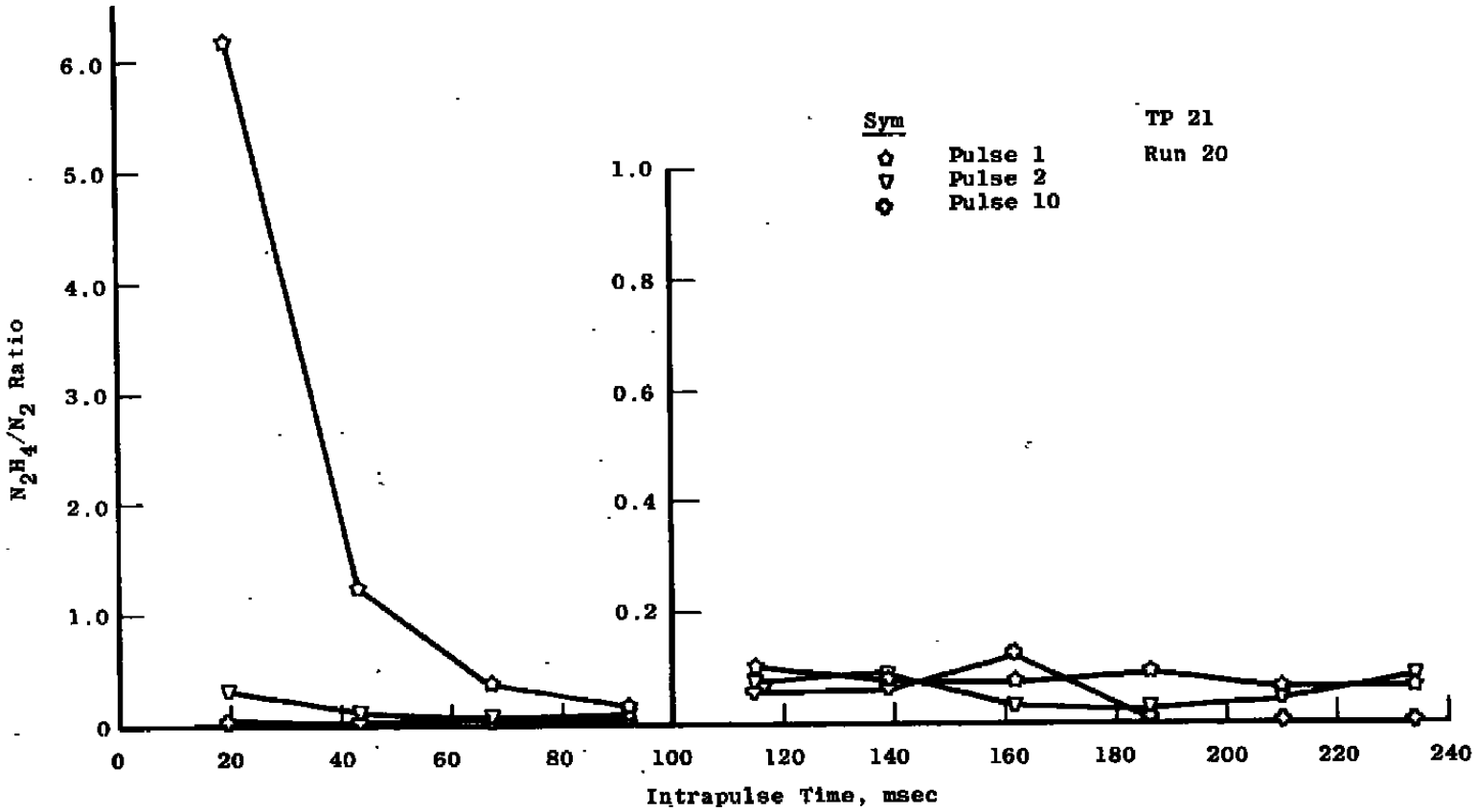

Figure 19. Intrapulse variation of the hydrazine-to-nitrogen mole fraction ratio, TC 2C.

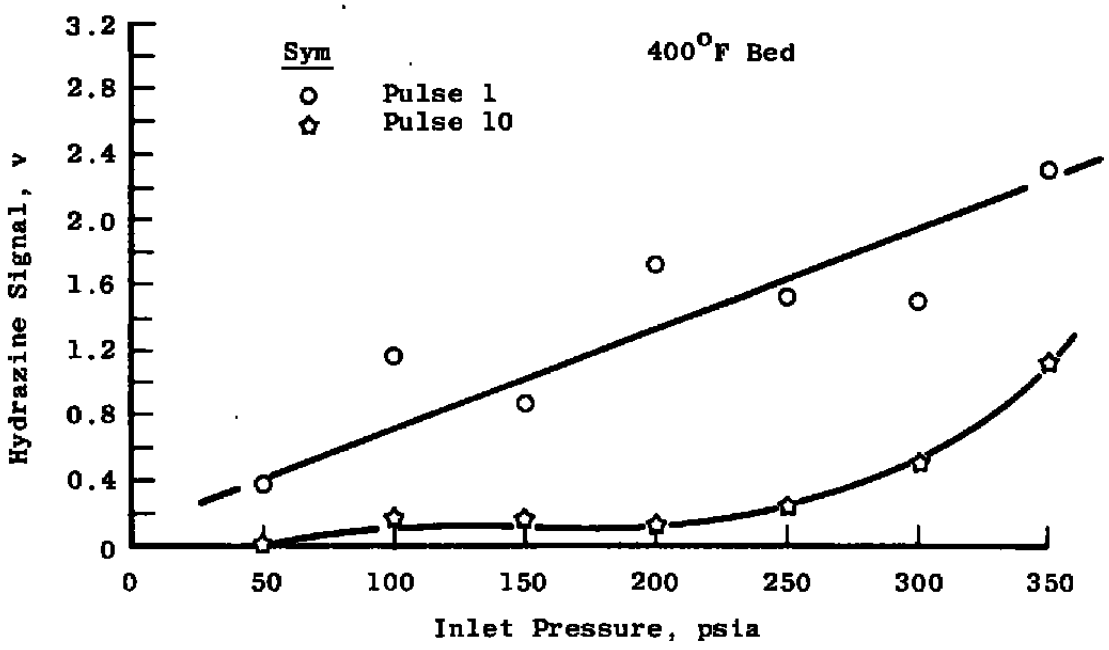

a. Hydrazine variation

Figure 20. Hydrazine and hydrazine-to-nitrogen plume centerline variations with inlet pressure.

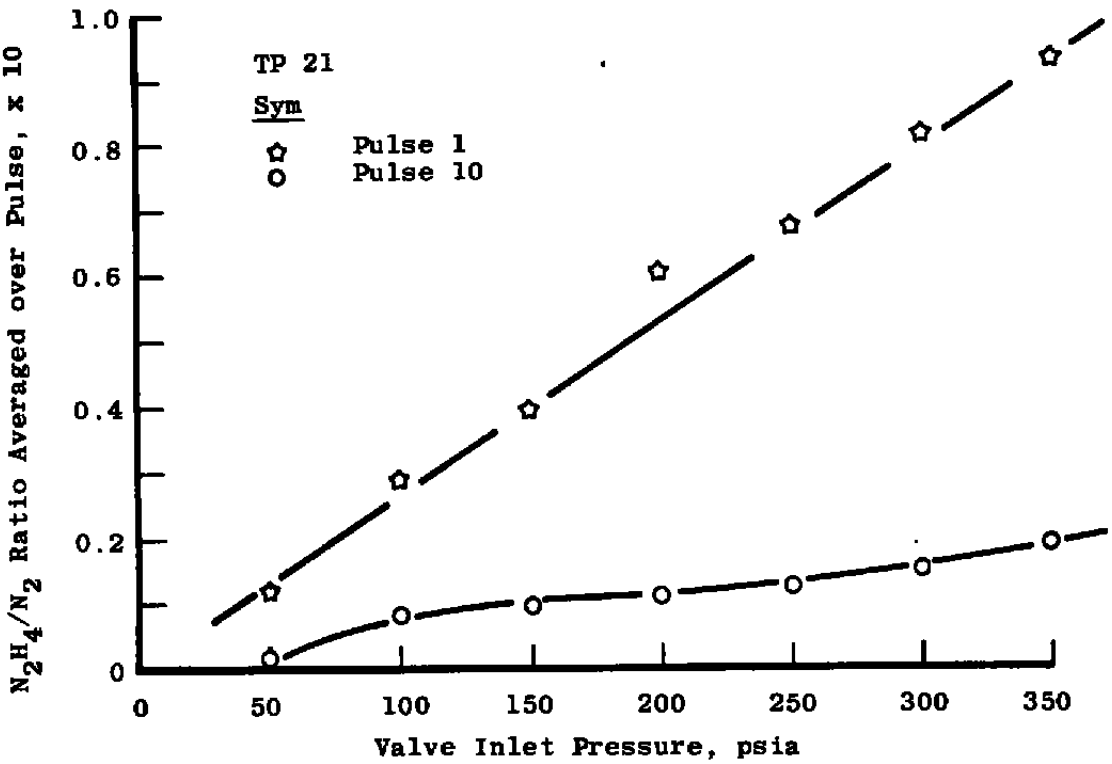

b. Hydrazine-to-nitrogen mole fraction ratio variation

Figure 20. Concluded.

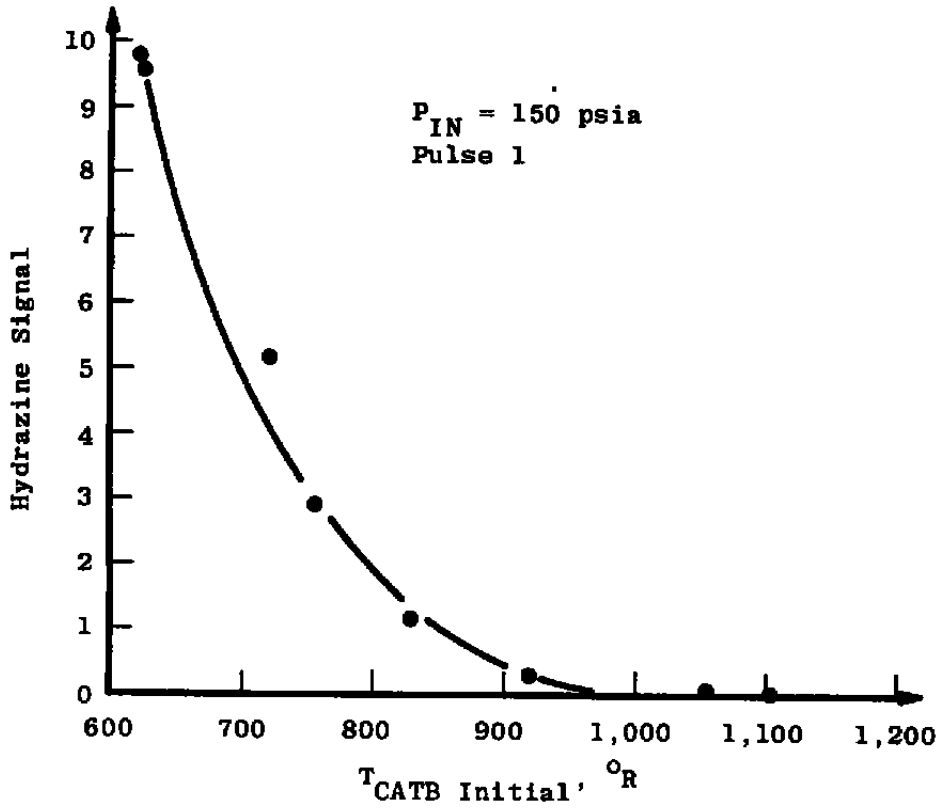

Figure 21. Variation of hydrazine on plume centerline with initial catalyst bed temperature.

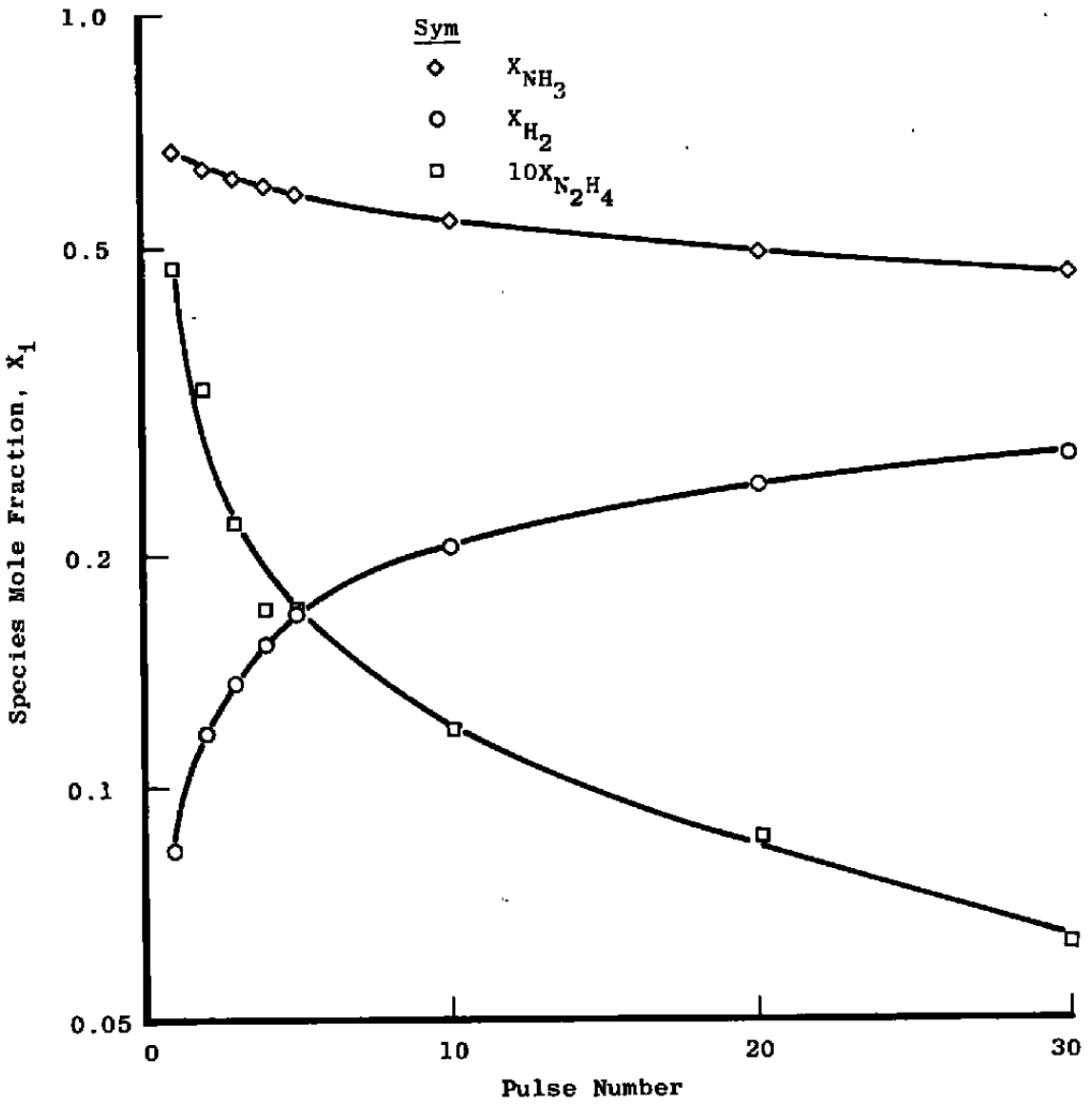

a. Mole fraction variation with pulse number, TC 2S

Figure 22. Mass spectrometer results.

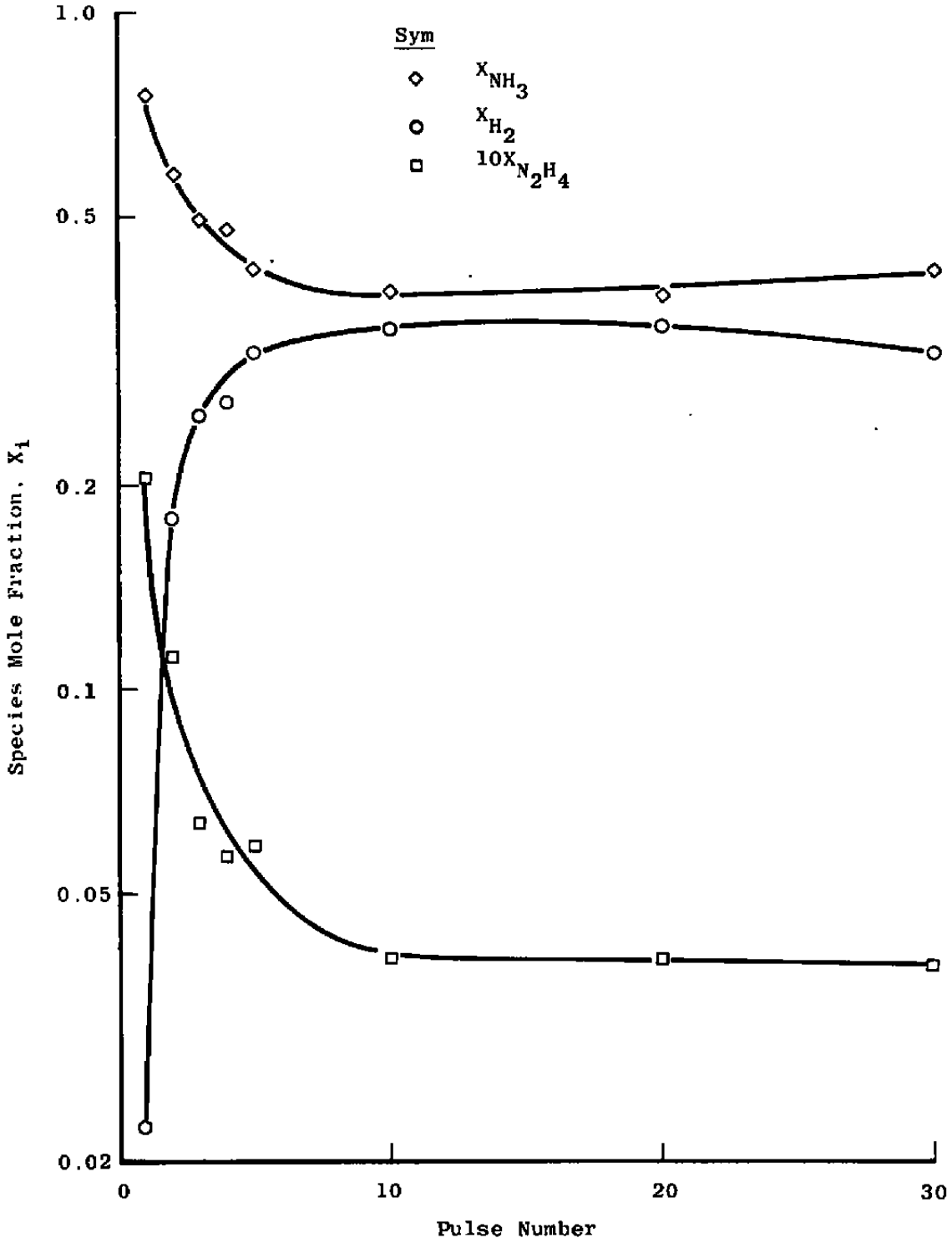

b. Mole fraction variation with pulse number, TC 2A
Figure 22. Continued.

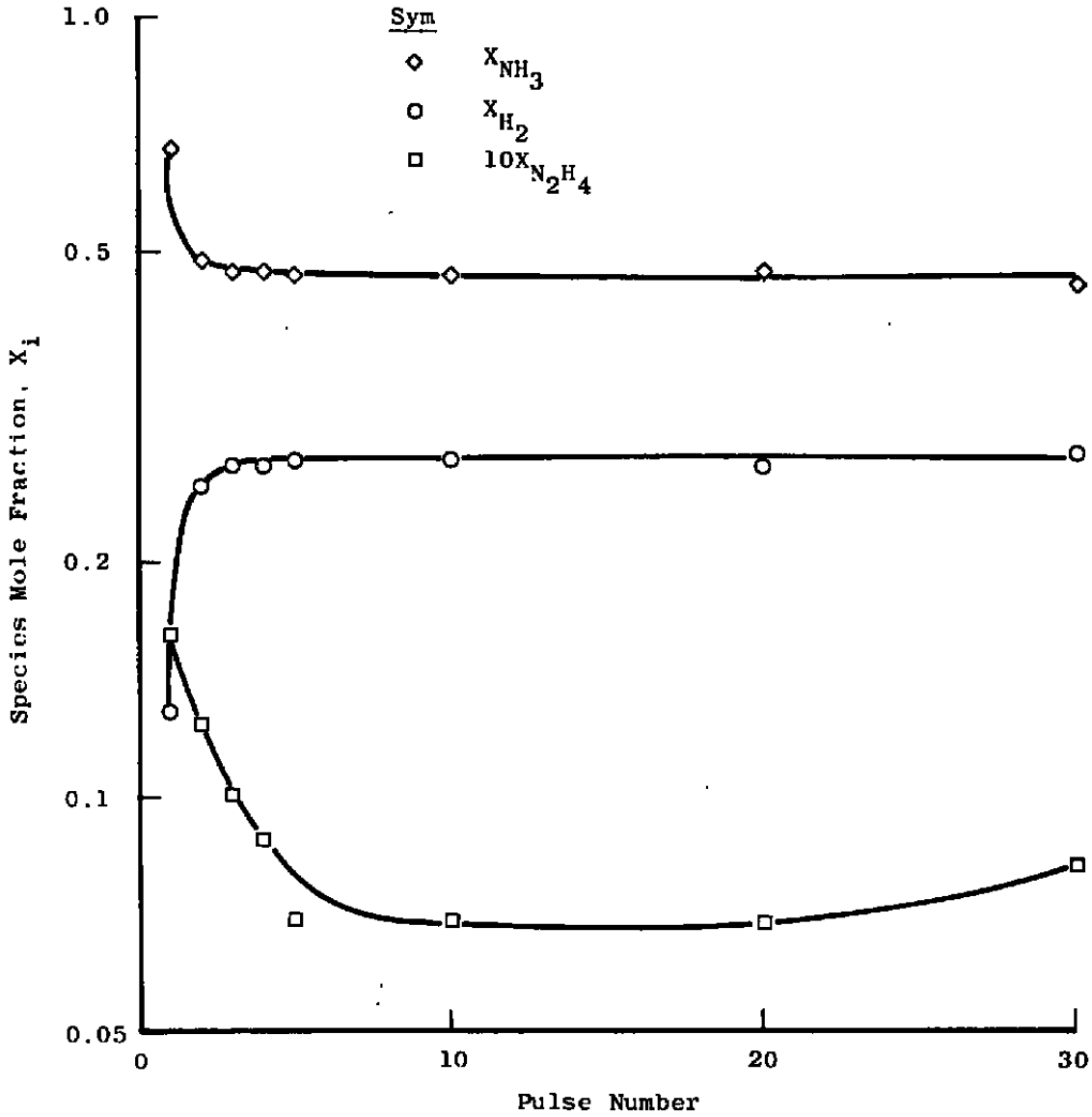

c. Mole fraction variation with pulse number, TC 2B
Figure 22. Continued.

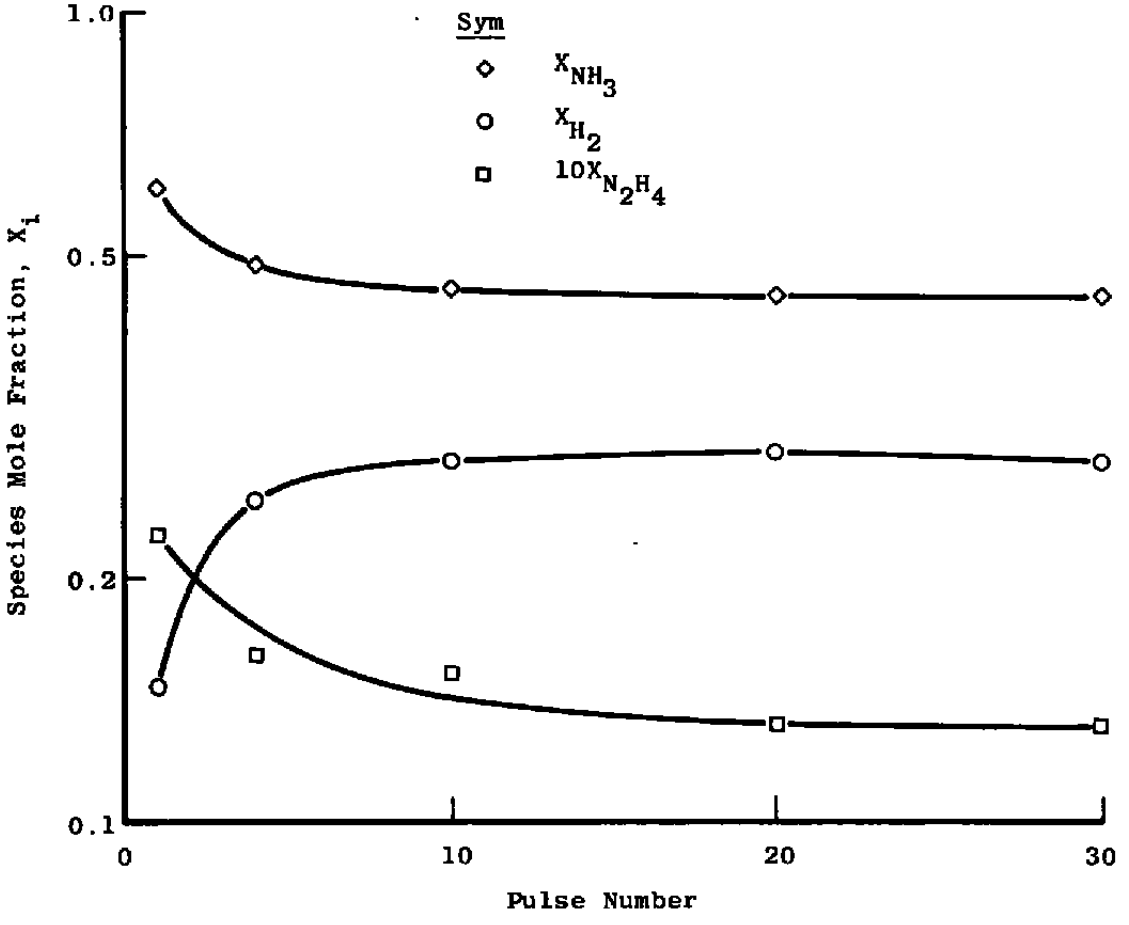

d. Mole fraction variation with pulse number, TC 2C
Figure 22. Continued.

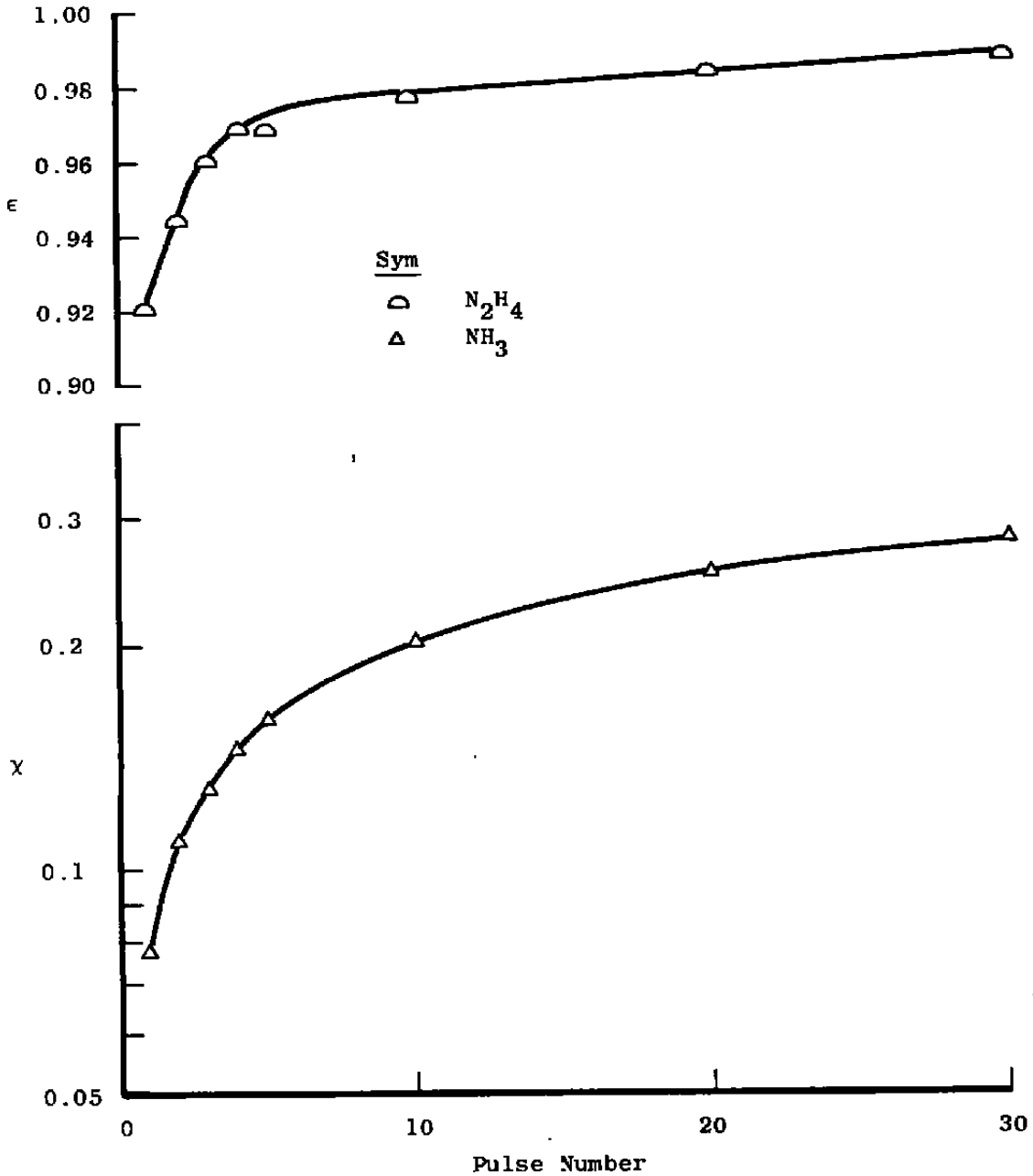

e. Variation with pulse number of degree of dissociation of N_2H_4 and NH_3, TC 2S

Figure 22. Continued.

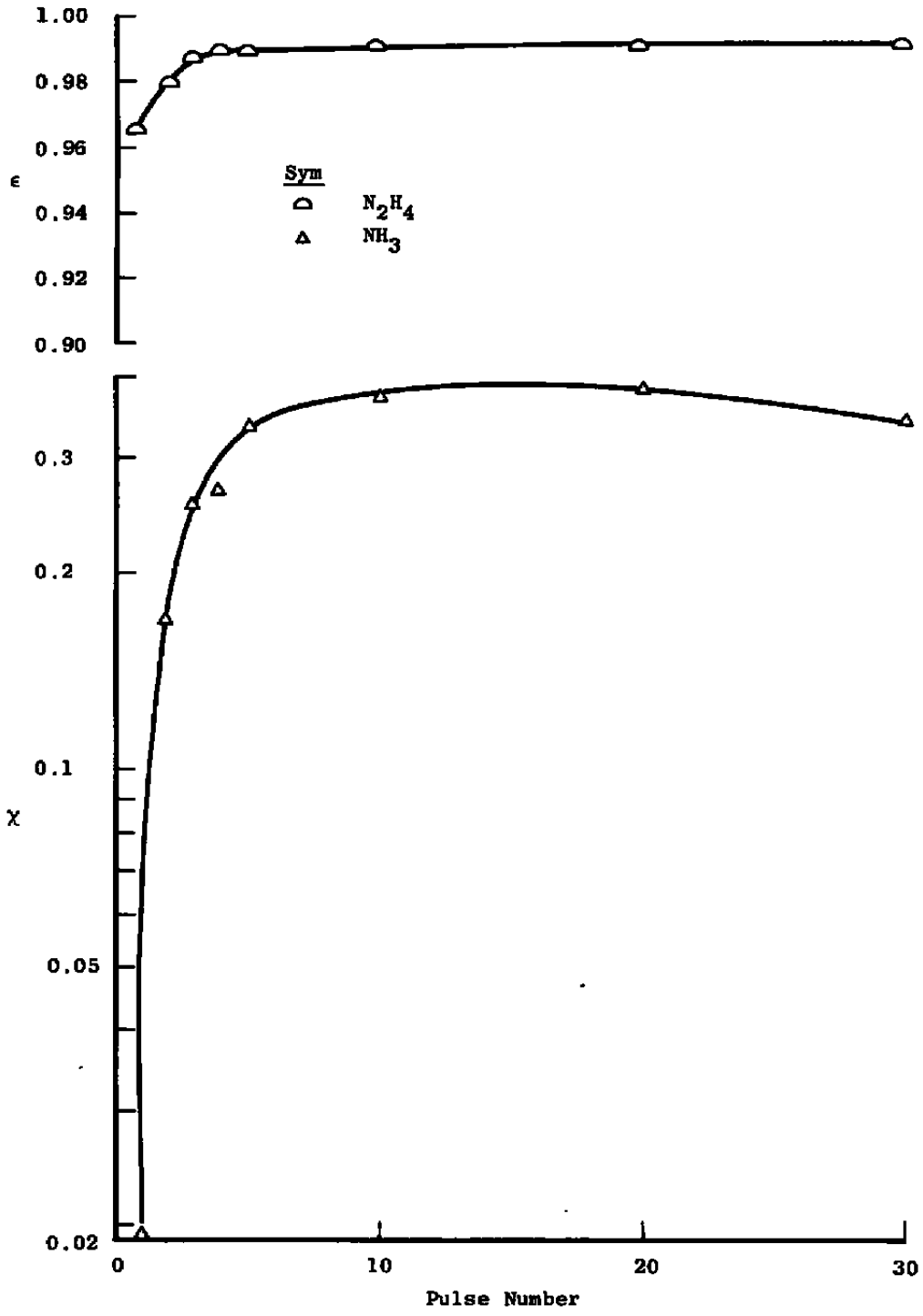

f. Variation with pulse number of degree of dissociation of N_2H_4 and NH_3, TC 2A

Figure 22. Continued.

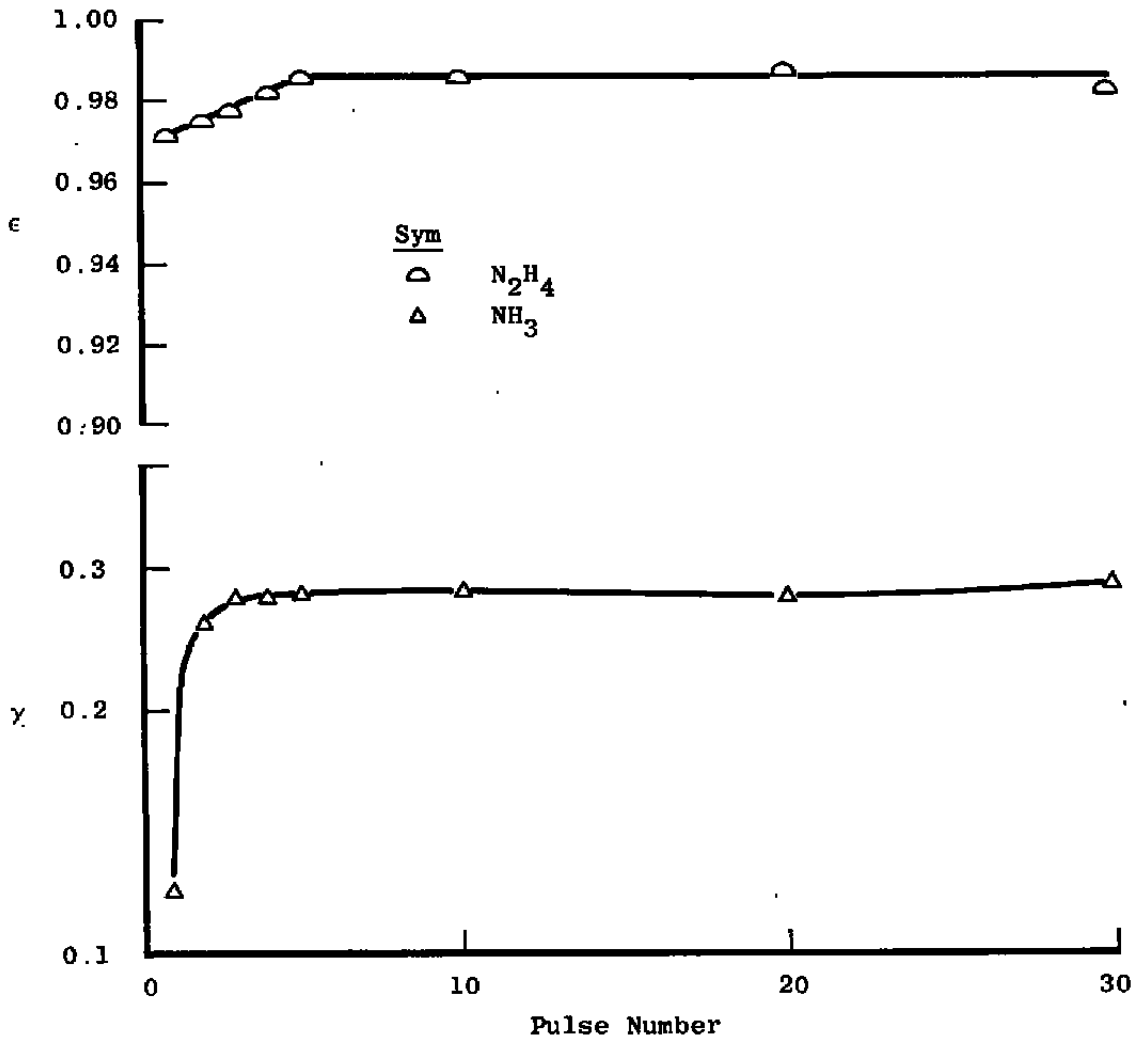

g. Variation with pulse number of degree of dissociation of N_2H_4 and NH_3, TC 2B

Figure 22. Continued.

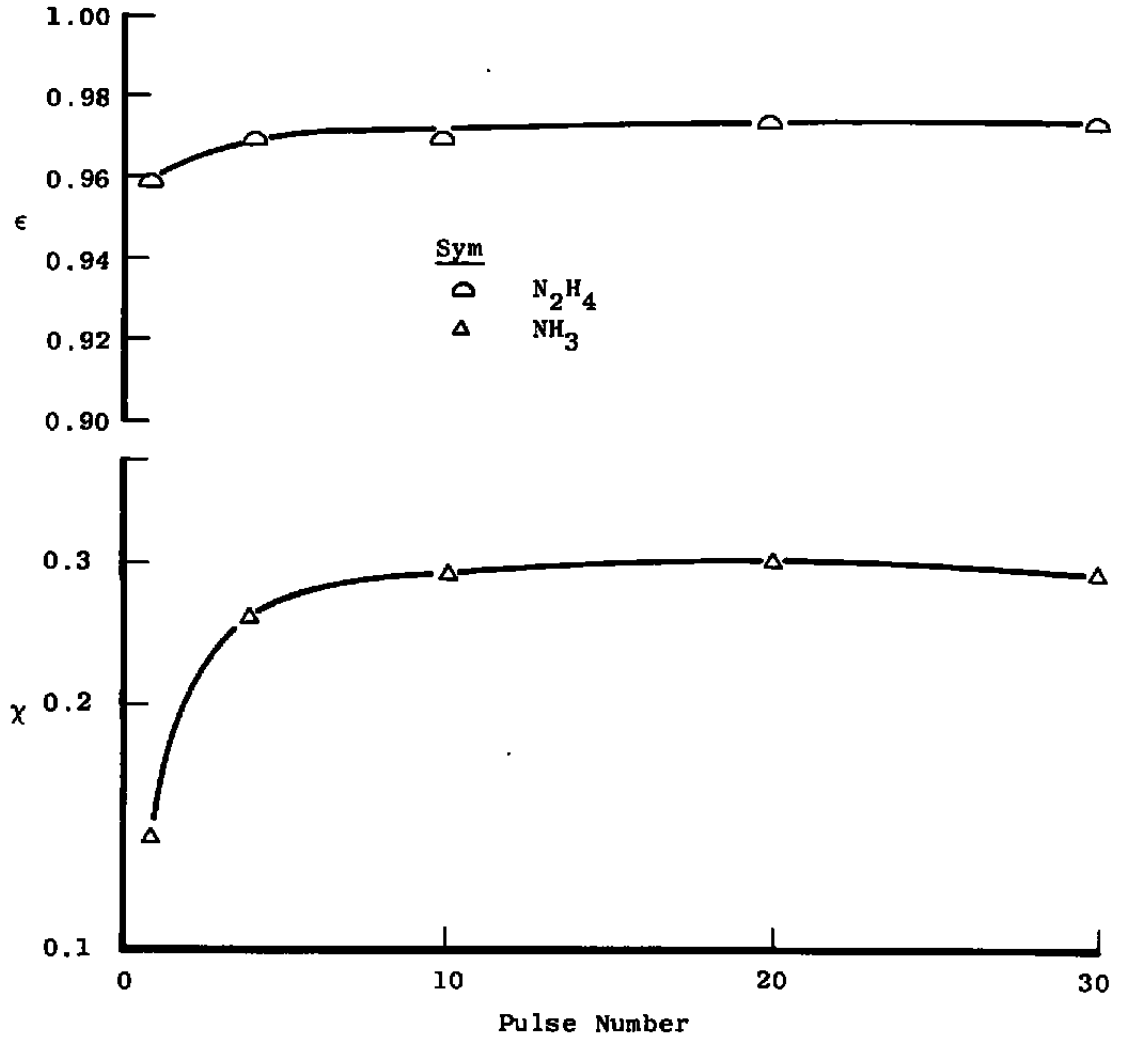

h. Variation with pulse number of degree of dissociation of N_2H_4 and NH_3, TC 2C

Figure 22. Continued.

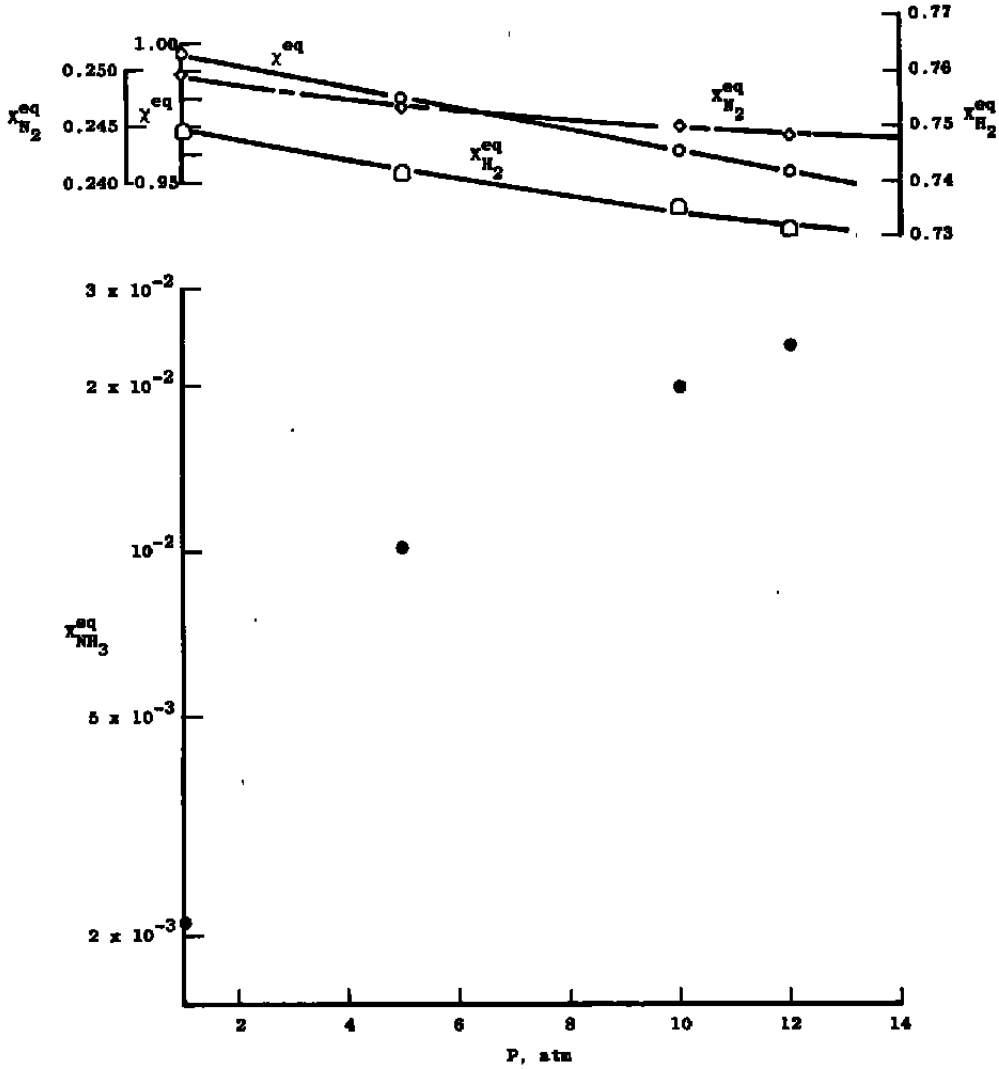

i. Pressure variation of equilibrium properties of dissociating NH_3

Figure 22. Continued.

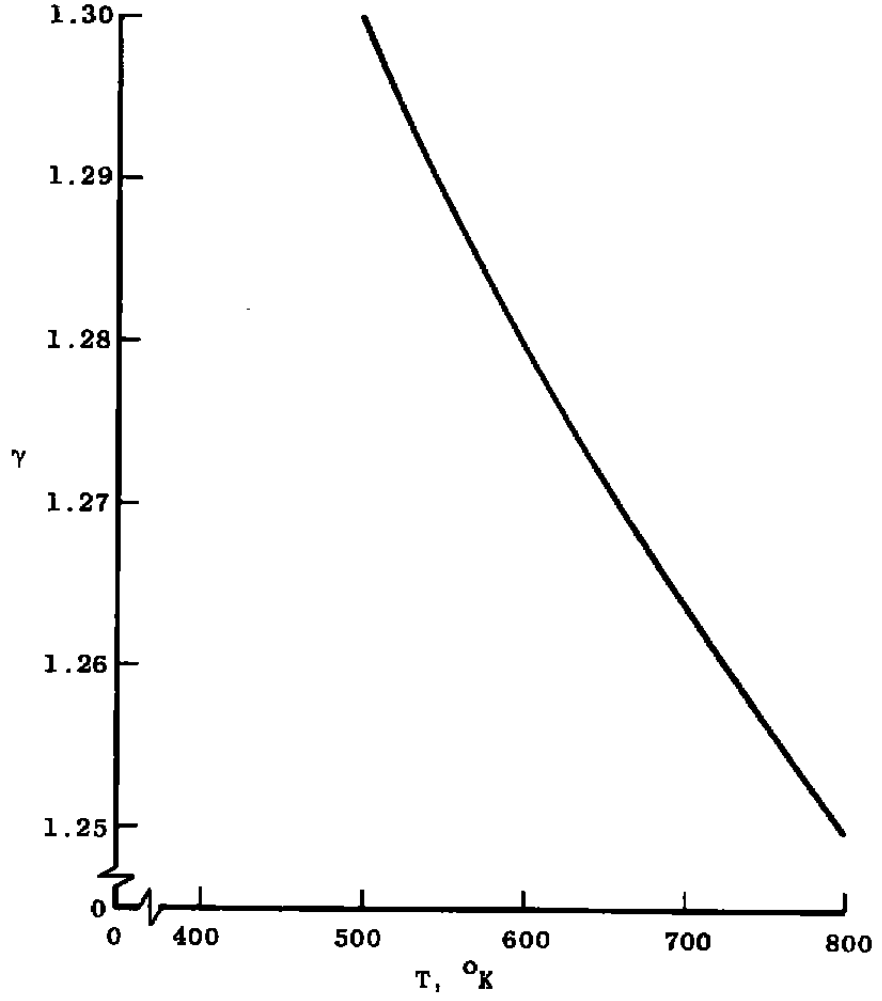

j. Temperature variation of specific heat ratio for Pulse 1 of TC 2C

Figure 22. Continued.

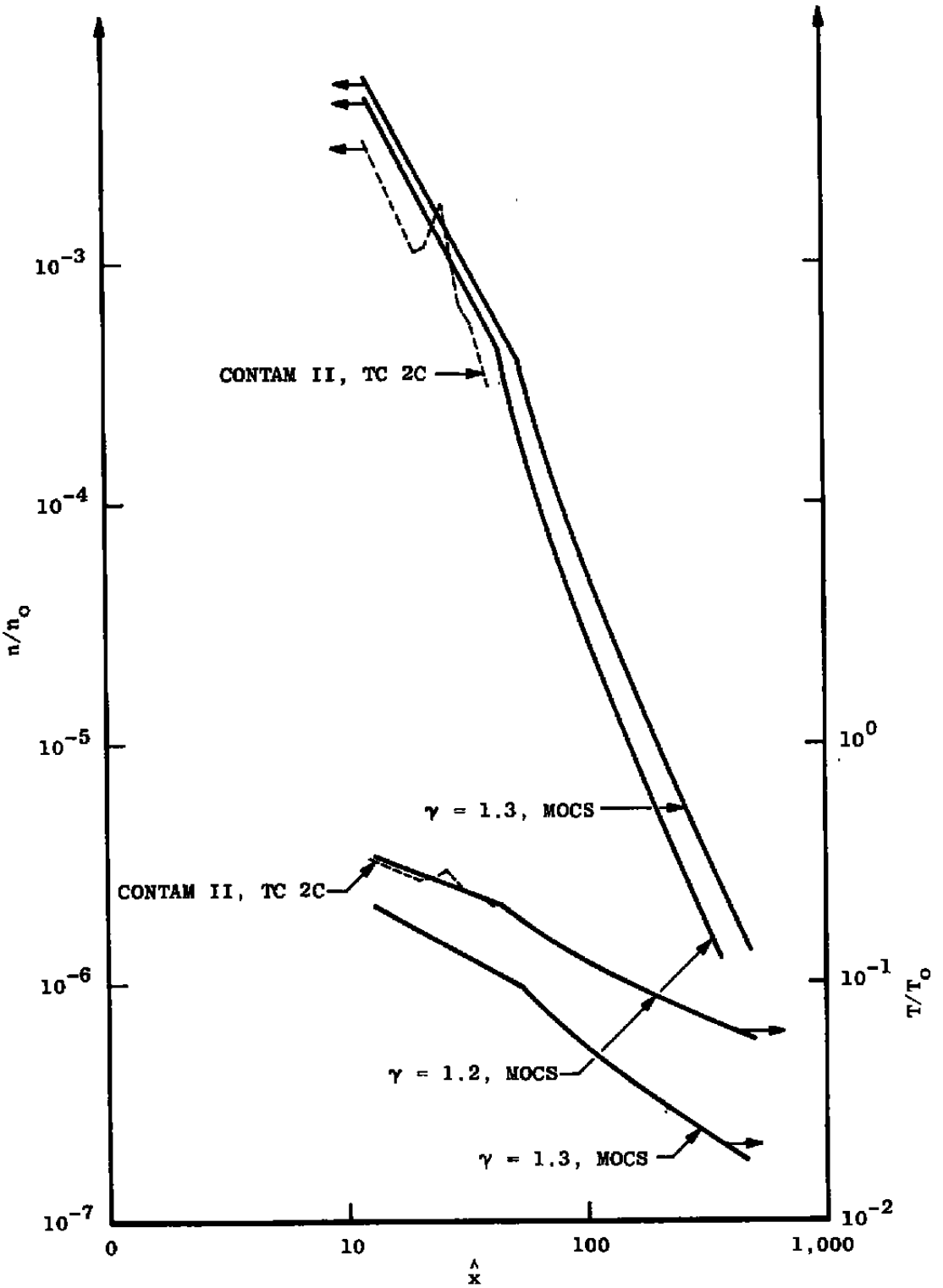

k. Theoretical predictions of the axial variation of plume number density and temperature

Figure 22. Concluded.

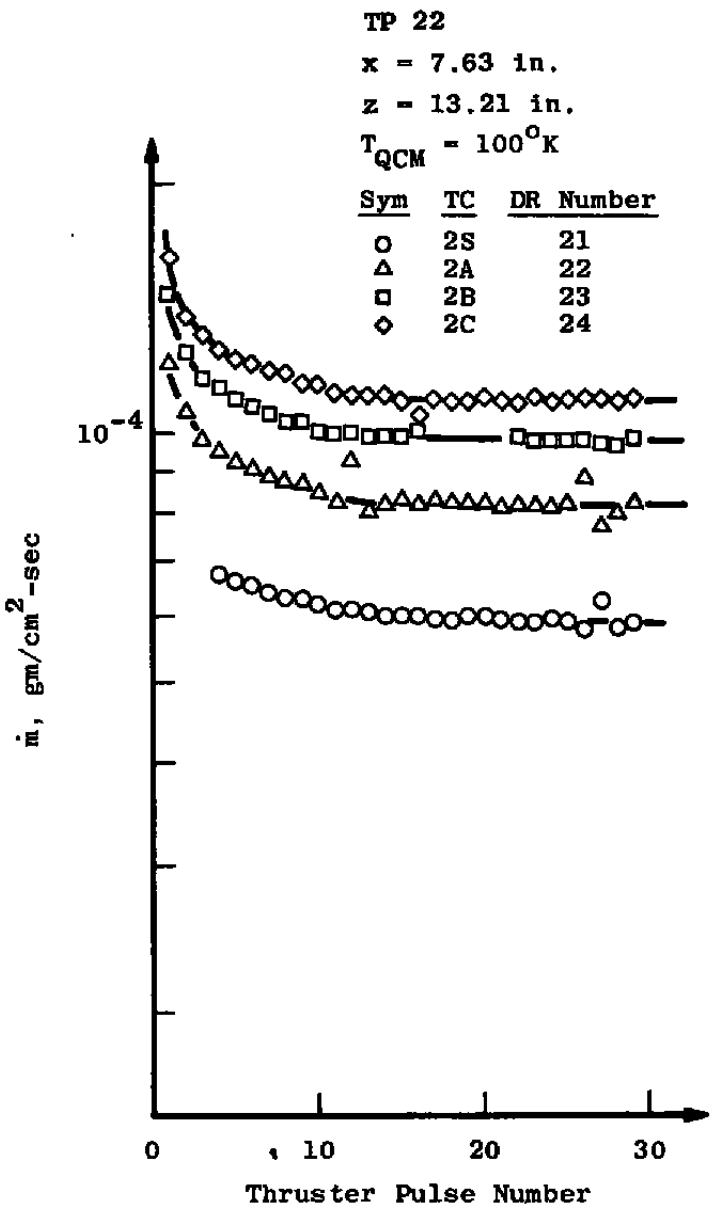

Figure 23. Mass deposition rate versus pulse number for TC's 2S, 2A, 2B, and 2C, T_{QCM} = 100°K.

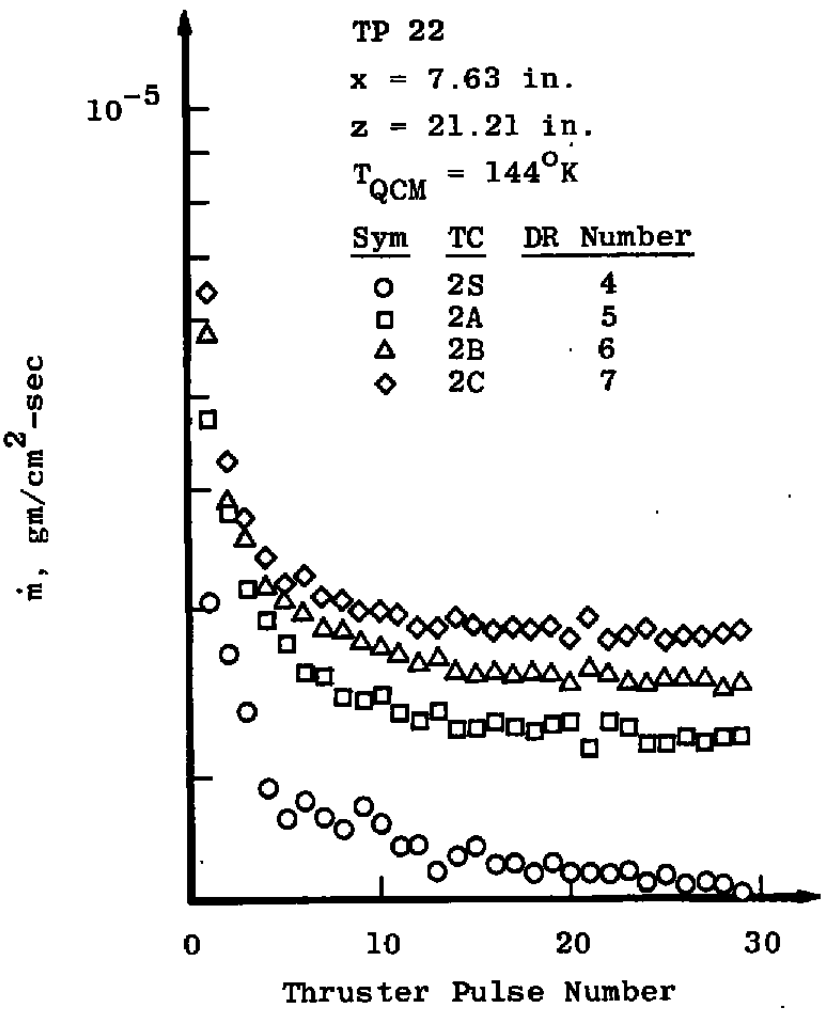

Figure 24. Mass deposition rate versus pulse number for TC's 2S, 2A, 2B, and 2C, T_{QCM} = 144°K.

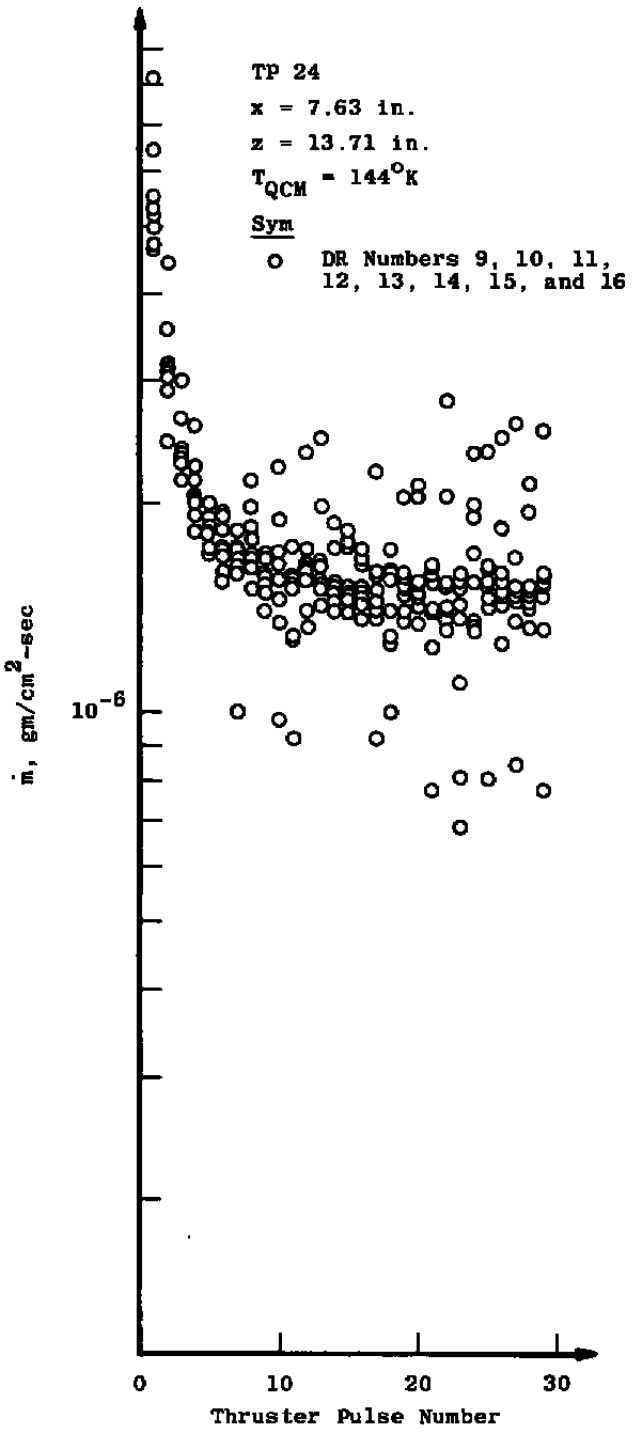

Figure 25. Mass deposition rate versus pulse number for several pulse sequences at TC 2A, T_{QCM} = 144°K.

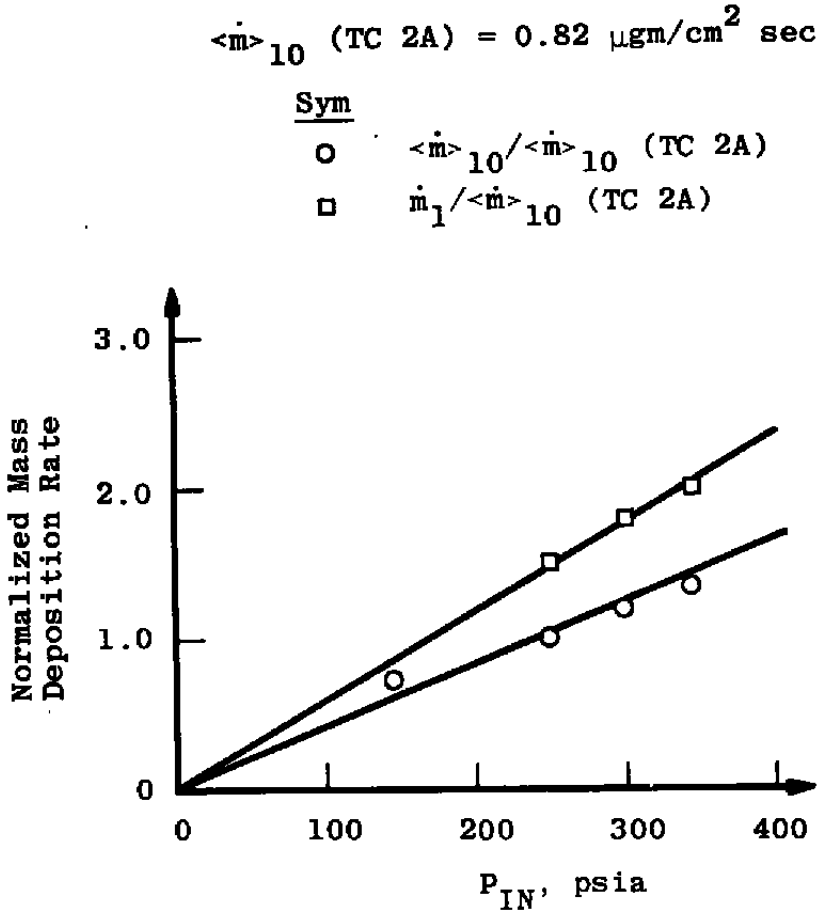

Figure 26. Normalized mass deposition rates as a function of inlet pressure, T_{QCM} = 100°K, θ = 30.01 deg.

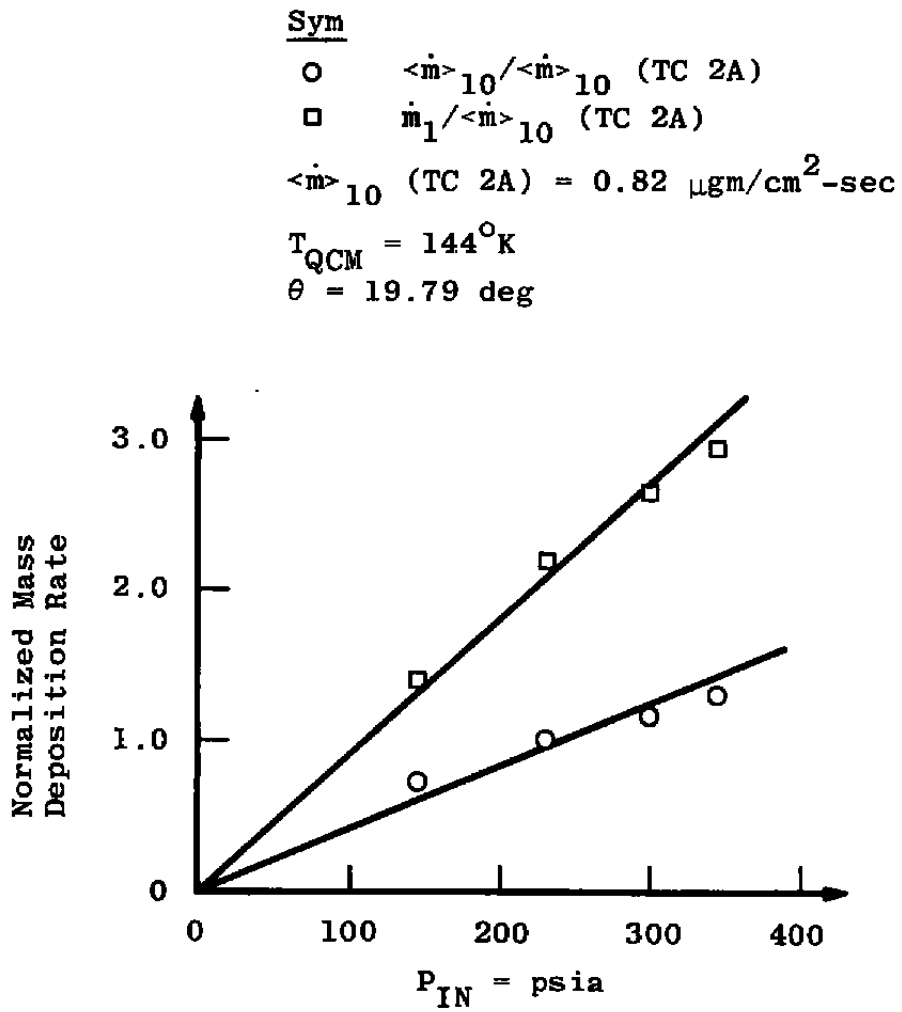

Figure 27. Normalized mass deposition rates as a function of inlet pressure, T_{QCM} = 144°K, θ = 19.79 deg.

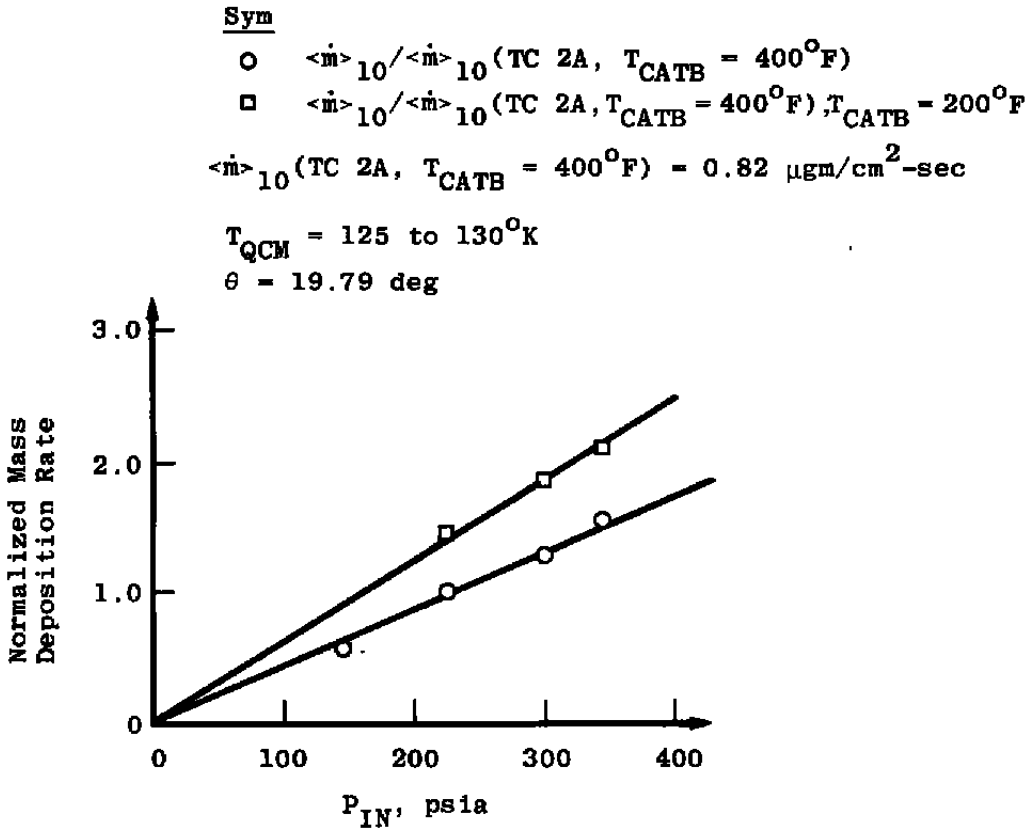

Figure 28. Normalized mass deposition rates as a function of inlet pressure, for initial catalyst bed temperatures of 200 and 400°F T_{QCM} = 125 to 130°K, θ =19.79 deg.

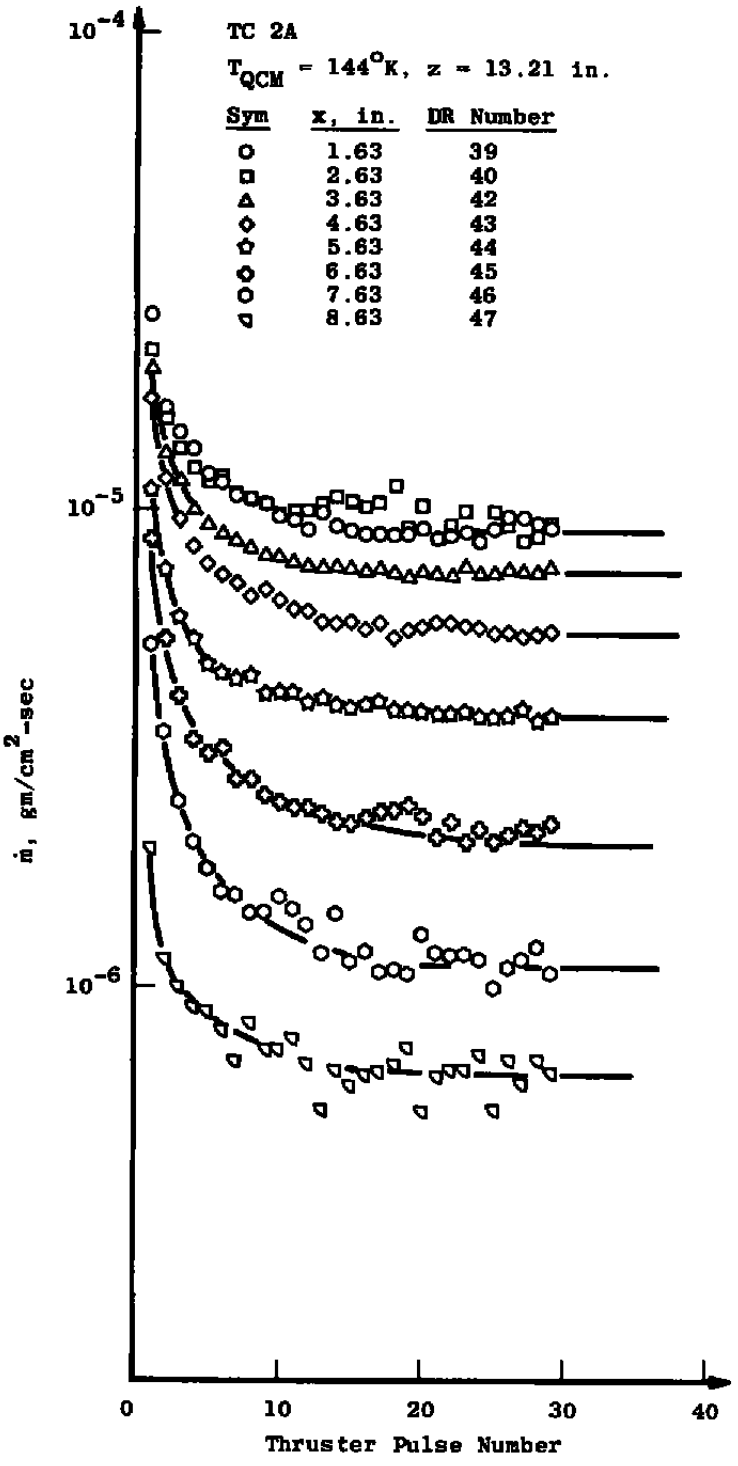

Figure 29. Mass deposition rate versus pulse number for several thruster positions, TC 2A, T_{QCM} = 144°K.

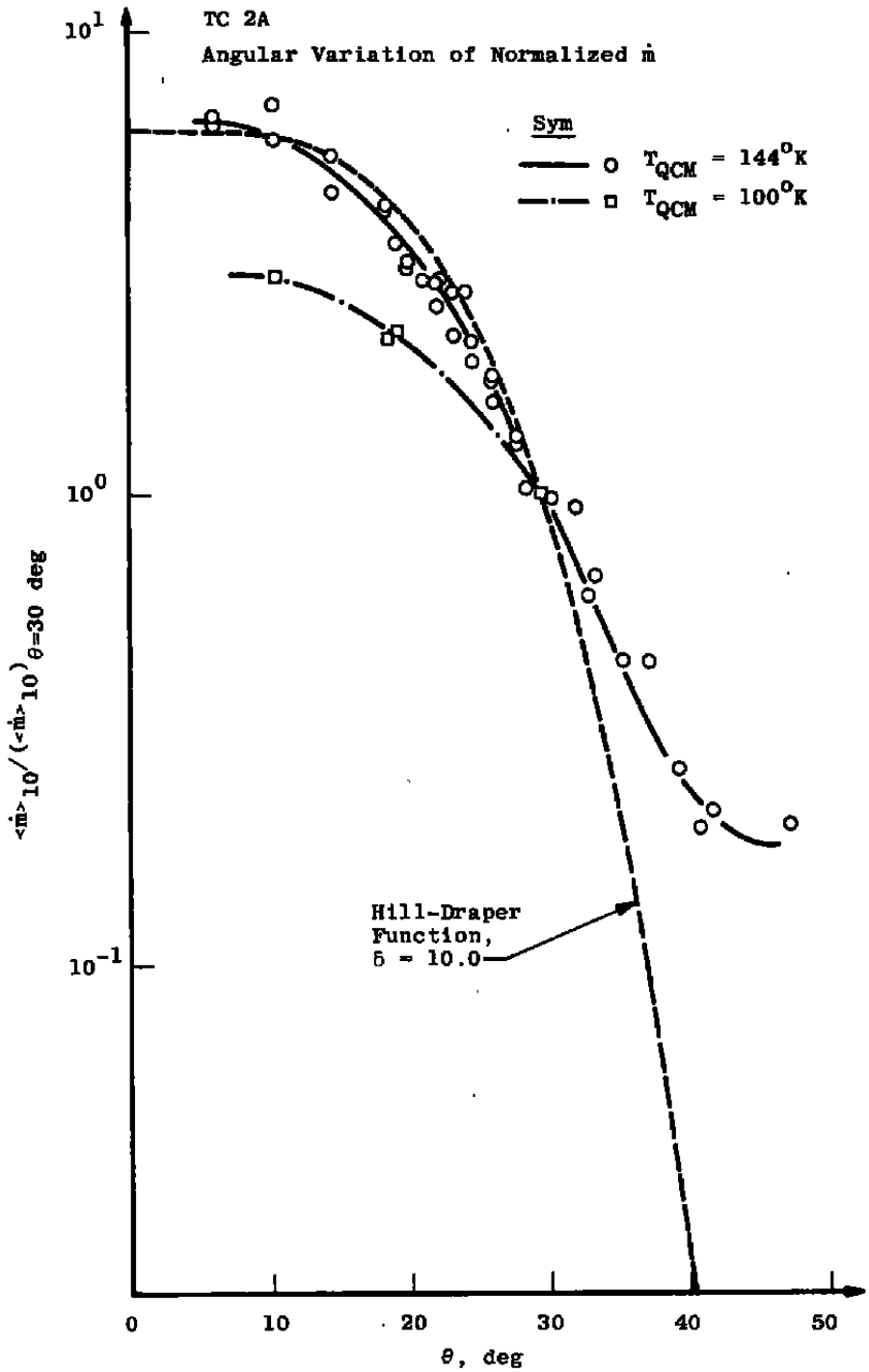

Figure 30. Normalized angular variation of mass deposition rate.

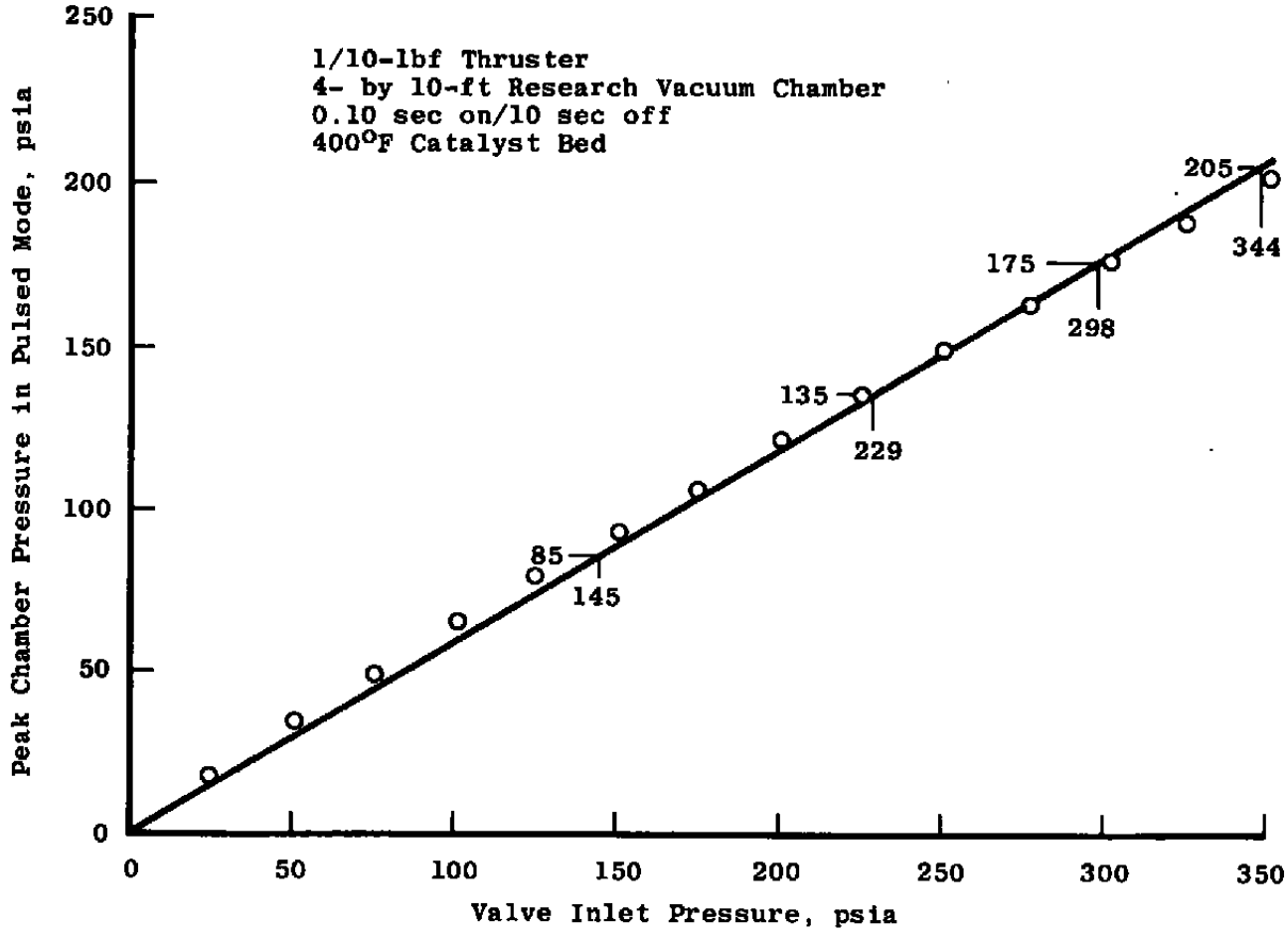

Figure 31. Thruster calibration, T_{CATB} = 478°K (400°F).

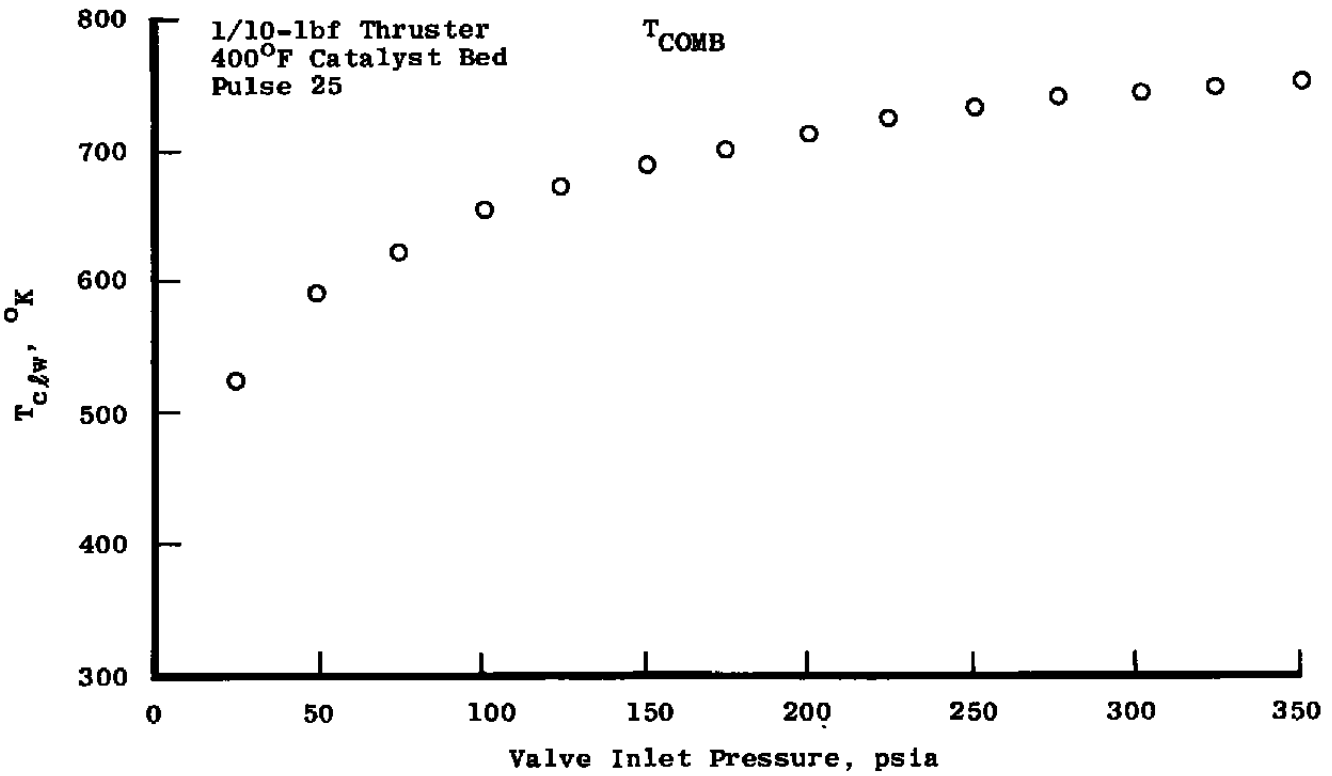

Figure 32. Variation of catalyst bed lower wall temperature with inlet pressure.

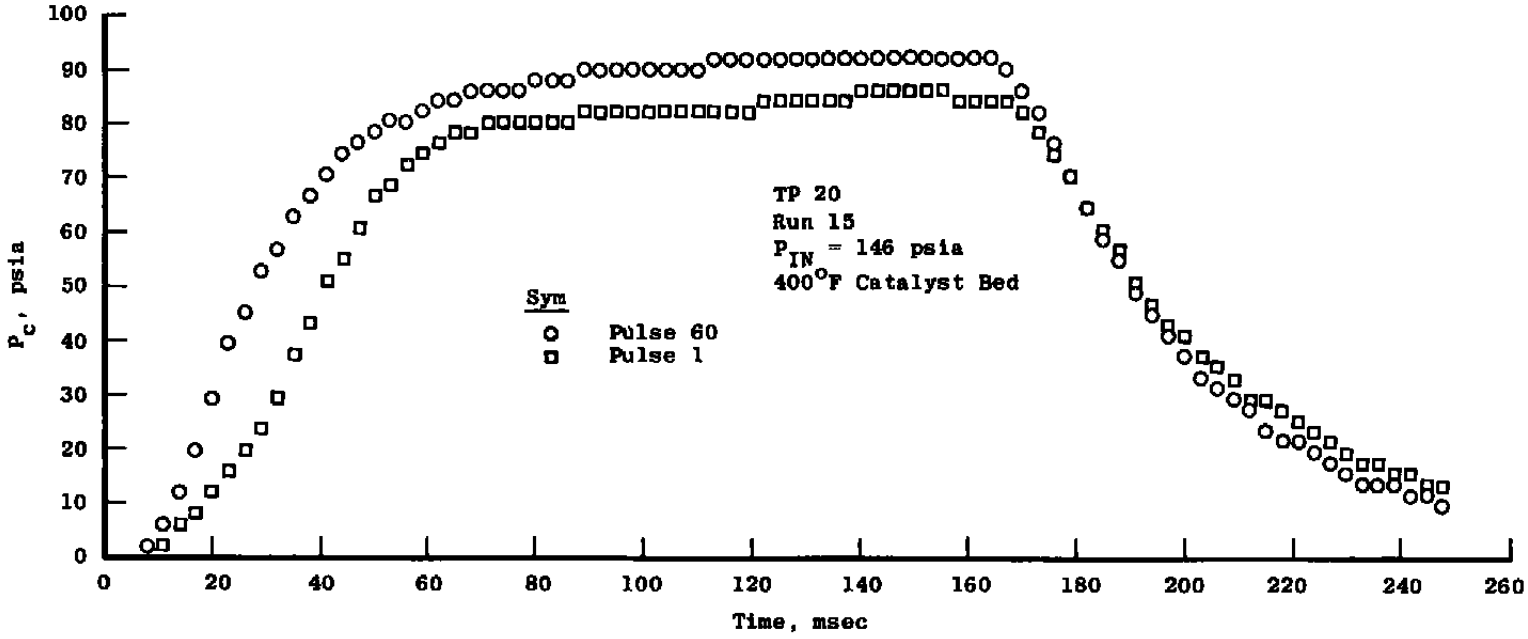

Figure 33. Thruster pulse shape for P_{IN} = 146 psia.

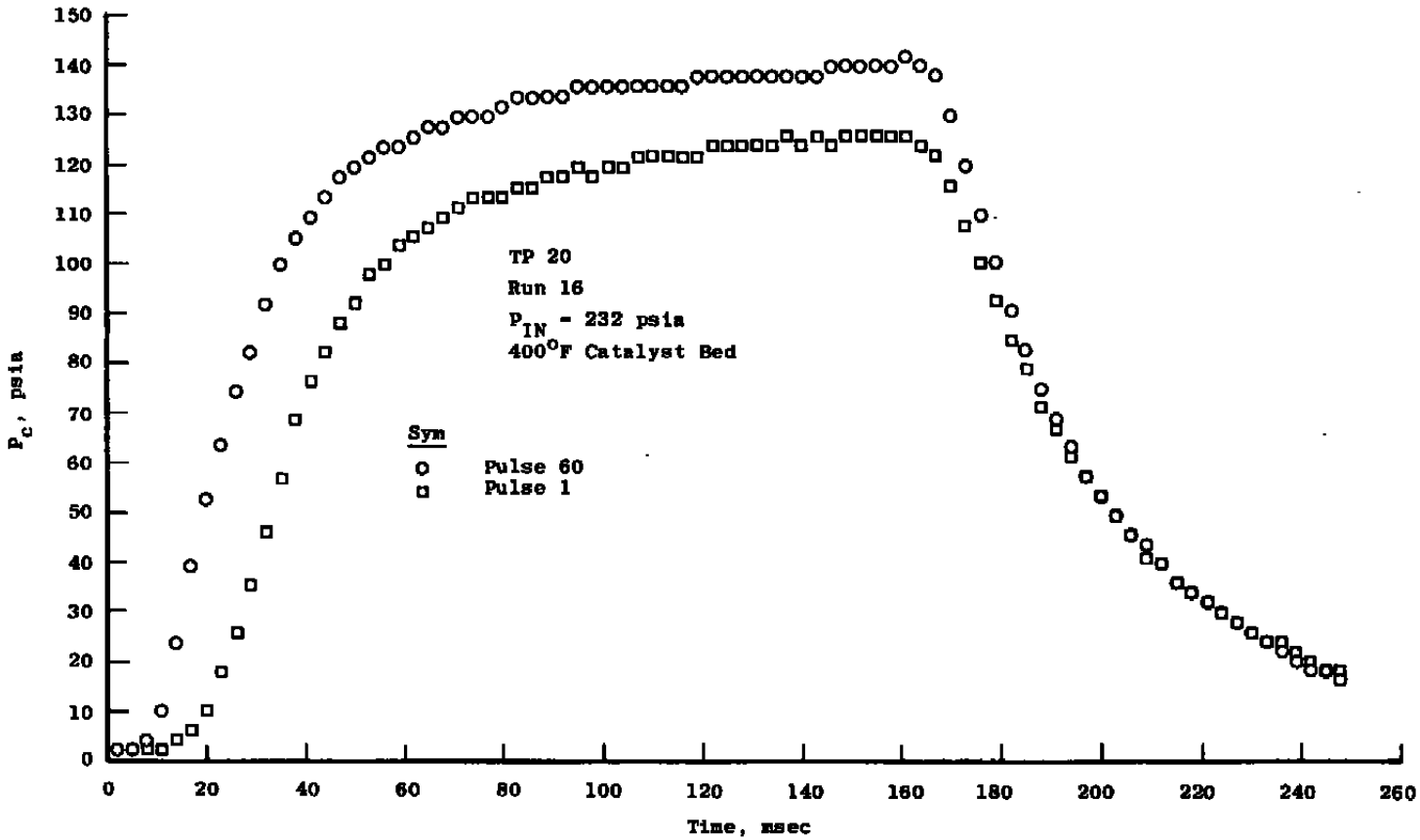

Figure 34. Thruster pulse shape for P_{IN} = 232 psia.

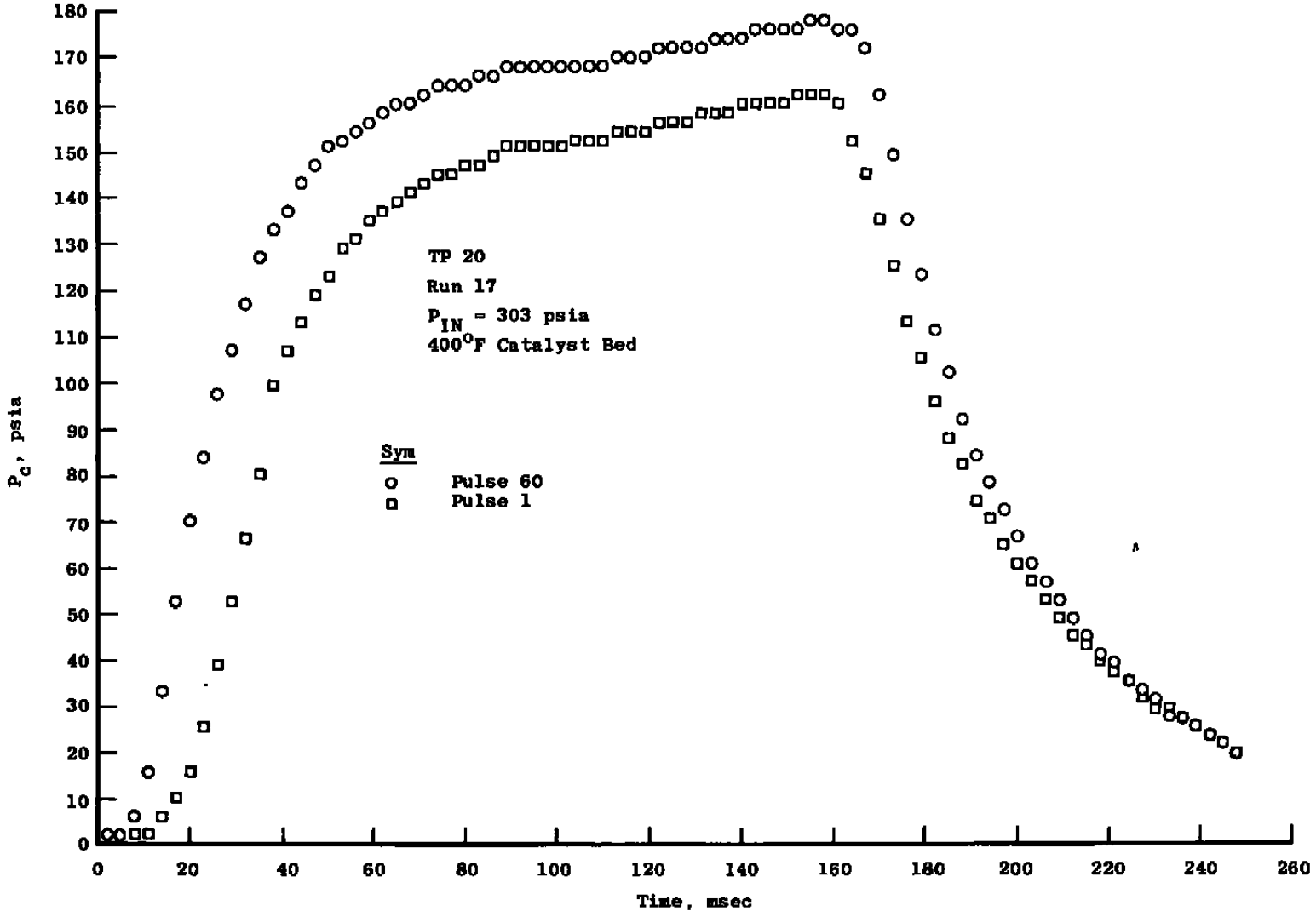

Figure 35. Thruster pulse shape for P_{IN} = 303 psia.

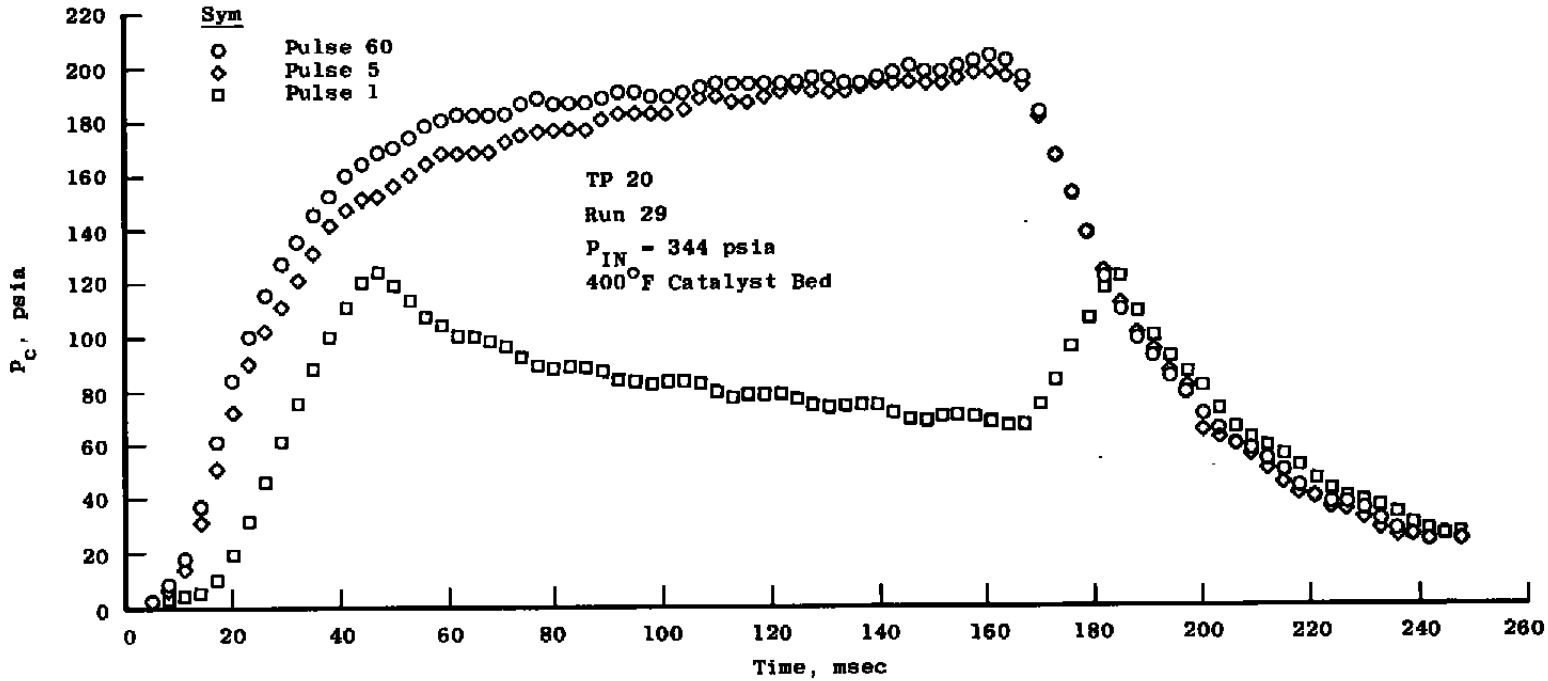

Figure 36. Thruster pulse shape for P_{IN} = 344 psia.

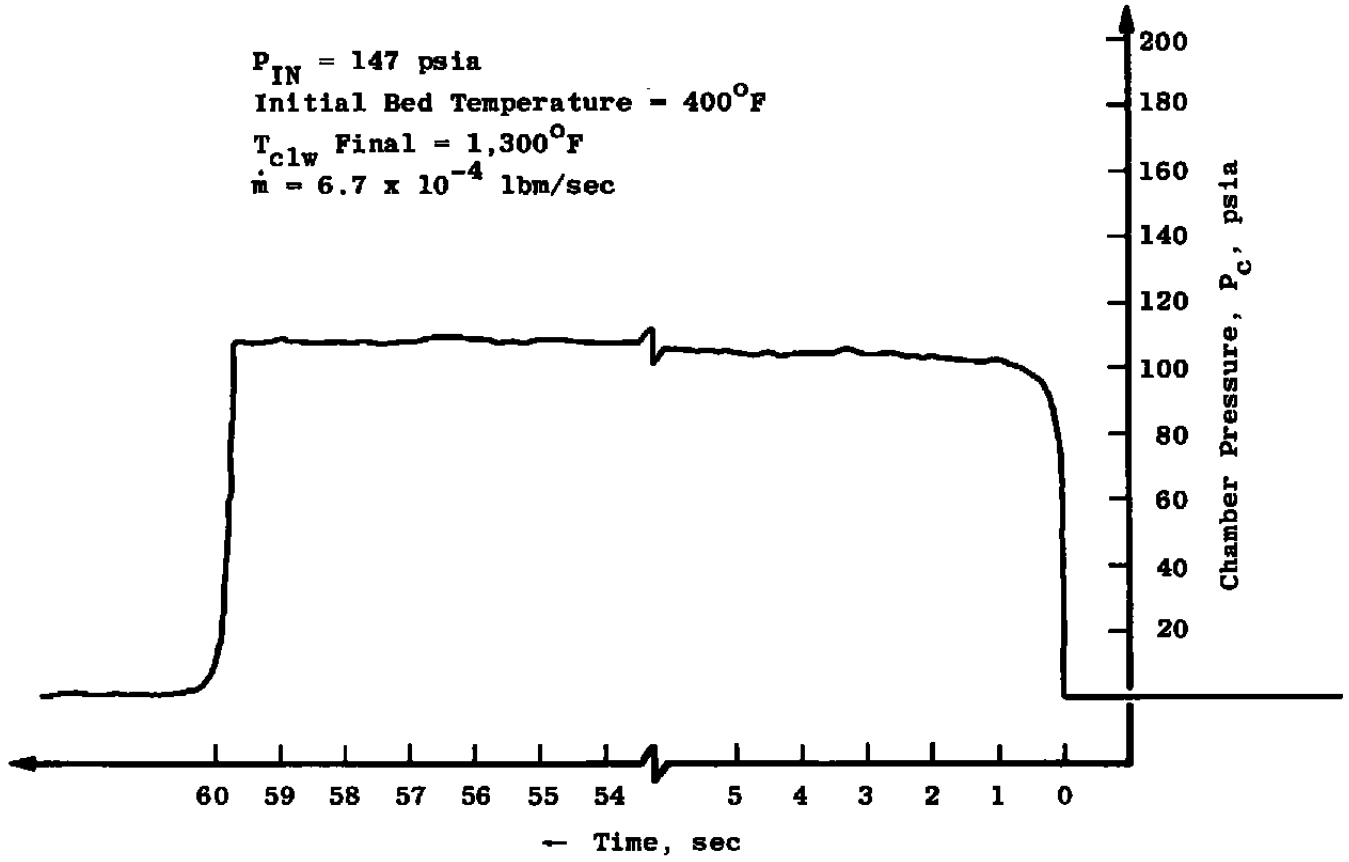

Figure 37. Thruster chamber pressure for a steady-state firing, P_{IN} = 147 psia.

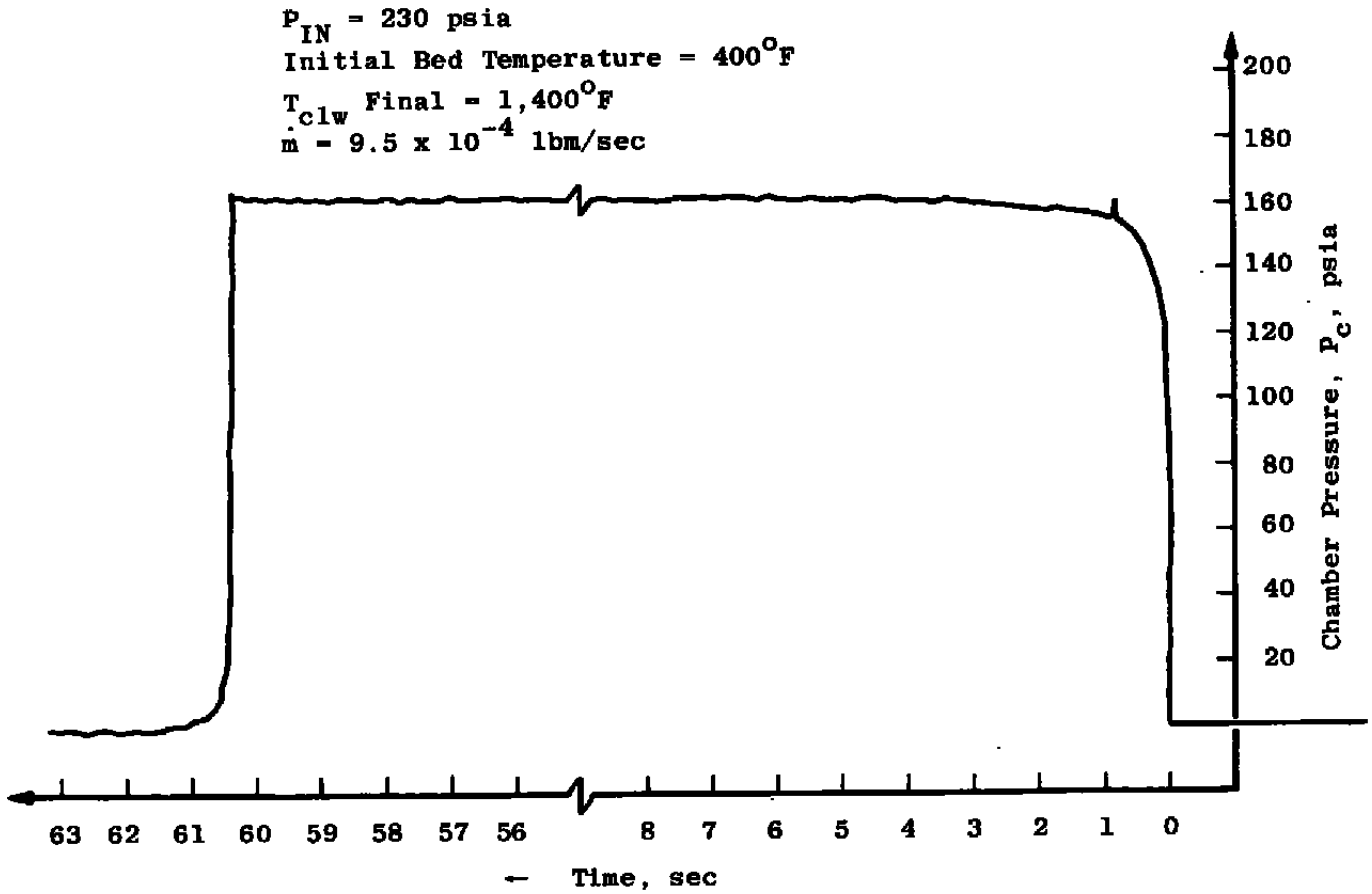

Figure 38. Thruster chamber pressure for a steady-state firing, P_{IN} = 230 psia.

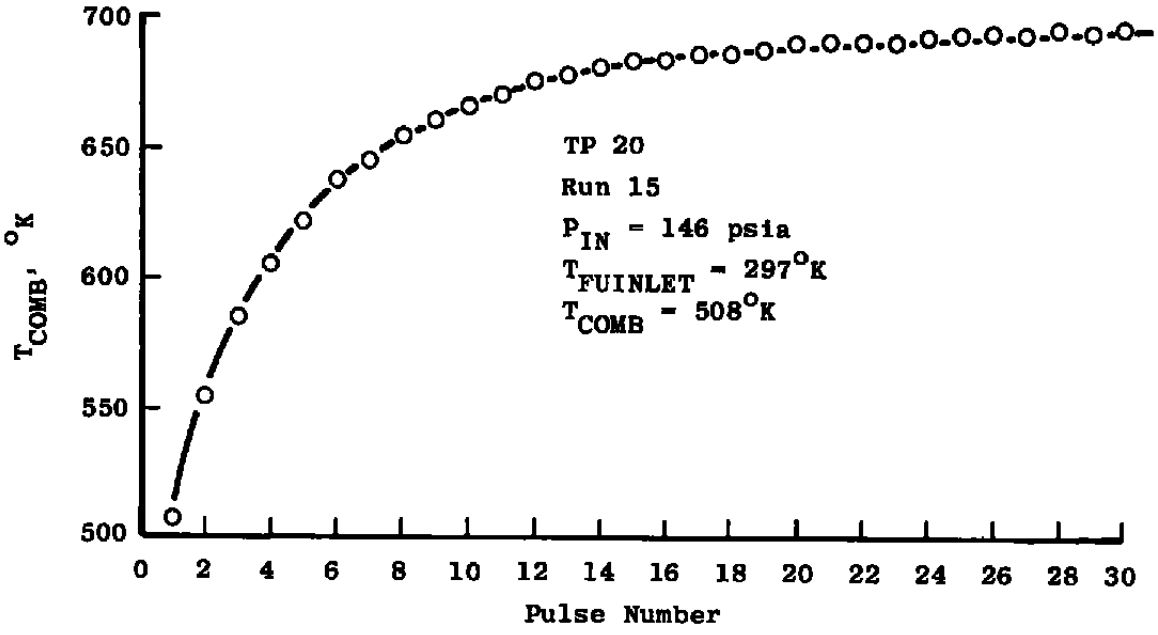

Figure 39. Catalyst bed temperature T_{COMB}, versus pulse number, TC 2S.

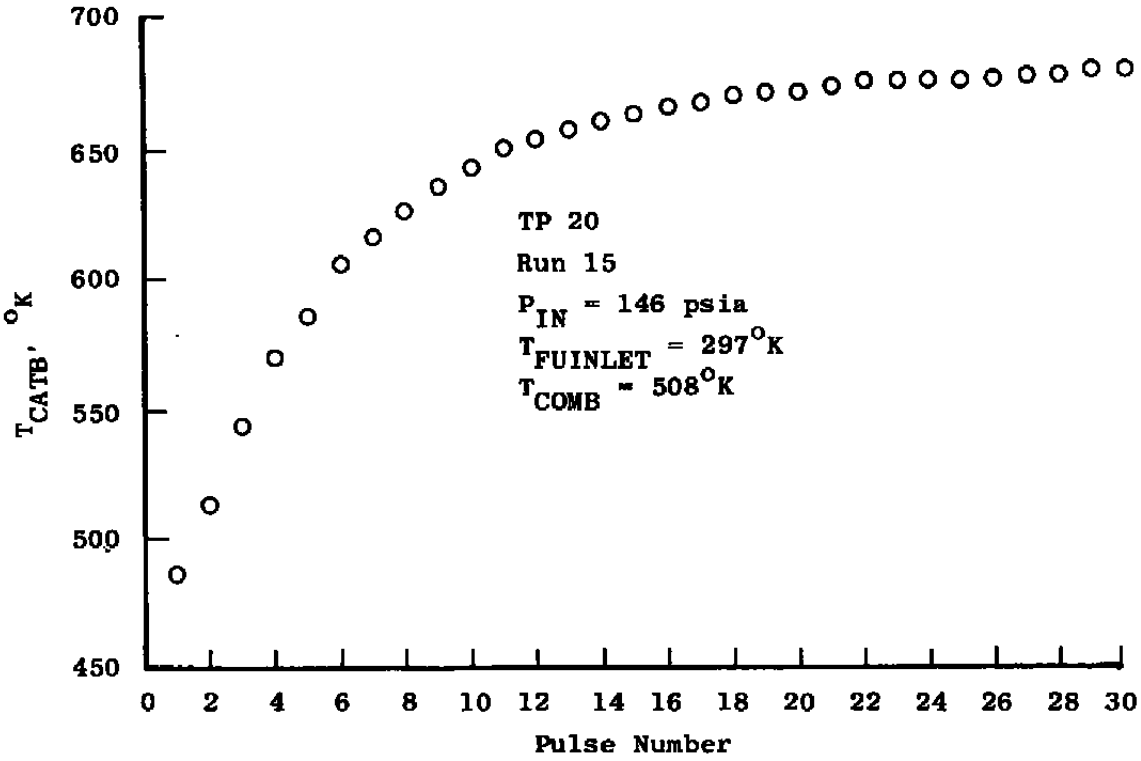

Figure 40. Catalyst bed temperature, T_{CATB}, versus pulse number, TC 2S.

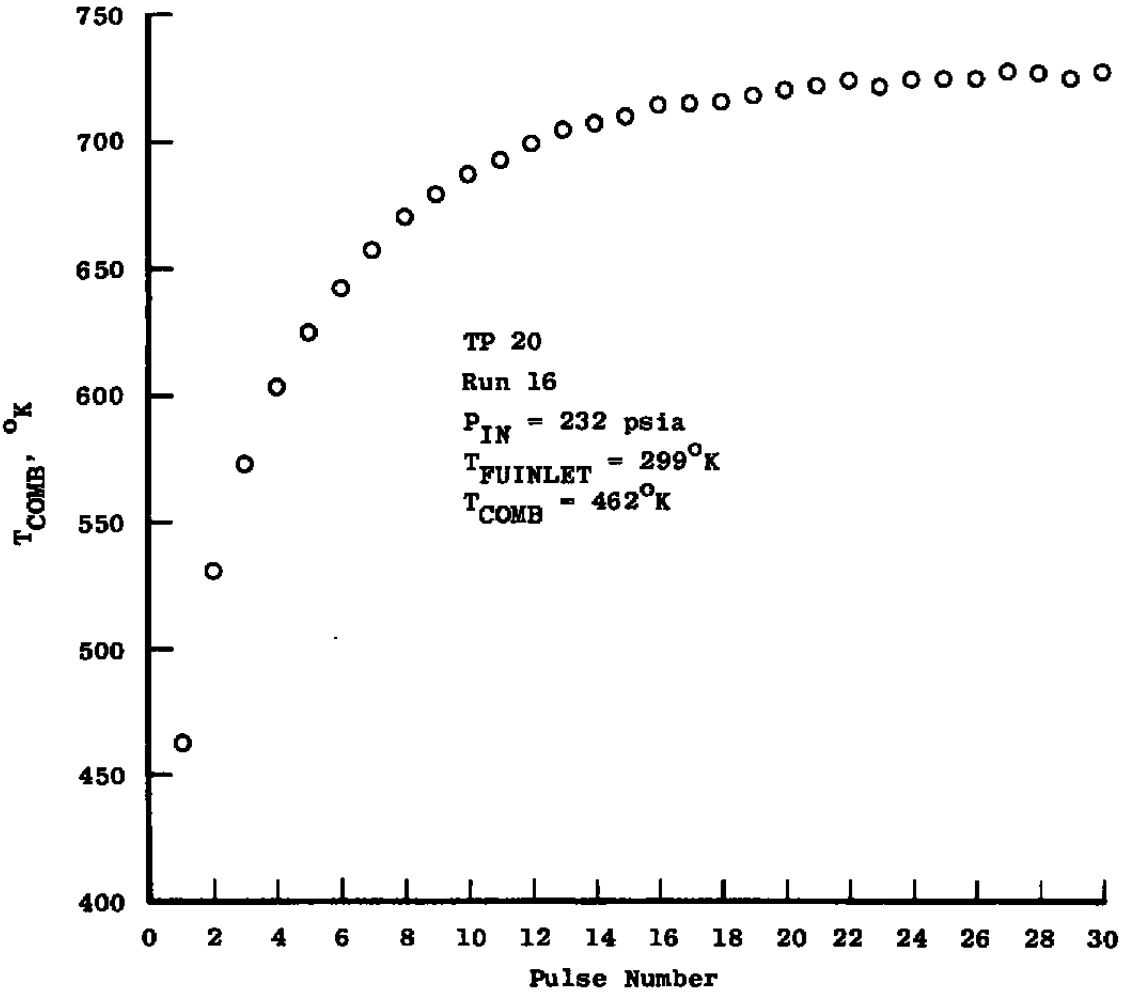

Figure 41. Catalyst bed temperature, T_{COMB}, versus pulse number, TC 2A.

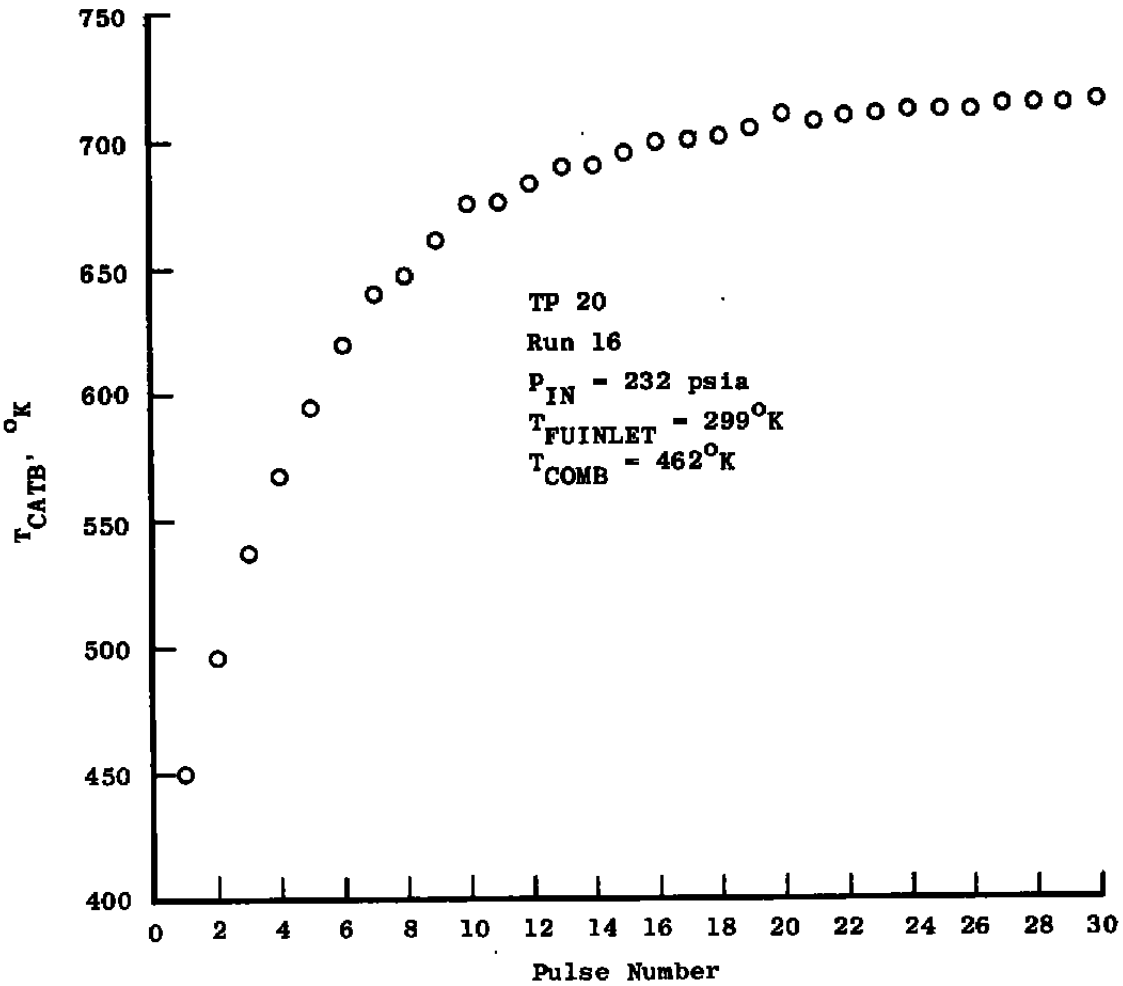

Figure 42. Catalyst bed temperature, T_{CATB}, versus pulse number, TC 2A.

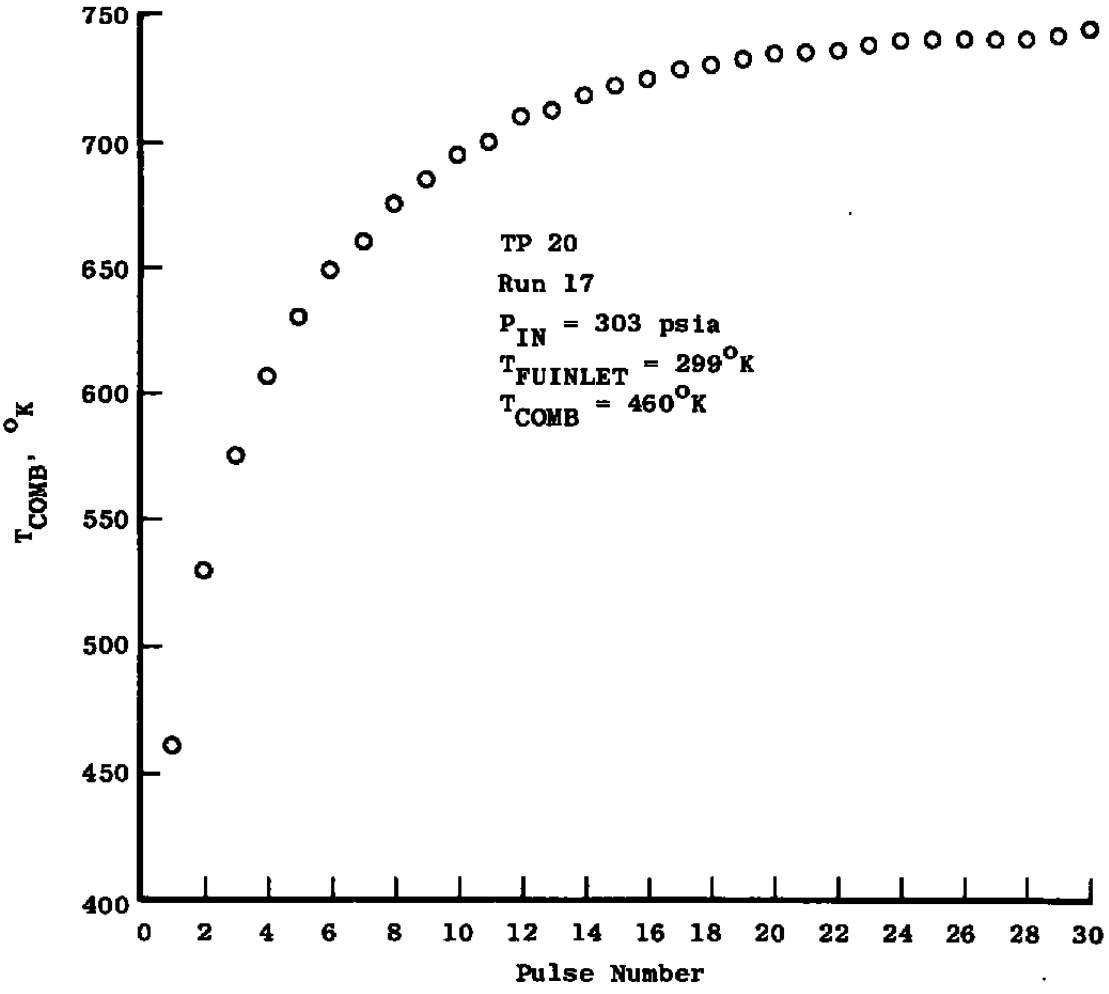

Figure 43. Catalyst bed temperature, T_{COMB}, versus pulse number, TC 2B.

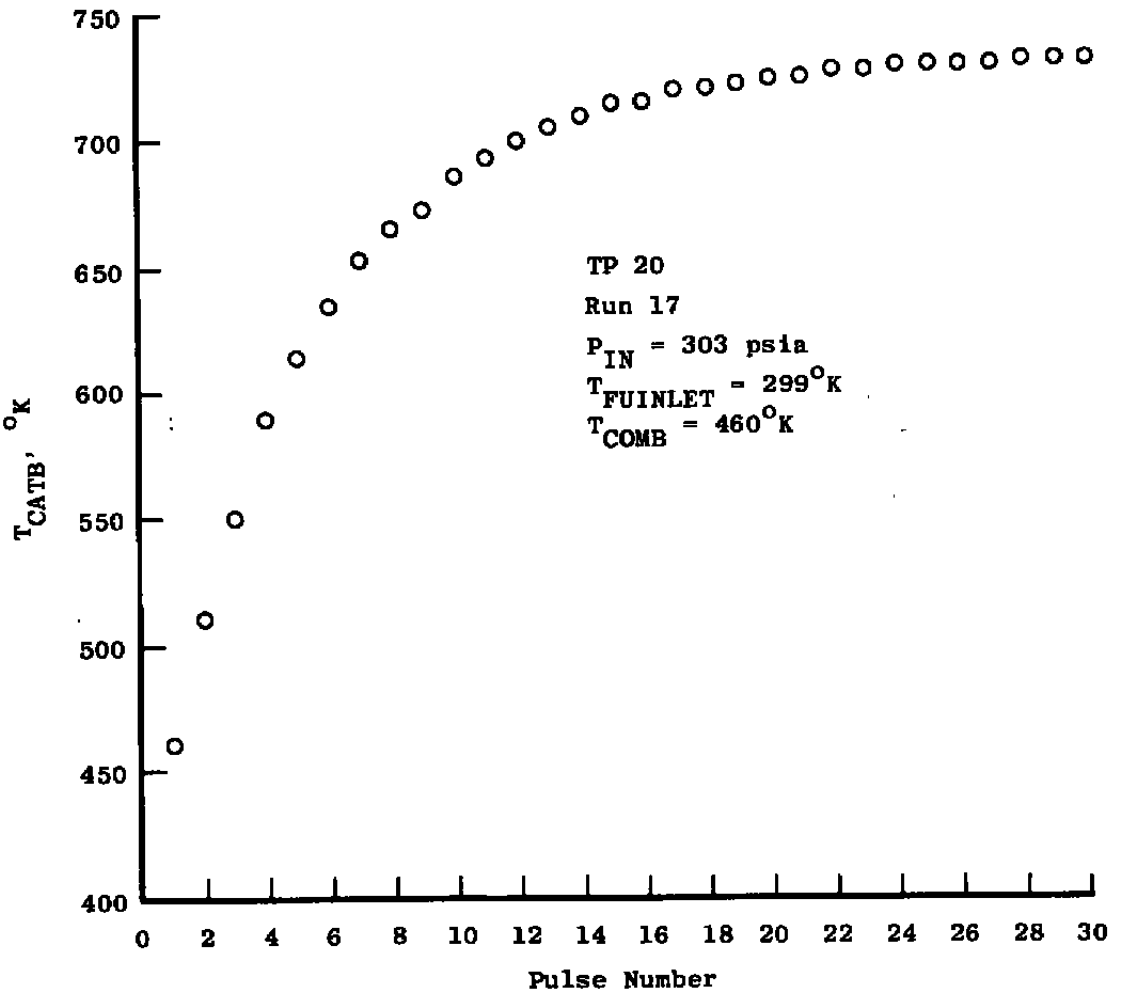

Figure 44. Catalyst bed temperature, T_{CATB}, versus pulse number, TC 2B.

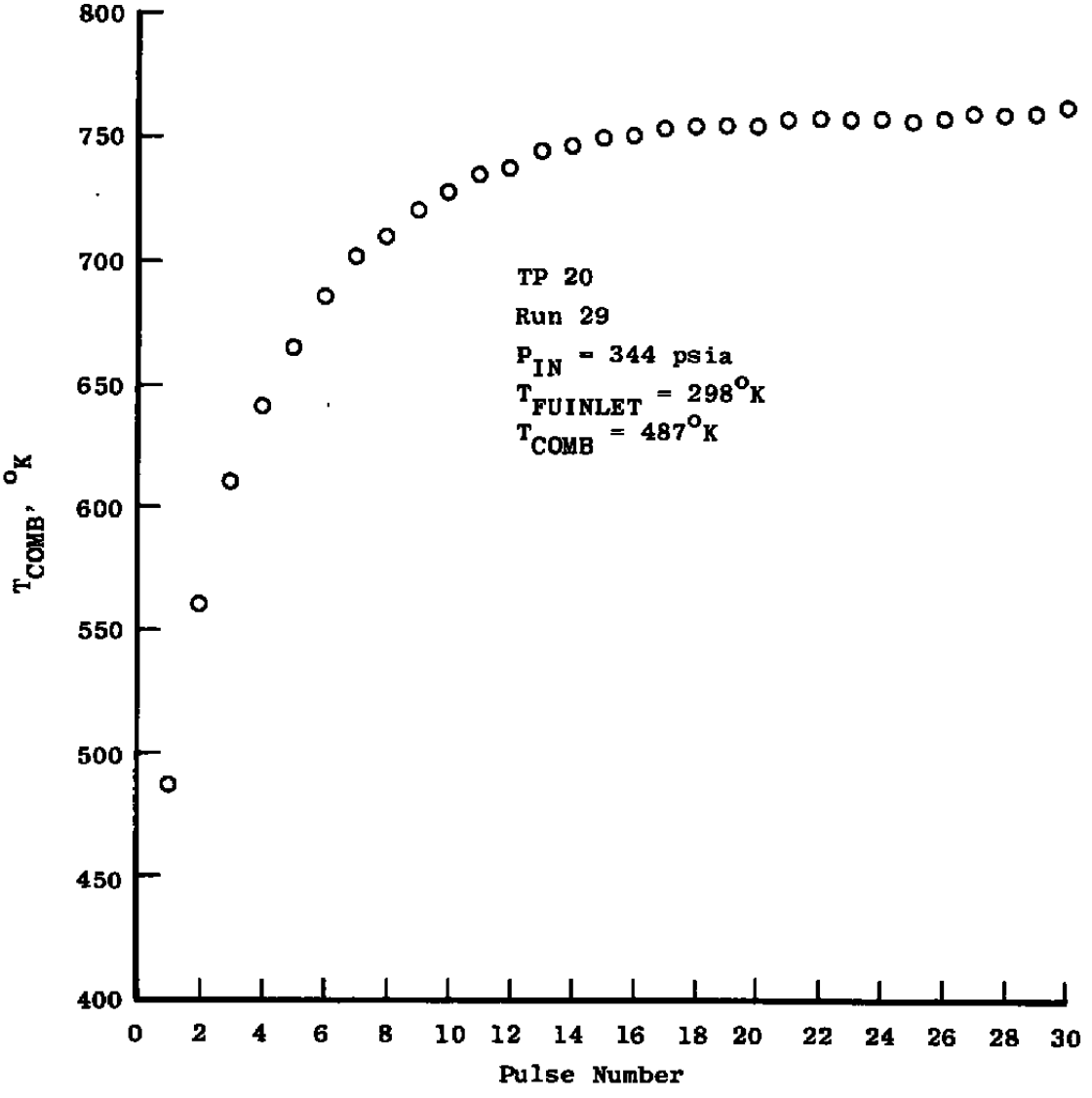

Figure 45. Catalyst bed temperature, T_{COMB}, versus pulse number, TC 2C.

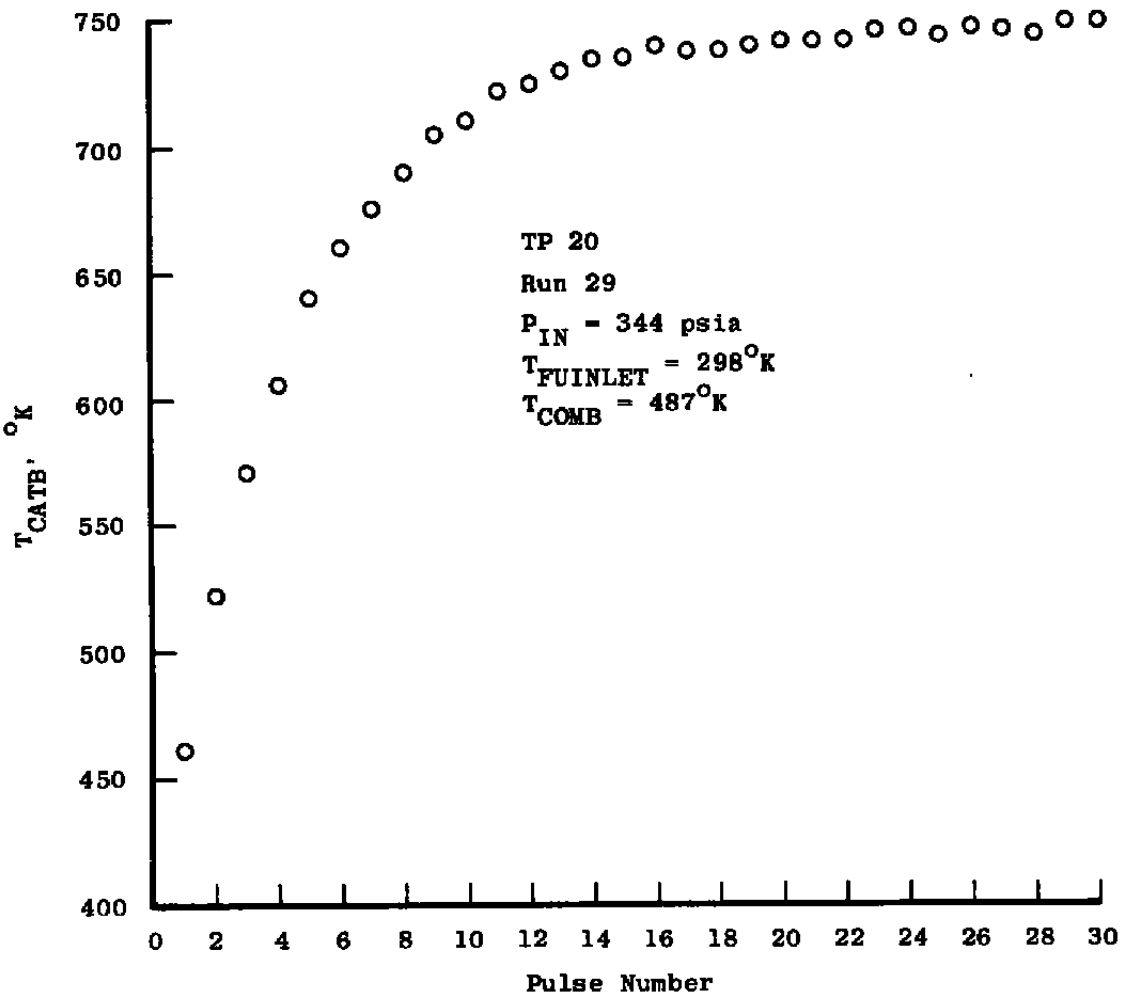

Figure 46. Catalyst bed temperature, T_{CATB}, versus pulse number, TC 2C.

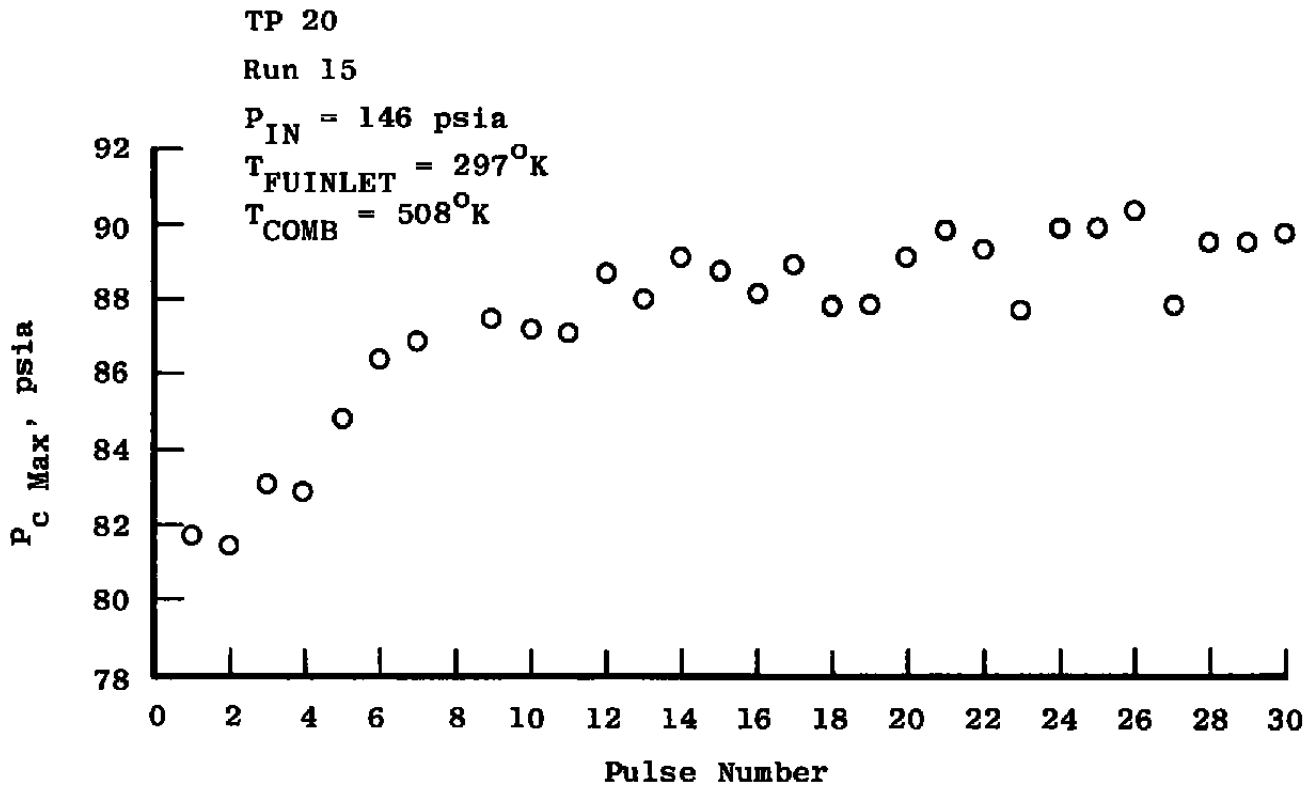

Figure 47. Combustion chamber pressure, P_c, versus pulse number, TC 2S.

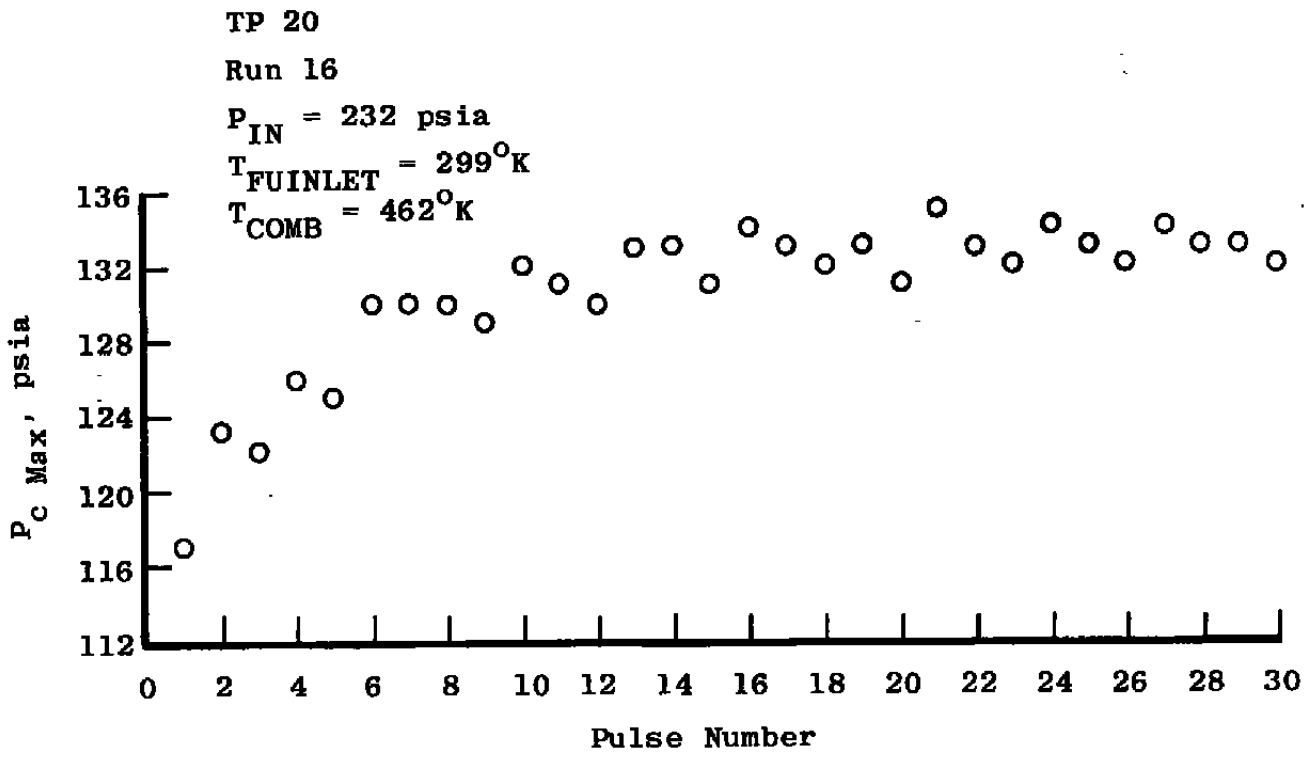

Figure 48. Combustion chamber pressure, P_c, versus pulse number, TC 2A.

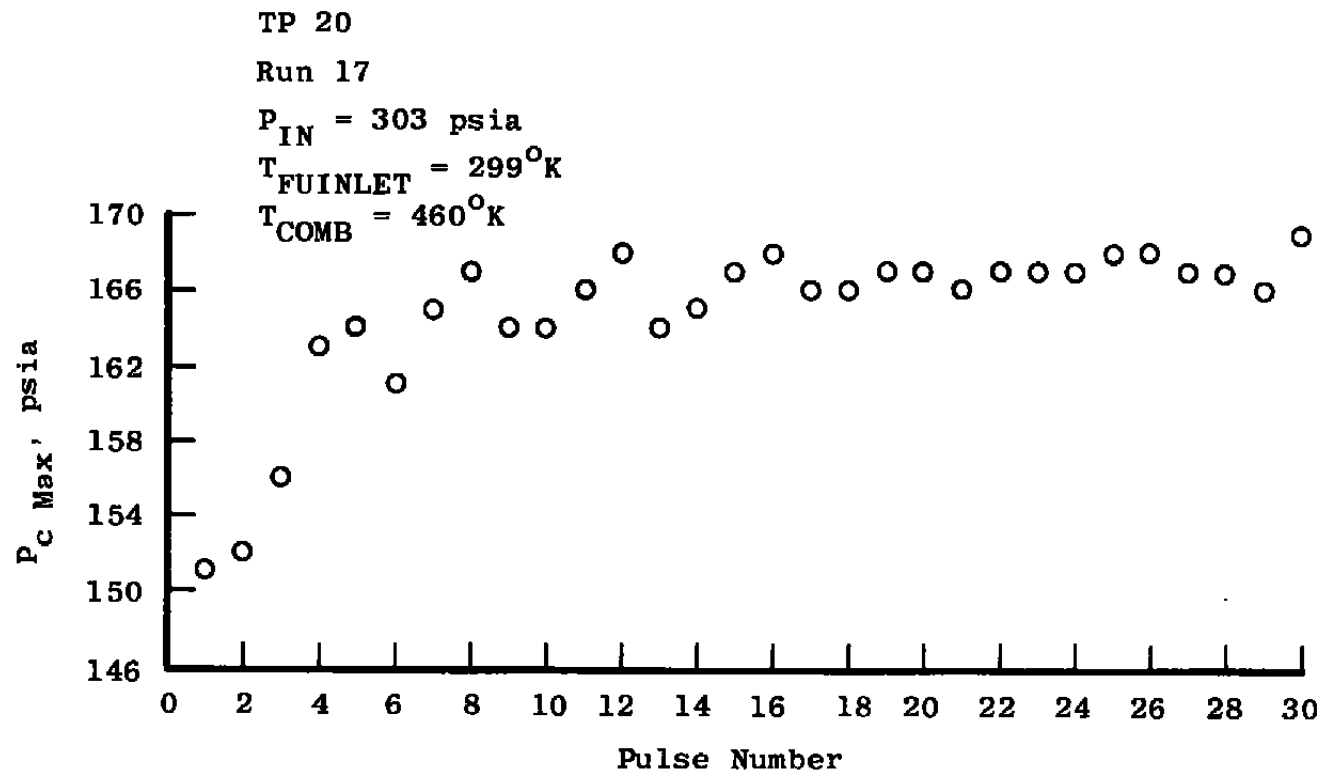

Figure 49. Combustion chamber pressure, P_c, versus pulse number, TC 2B.

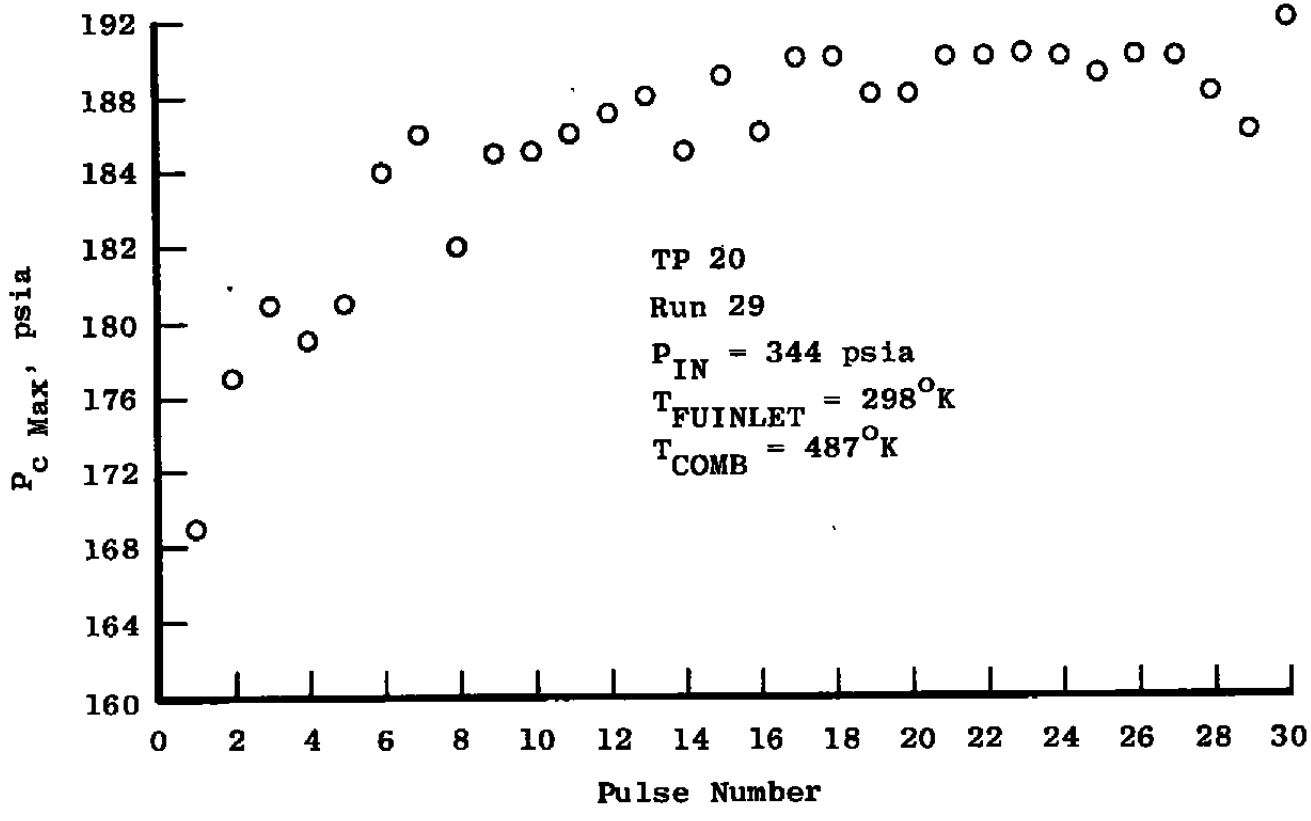

Figure 50. Combustion chamber pressure, P_c, versus pulse number, TC 2C.

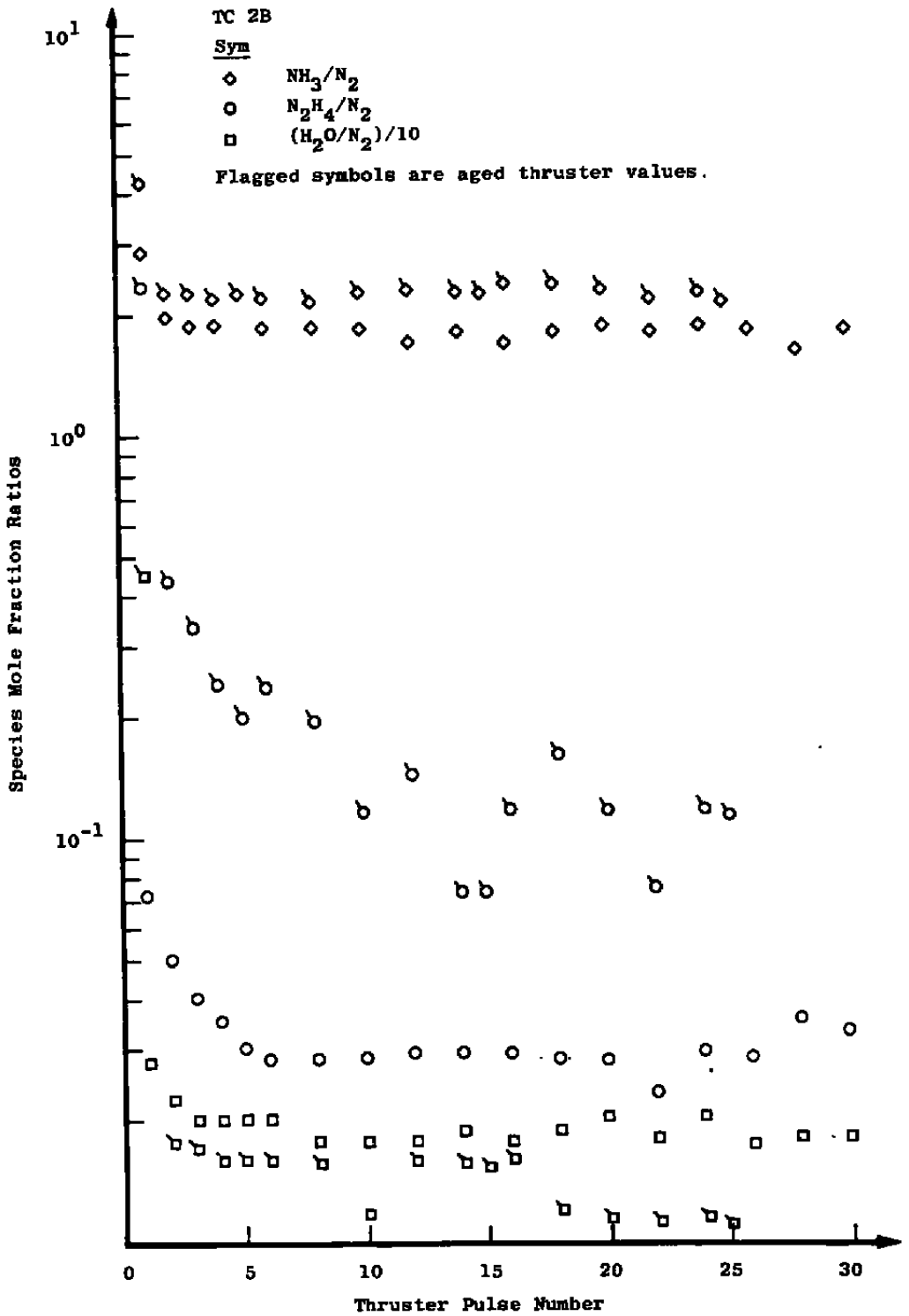

Figure 51. Species mole fraction ratio versus pulse number, TC 2B.

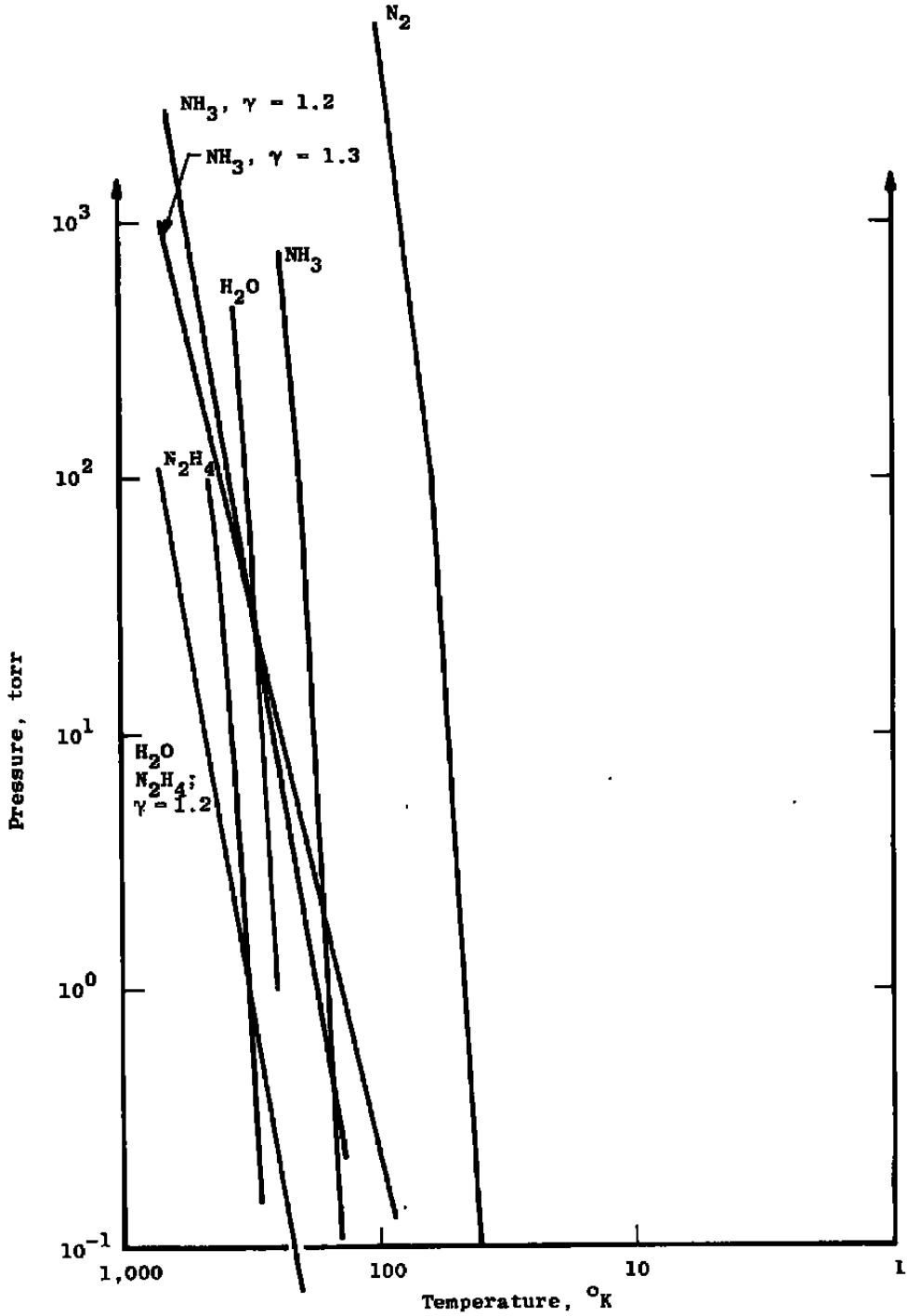

Figure 52. Pressure-temperature diagram of plume centerline expansion.

Table 1. Thruster Test Conditions and Data Matrix

TC	P_{IN}, psia	P_c, psia	Initial T_{CATB}, ^oF	Thrust, lbf	Raman Data Near Exit Plane	Rayleigh Data, Axial Scan	Mass Spectrometer Data	QCM Data
1A	229	135	200	0.165	x	x		
1B	298	175	200	0.212	x			x
1C	344	205	200	0.255	x	x		x
2S	145	85	400	0.1	x	x	x	x
2A	229	135	400	0.165	x	x	x	x
2B	298	175	400	0.212	x	x	x	x
2C	344	205	400	0.255	x	x	x	x

Table 2. Laser-Raman Results

TP	TC	Axial Position x, in.	Axial Position $\hat{x}$	$n(N_2)$, cm^{-3}	$n(H_2)$, cm^{-3}	$n(NH_3)$, cm^{-3}	n_T, cm^{-3}	T_R, ^oK	T_R/T_o	T_o, ^oK	n_o, cm^{-3}	T_{CATB} Initial ^oF
23	2A	0.5	28.5	3.10×10^{16}						726	9.49×10^{19}	400
				4.05×10^{16}								
				4.25×10^{16}								
23	2C	0.5	28.5	4.72×10^{16}						776	1.287×10^{20}	400
				4.50×10^{16}								
24	2S	0.5	28.5	2.70×10^{16}	2.31×10^{16}			153	0.227	675	6.73×10^{19}	400
	2A							163	0.222	734	9.38×10^{19}	
	2C							156	0.201	778	1.2181×10^{20}	
25	2S	0.5	28.5	2.45×10^{16}	2.35×10^{16}	3.30×10^{16}	8.11×10^{16}	148	0.227	653	7.00×10^{19}	400
				2.33×10^{16}								
	2A	0.5	28.5	2.57×10^{16}	2.70×10^{16}	3.89×10^{16}	9.16×10^{16}	153	0.215	710	9.67×10^{19}	400
	2B			3.35×10^{16}						739	1.186×10^{20}	400
	2C			2.71×10^{16}						757	1.326×10^{20}	400
	1A			2.24×10^{16}	2.22×10^{16}					679	1.013×10^{20}	200
	1B			3.19×10^{16}						711	1.226×10^{20}	200
	1C			2.93×10^{16}	3.16×10^{16}					730	1.372×10^{20}	200

Table 3. Average Laser-Raman Results

TC	$n(H_2)/n(N_2)$	$n(N_2)$, cm^{-3}	$n(H_2)$, cm^{-3}	$n(NH_3)$, cm^{-3}	T_R/T_o	n_T/n_o	$n(NH_3)/n(N_2)$
2S	0.936	2.49×10^{16}	2.33×10^{16}	3.30×10^{16}	0.227	1.18×10^{-3}	1.33
2A	1.051	2.57×10^{16}	2.70×10^{16}	3.89×10^{16}	0.215	9.47×10^{-4}	1.51

Table 4. $\hat{I}_{RY}$ Values, TP 25, $\hat{x} = 45.2$

TC	$\hat{I}_{RY}$	T_o, ^oK	n_o, (cm^{-3})	$\gamma = 1.2$ n/n_o
2S	3.71×10^{-3}	653	7.00×10^{19}	4.3×10^{-4}
2A	3.61×10^{-3}	710	9.67×10^{19}	↓
2B	3.04×10^{-3}	739	1.186×10^{20}	↓
2C	2.78×10^{-3}	757	1.326×10^{20}	↓
1A	5.07×10^{-3}	679	1.013×10^{20}	↓
1C	2.49×10^{-3}	730	1.372×10^{20}	4.3×10^{-4}

Table 5. $\hat{I}_{RY}$ Values, TP 26

$\hat{x}$	TC 2S	TC 2A	TC 2B	TC 2C	TC 1A	TC 1B
278.5	3.35×10^{-4}	3.55×10^{-4}	2.32×10^{-4}	1.96×10^{-4}	2.48×10^{-4}	2.17×10^{-4}
211.8	5.34×10^{-4}	4.12×10^{-4}	3.71×10^{-4}	3.80×10^{-4}	4.11×10^{-4}	2.35×10^{-4}
145.2	8.29×10^{-4}	6.38×10^{-4}	5.97×10^{-4}	4.81×10^{-4}	6.51×10^{-4}	3.95×10^{-4}
111.8	1.57×10^{-3}	8.47×10^{-4}	1.26×10^{-3}	9.67×10^{-4}	1.28×10^{-3}	5.95×10^{-4}
78.5	2.08×10^{-3}	1.21×10^{-3}	1.50×10^{-3}	1.68×10^{-3}	1.99×10^{-3}	1.17×10^{-3}
45.2	3.83×10^{-3}	3.10×10^{-3}				
28.5	1.12×10^{-2}	8.14×10^{-3}	8.15×10^{-3}	5.75×10^{-3}	7.98×10^{-3}	4.80×10^{-3}

Table 6. Estimated Data Uncertainties

Rayleigh	Raman	Mass Spectrometer	QCM	QCM
$\sigma(\hat{I}_{RY})$ = ±13 percent	$\sigma(N_2)$ = ±14 percent $\sigma(H_2)$ = ±13 percent $\sigma(NH_3)$ = ±18 percent $\sigma(T_R)$ = ±14 percent	±20 percent	±57 percent	±57 percent

Table 7. Far-Field Ammonia-to-Nitrogen Mole Fraction Ratios.

Pulse Number	TC 2S	TC 2A	TC 2B	TC 2C	Average
1	3.21	3.79	2.84	2.68	3.13
5	2.56	1.61	1.83	1.96	1.99
10	2.28	1.46	1.84	1.80	1.85
20	2.01	1.43	1.84	1.75	1.76
30	1.86	1.60	1.81	1.81	1.77

Table 8. Average Mass Desposition Rates, TC 2S

T_{QCM}, °K	z, in.	x, in.	TP	DR Number	$\langle \dot{m} \rangle 10$, gm/cm^2·sec	θ, deg	cos φ	R^2, cm^2
130	21.21	7.63	20	18	9.76×10^{-6}	19.79	0.984	3.278×10^3
172				28	5.08×10^{-7}			
152				33*	2.05×10^{-6}			
147				34+	3.62×10^{-6}			
144			20	35	3.46×10^{-6}			
125			21	1	2.28×10^{-6}			
				2	2.31×10^{-6}			
				15	1.83×10^{-6}			
				17	3.58×10^{-6}			
	21.21			21	2.55×10^{-6}	19.79	0.984	3.278×10^3
125	13.21			31	1.33×10^{-6}	30.01	1.0	1.501×10^3
144	13.21		21	35	3.66×10^{-7}	30.01	1.0	1.501×10^3
100	21.21		22	1	5.97×10^{-5}	19.79	0.984	3.278×10^3
144	21.21			4	1.57×10^{-6}	19.79	0.984	3.278×10^3
100	13.21			21	5.88×10^{-5}	30.01	1.0	1.501×10^3
		7.63		25	5.92×10^{-5}	30.01	1.0	1.501×10^3
		4.63		26	1.50×10^{-4}	19.32	0.983	1.264×10^3
100		2.63		27	2.11×10^{-4}	11.26	0.947	1.170×10^3
172	13.21	0.63	22	29	7.51×10^{-7}	2.73	0.889	1.128×10^3
144	14.21	7.63	23	42	8.07×10^{-6}	28.23	-1.0	1.678×10^3
	14.21		23	43	8.33×10^{-6}	28.23		1.678×10^3
	13.71		24	2	9.90×10^{-7}	29.10		1.588×10^3
				3	8.13×10^{-7}			
				4	5.85×10^{-7}			
				5	8.43×10^{-7}			
				6	1.10×10^{-6}			
				7	1.03×10^{-6}			
				8	9.06×10^{-7}			
			25	11	9.53×10^{-7}			
				12	1.36×10^{-6}			
				17	1.03×10^{-6}			
				18	9.17×10^{-7}			
				19	7.48×10^{-7}			
	13.71	7.63	25	20	1.06×10^{-6}	29.10		1.588×10^3
	19.52	10.37	26	1	1.15×10^{-6}	27.98		3.152×10^3
	19.52			2	9.50×10^{-7}	27.98		3.152×10^3
	17.52			11	2.13×10^{-7}	30.62	-1.0	2.674×10^3
	15.52			14	3.57×10^{-7}	33.75	0.998	2.248×10^3
	14.52			23	3.22×10^{-7}	35.53	0.995	2.054×10^3
	13.52			29	1.15×10^{-7}	37.49	0.991	1.873×10^3
	12.02			34	2.08×10^{-7}	40.79	0.982	1.626×10^3
	13.52			40	2.87×10^{-7}	37.49	0.991	1.873×10^3
144	12.52	10.37	26	32	5.89×10^{-7}	39.63	0.986	1.705×10^3

* Thruster pulse duration of 0.1 sec with 9.9-sec-off time.

\+ Thruster pulse duration of 0.276 sec with 9.724-sec-off time.

Table 9. Average Mass Desposition Rates, TC 2A

T_{QCM}, °K	z, in.	x, in.	TP	DR Number	$\langle \dot{m} \rangle_{10}$, gm/cm^2-sec	θ, deg	cos ϕ	R^2, cm^2
130	21.21	7.63	20	19	9.76×10^{-6}	19.79	0.984	3.278×10^3
155	↓	↓	↓	32*	2.47×10^{-6}	↓	↓	↓
144				36	5.14×10^{-6}			
125			21	3	3.69×10^{-6}			
125	21.21			18	6.36×10^{-6}	19.79	0.984	3.278×10^3
125	13.21			32	2.54×10^{-6}	30.01	1.0	1.501×10^3
144	↓	7.63		36	1.16×10^{-6}	30.01	1.0	1.501×10^3
↓		1.63		39	9.10×10^{-6}	7.03	0.921	1.143×10^3
		2.63		40	9.73×10^{-6}	11.26	0.947	1.170×10^3
		3.63		42	7.43×10^{-6}	15.37	0.968	1.211×10^3
		4.63		43	5.62×10^{-6}	19.32	0.983	1.264×10^3
		5.63		44	3.74×10^{-6}	23.08	0.993	1.330×10^3
		6.63		45	2.14×10^{-6}	26.65	0.998	1.409×10^3
		7.63		46	1.15×10^{-6}	30.01	1.0	1.501×10^3
	13.21	8.63		47	6.51×10^{-7}	33.16	0.998	1.606×10^3
	14.21	7.63		49	1.36×10^{-6}	28.23	~1.0	1.678×10^3
	15.21	↓		50	1.66×10^{-6}	26.64	0.998	1.868×10^3
	16.21			51	1.76×10^{-6}	25.21	0.996	2.071×10^3
	17.21			52	2.05×10^{-6}	23.91	0.994	2.286×10^3
144	18.21		21	53	1.94×10^{-6}	23.73	0.992	2.515×10^3
100	21.21		22	2	8.20×10^{-5}	19.79	0.984	3.278×10^3
144	21.21			5	2.20×10^{-6}	19.79	0.984	3.278×10^3
↓	20.21			8	2.15×10^{-6}	20.68	0.987	3.011×10^3
	19.21			9	2.20×10^{-6}	21.66	0.989	2.756×10^3
	18.21			10	2.13×10^{-6}	22.73	0.992	2.515×10^3
	17.21			11	2.03×10^{-6}	23.91	0.994	2.286×10^3
	16.21			12	1.96×10^{-6}	25.21	0.996	2.071×10^3
	15.21			13	1.79×10^{-6}	26.64	0.998	1.868×10^3
	14.21			14	1.61×10^{-6}	28.23	~1.0	1.678×10^3
	13.21	7.63		15	1.42×10^{-6}	30.01	1.0	1.501×10^3
	↓	0.63		16	8.57×10^{-6}	2.73	0.889	1.128×10^3
		1.63		17	1.07×10^{-5}	7.03	0.921	1.143×10^3
		2.63		18	1.00×10^{-5}	11.26	0.947	1.170×10^3
		3.63		19	7.64×10^{-6}	15.37	0.968	1.211×10^3
144	13.21	4.63	22	20	6.77×10^{-6}	19.32	0.983	1.264×10^3

* Thruster pulse duration of 0.1 sec with 9.9-sec-off time

Table 9. Concluded

T_{QCM}, °K	z, in.	x, in.	TP	DR Number	$\langle\dot{m}\rangle_{10}$, gm/cm²·sec	θ, deg	cos φ	R^2, cm²
100	13.21	7.63	22	22	8.16×10^{-5}	30.01	1.0	1.501×10^{3}
172	↓	0.63	↓	30	7.28×10^{-7}	2.73	0.889	1.128×10^{3}
↓	↓	2.63	↓	31	1.34×10^{-6}	11.26	0.947	1.170×10^{3}
↓	↓	4.63	↓	32	9.05×10^{-7}	19.32	0.983	1.264×10^{3}
172	13.21	5.63	22	33	4.86×10^{-7}	23.08	0.993	1.330×10^{3}
144	13.71	7.63	23	22	8.77×10^{-6}	29.10	~1.0	1.588×10^{3}
↓	↓	↓	↓	23	9.06×10^{-6}	↓	↓	↓
↓	↓	↓	↓	24	1.56×10^{-5}	↓	↓	↓
↓	13.71	↓	↓	25	1.79×10^{-5}	29.10	↓	1.588×10^{3}
↓	14.21	↓	↓	44	8.59×10^{-6}	28.23	↓	1.678×10^{3}
↓	13.71	↓	↓	47	8.64×10^{-6}	29.10	↓	1.588×10^{3}
↓	↓	↓	23	48	8.57×10^{-6}	↓	↓	↓
↓	↓	↓	24	9	1.59×10^{-6}	↓	↓	↓
↓	↓	↓	↓	10	1.48×10^{-6}	↓	↓	↓
↓	↓	↓	↓	11	1.52×10^{-6}	↓	↓	↓
↓	↓	↓	↓	12	1.41×10^{-6}	↓	↓	↓
↓	↓	↓	↓	13	1.20×10^{-6}	↓	↓	↓
↓	↓	↓	↓	14	1.56×10^{-6}	↓	↓	↓
↓	↓	↓	↓	15	2.44×10^{-6}	↓	↓	↓
↓	13.71	7.63	24	16	1.40×10^{-6}	29.10	↓	1.588×10^{3}
↓	19.52	10.37	26	3	3.50×10^{-7}	27.98	↓	3.152×10^{3}
↓	17.52	↓	↓	10	6.06×10^{-7}	30.62	~1.0	2.674×10^{3}
↓	15.52	↓	↓	15	4.91×10^{-7}	33.75	0.998	2.248×10^{3}
↓	14.52	↓	↓	22	3.58×10^{-7}	35.53	0.995	2.054×10^{3}
↓	13.52	↓	↓	28	3.90×10^{-7}	37.49	0.991	1.873×10^{3}
↓	12.52	↓	↓	33	2.50×10^{-7}	39.63	0.986	1.705×10^{3}
↓	12.02	↓	↓	35	1.95×10^{-7}	40.79	0.982	1.626×10^{3}
↓	11.52	10.37	↓	41	2.22×10^{-7}	41.99	0.978	1.550×10^{3}
↓	↓	3.37	↓	42	1.57×10^{-5}	16.31	0.972	9.29×10^{2}
↓	↓	4.37	↓	43	5.29×10^{-6}	20.77	0.987	9.79×10^{2}
↓	↓	5.37	↓	44	4.33×10^{-6}	24.99	0.996	1.042×10^{3}
↓	↓	6.37	↓	45	1.51×10^{-6}	28.94	~1.0	1.118×10^{3}
↓	↓	7.37	↓	46	1.29×10^{-6}	32.61	0.999	1.207×10^{3}
144	11.52	12.57	26	47	1.68×10^{-7}	47.50	0.954	1.876×10^{3}

Table 10. Average Mass Deposition Rates, TC 2B·

T_{QCM}, °K	z, in.	x, in.	TP	DR Number	$\langle\dot{m}\rangle 10^{7}$, gm/cm^2-sec	θ, deg	cos ϕ	R^2, cm^2
130	21.21	7.63	20	20	1.99 x 10^{-5}	19.79	0.984	3.278 x 10^3
159	↓	↓	20	31	1.80 x 10^{-6}	↓	↓	↓
144			20	37	6.17 x 10^{-6}			
125			21	4	4.91 x 10^{-6}			
↓			↓	5	4.82 x 10^{-6}			
				6	4.66 x 10^{-6}			
	21.21			19	7.45 x 10^{-6}	19.79	0.984	3.278 x 10^3
125	13.21		↓	33	3.54 x 10^{-6}	30.01	1.0	1.501 x 10^3
144	13.21		21	37	1.58 x 10^{-6}	30.01	1.0	1.501 x 10^3
100	21.21		22	3	9;83 x 10^{-5}	19.79	0.984	3.278 x 10^3
144	21.21		22	6	2.51 x 10^{-6}	19.79	0.984	3.278 x 10^3
100	13.21		22	23	9.78 x 10^{-5}	30.01	1.0	1.501 x 10^3
144	14.21		23	45	9.83 x 10^{-6}	28.23	~1.0	1.678 x 10^3
↓	13.71		24	17	1.48 x 10^{-6}	29.10	↓	1.588 x 10^3
	↓		↓	18	1.43 x 10^{-6}	↓		↓
				19	1.37 x 10^{-6}			
				20	1.83 x 10^{-6}			
				21	1.69 x 10^{-6}			
				22	1.99 x 10^{-6}			
				23	1.88 x 10^{-6}			
	↓	↓	24	24	2.04 x 10^{-6}	↓	↓	↓
	13.71	7.63	25	6	1.71 x 10^{-6}	29.10		1.588 x 10^3
	17.52	10.37	26	9	6.34 x 10^{-7}	30.62	~1.0	2.674 x 10^3
	15.52	↓	↓	16	5.07 x 10^{-7}	33.75	0.988	2.248 x 10^3
	14.52			21	8.72 x 10^{-7}	35.53	0.995	2.054 x 10^3
↓	13.52	↓	↓	27	3.71 x 10^{-7}	37.49	0.991	1.873 x 10^3
144	12.02	10.37	26	36	2.93 x 10^{-7}	40.79	0.982	1.626 x 10^3

Table 11. Average Mass Deposition Rates, TC 2C

T_{QCM}, °K	z, in.	x, in.	TP	DR Number	$\langle \dot{m} \rangle_{10'}$, gm/cm^2.sec	θ, deg	cos φ	R^2, cm^2
130	21.21	7.63	20	21	2.16 x 10^{-5}	19.79	0.984	3.278 x 10^3
172	↓	↓	↓	29	9.98 x 10^{-7}	↓	↓	↓
164				30*	1.57 x 10^{-6}			
144			20	38	6.24 x 10^{-6}			
125			21	7	5.36 x 10^{-6}			
↓				8	5.38 x 10^{-6}			
	21.21			20	8.53 x 10^{-6}	19.79	0.984	3.278 x 10^3
125	13.21			34	4.29 x 10^{-6}	30.01	1.0	1.501 x 10^3
144	13.21		21	38	1.68 x 10^{-6}	30.01	1.0	1.501 x 10^3
144	21.21		22	7	2.81 x 10^{-6}	19.79	0.984	3.278 x 10^3
100	13.21		22	24	1.09 x 10^{-4}	30.01	1.0	1.501 x 10^3
144	13.71		23	49	9.57 x 10^{-6}	29.10	-1.0	1.588 x 10^3
↓	↓	↓	23	50	9.85 x 10^{-6}	↓	↓	↓
			24	25	1.58 x 10^{-6}			
			↓	26	2.41 x 10^{-6}			
				27	2.50 x 10^{-6}			
				28	3.22 x 10^{-6}			
				29	3.04 x 10^{-6}			
				30	3.08 x 10^{-6}			
				31	2.08 x 10^{-6}			
			24	32	2.12 x 10^{-6}			
			25	7	1.86 x 10^{-6}			
	13.71	7.63	25	8	2.56 x 10^{-6}	29.10		1.588 x 10^3
	19.52	10.37	26	5	1.14 x 10^{-6}	27.98		3.152 x 10^3
	17.52	↓	↓	8	9.05 x 10^{-7}	30.62	-1.0	2.674 x 10^3
	15.52			17	6.64 x 10^{-7}	33.75	0.998	2.248 x 10^3
	14.52			20	4.10 x 10^{-7}	35.53	0.995	2.054 x 10^3
	13.52			26	5.36 x 10^{-7}	37.49	0.991	1.873 x 10^3
144	12.02	10.37	26	37	3.81 x 10^{-7}	40.79	0.982	1.626 x 10^3

* Thruster pulse duration of 0.1 sec with 9.9-sec-off time.

Table 12. Average Mass Deposition Rates, TC 1A

T_{QCM}, °K	z, in.	x, in.	TP	DR Number	$\langle\dot{m}\rangle 10^{7}$, gm/cm^2.sec	θ, deg	cos ϕ	R^2, cm^2
130	21.21	7.63	20	22	1.50×10^{-5}	19.79	0.984	3.278×10^{3}
172	↓	↓	20	25	3.39×10^{-7}	↓	↓	↓
125			21	9	3.40×10^{-6}			
125	↓		21	10	3.26×10^{-6}	↓	↓	↓
125	21.21		21	23	5.28×10^{-6}	19.79	0.984	3.278×10^{3}
144	13.71		25	9	1.42×10^{-6}	29.10	~1.0	1.588×10^{3}
↓	↓	↓	↓	10	1.51×10^{-6}	↓	↓	↓
				21	1.91×10^{-6}			
				22	1.81×10^{-6}			
	↓	↓	↓	23	1.94×10^{-6}	↓	↓	↓
	13.71	7.63	25	24	1.87×10^{-6}	29.10	↓	1.588×10^{3}
	19.52	10.37	26	6	7.62×10^{-7}	27.98		3.152×10^{3}
	17.52	↓	↓	12	6.07×10^{-7}	30.62	~1.0	2.674×10^{3}
	15.52			18	4.86×10^{-7}	33.75	0.998	2.248×10^{3}
	14.52			24	4.16×10^{-7}	35.53	0.995	2.054×10^{3}
↓	13.52	↓	↓	30	2.91×10^{-7}	37.49	0.991	1.873×10^{3}
144	12.02	10.37	26	38	2.50×10^{-7}	40.79	0.982	1.626×10^{3}

Table 13. Average Mass Deposition Rates, TC 1B

T_{QCM}, °K	z, in.	x, in.	TP	DR Number	$\langle\dot{m}\rangle 10'$, gm/cm^2,sec	θ, deg	cos ϕ	R^2, cm^2
130	21.21	7.63	20	23	2.04×10^{-5}	19.79	0.984	3.278×10^3
172	↓	↓	20	26	8.38×10^{-7}	↓	↓	↓
125	↓	↓	21	11	4.19×10^{-6}	↓	↓	↓
125	21.21	↓	21	12	4.21×10^{-6}	19.79	0.984	3.278×10^3
144	13.71	↓	25	13	1.90×10^{-6}	29.10	~1.0	1.588×10^3
144	13.71	7.63	25	14	1.94×10^{-6}	29.10	~1.0	1.588×10^3

Table 14. Average Mass Deposition Rates, TC 1C

T_{QCM}, °K	z, in.	x, in.	TP	DR Number	$\langle\dot{m}\rangle 10^{7}$, gm/cm^2·sec	θ, deg	cos ϕ	R^2, cm^2
130	21.21	7.63	20	24	2.26×10^{-5}	19.79	0.984	3.278×10^{3}
172	↓	↓	20	27	1.12×10^{-6}	↓	↓	↓
125	↓	↓	21	13	4.94×10^{-6}	↓	↓	↓
125	21.21	↓	21	14	4.86×10^{-6}	19.79	0.984	3.278×10^{3}
144	13.71	↓	25	15	2.29×10^{-6}	19.10	~1.0	1.588×10^{3}
↓	↓	↓	↓	16	2.13×10^{-6}	↓	↓	↓
↓	↓	↓	↓	25	2.98×10^{-6}	↓	↓	↓
↓	↓	↓	↓	26	2.78×10^{-6}	↓	↓	↓
↓	↓	↓	↓	27	2.54×10^{-6}	↓	↓	↓
↓	13.71	7.63	25	28	2.51×10^{-6}	29.10	↓	1.588×10^{3}
↓	19.52	10.37	26	7	9.91×10^{-7}	27.98	↓	3.152×10^{3}
↓	17.52	↓	↓	13	9.43×10^{-7}	30.62	~1.0	2.674×10^{3}
↓	15.52	↓	↓	19	6.00×10^{-7}	33.75	0.998	2.248×10^{3}
↓	14.52	↓	↓	25	5.26×10^{-7}	35.53	0.995	2.054×10^{3}
↓	13.52	↓	↓	31	3.39×10^{-7}	37.49	0.991	1.873×10^{3}
144	12.02	10.37	26	39	5.73×10^{-7}	40.79	0.982	1.626×10^{3}

Table 15. Average Mass Deposition Rates versus Inlet Pressure, T_{QCM} = 125°K, Initial T_{CATB} = 400°F (478°K)

T_{QCM}, °K	z, in.	x, in.	DR Number	$P_{in.}$, psia	$\langle\dot{m}\rangle 10'$, gm/cm^2.sec	θ, deg	cos φ	R^2, cm^2
125	21.21	7.63	24	50	7.47×10^{-7}	19.79	0.984	3.278×10^3
↓	↓	↓	25	100	2.53×10^{-6}	↓	↓	↓
↓	↓	↓	26	150	3.84×10^{-6}	↓	↓	↓
↓	↓	↓	27	200	5.54×10^{-6}	↓	↓	↓
↓	↓	↓	28	250	6.81×10^{-6}	↓	↓	↓
↓	↓	↓	29	300	8.37×10^{-6}	↓	↓	↓
125	21.21	7.63	30	350	9.32×10^{-6}	19.79	0.984	3.278×10^3

Table 16. Averaged QCM Data

TC	T_{QCM}, °K	θ, deg	R^2, cm^2	cos φ	$\langle\dot{m}\rangle_{10}$, gm/cm^2.sec
2S	144	19.79	3.28×10^3	0.984	2.52×10^{-6}
↓	144	-30	-1.54×10^3	-1	9.07×10^{-7}
↓	125-130	19.79	3.28×10^3	0.984	3.72×10^{-6}
↓	125	30.01	1.50×10^3	1.0	1.33×10^{-6}
↓	100	19.79	3.28×10^3	0.984	5.97×10^{-5}
↓	100	30.01	1.50×10^3	1.0	5.90×10^{-5}
2S	172	19.79	3.28×10^3	0.984	5.08×10^{-7}
2A	144	19.79	3.28×10^3	0.984	3.67×10^{-6}
↓	144	-30	-1.54×10^3	-1	1.51×10^{-6}
↓	125-130	19.79	3.28×10^3	0.984	6.60×10^{-6}
↓	125	30.01	1.50×10^3	1.0	2.54×10^{-6}
↓	100	19.79	3.28×10^3	0.984	8.20×10^{-5}
2A	100	30.01	1.50×10^3	1.0	8.16×10^{-5}
2B	144	19.79	3.28×10^3	0.984	4.34×10^{-6}
↓	144	-30	-1.54×10^3	-1	1.70×10^{-6}
↓	125-130	19.79	3.28×10^3	0.984	8.35×10^{-6}
↓	125	30.01	1.50×10^3	1.0	3.54×10^{-6}
↓	100	19.79	3.28×10^3	0.984	9.83×10^{-5}
2B	100	30.01	1.50×10^3	1.0	9.78×10^{-5}
2C	144	19.79	3.28×10^3	0.984	4.53×10^{-6}
↓	144	-30	-1.54×10^3	-1	2.38×10^{-6}
↓	125-130	19.79	3.28×10^3	0.984	1.02×10^{-5}
↓	125	30.01	1.50×10^3	1.0	4.29×10^{-6}
↓	100	30.01	1.50×10^3	1.0	1.09×10^{-4}
2C	172	19.79	3.28×10^3	0.984	9.98×10^{-7}
1A	144	-30	-1.54×10^3	-1	1.74×10^{-6}
↓	130	19.79	3.28×10^3	0.984	1.50×10^{-5}
↓	125	19.79	3.28×10^3	0.984	3.98×10^{-6}
1A	172	19.79	3.28×10^3	0.984	3.39×10^{-7}
1B	144	-30	-1.54×10^3	-1	1.92×10^{-6}
↓	130	19.79	3.28×10^3	0.984	2.04×10^{-5}
↓	125	19.79	3.28×10^3	0.984	4.20×10^{-6}
1B	172	19.79	3.28×10^3	0.984	8.38×10^{-7}
1C	144	-30	-1.54×10^3	-1	2.54×10^{-6}
↓	130	19.79	3.28×10^3	0.984	2.26×10^{-5}
↓	125	19.79	3.28×10^3	0.984	4.90×10^{-6}
1C	172	19.79	3.28×10^3	0.984	1.12×10^{-6}

Table 17. Comparison of Aged and Refurbished Thruster Data Obtained Using Laser-Raman Scattering

TC	$\hat{x}$	$n(N_2)$		$n(H_2)$		T_R/T_o		γ	
		Aged	Refurbished	Aged	Refurbished	Aged	Refb.	Aged	Refb.
2S	28.5	1.4×10^{16}	2.5×10^{16}	2.3×10^{16}	2.3×10^{16}	0.15	0.23	1.26	1.22
2A	28.5	2.3×10^{16}	2.6×10^{16}	3.4×10^{16}	2.7×10^{16}	0.19	0.22	1.26	1.22

Table 18. Plume Mole Fractions Predicted by CONTAM II

N_2	H_2	NH_3	N_2H_4	γ	TC
0.2902	0.1808	0.5287	0.0003	1.199	2S
0.3238	0.2529	0.4217	0.0016	1.218	2A
0.3420	0.2413	0.4136	0.0031	1.217	2B
0.3480	0.2516	0.3904	0.0040	1.222	2C

Table 19. Average Combustion Chamber Number Density and Temperature for the Refurbished Thruster

TC	n_o, cm^{-3}	T_o, °K
2S	6.89×10^{19}	664
2A	9.51×10^{19}	723
2B	1.186×10^{20}	739
2C	1.298×10^{20}	770

Table 20. Comparison of Aged and Refurbished Thruster Rayleigh Scattering Data

Plume	TC	$\hat{I}_{RY}$	MOCS n/n_o, γ = 1.2	MOCS n/n_o, γ = 1.3	f(γ = 1.2)	$\hat{x}$
Aged Thruster	2S	1.04×10^{-1}	5.40×10^{-5}	1.1×10^{-4}	1.92×10^{3}	78.5
Refurbished Thruster	2S	2.08×10^{-3}			3.75×10^{1}	
Simulated Thruster γ = 1.2	2S, $N_2 - NH_3$	6.06×10^{-3}			1.11×10^{2}	
Simulated Thruster γ = 1.2	2S, $N_2 - NH_3 - H_2$	3.94×10^{-3}			7.19×10^{1}	
Simulated Thruster γ = 1.25	2S, $N_2 - NH_3 - H_2$	1.29×10^{-3}	5.40×10^{-5}	1.1×10^{-4}	2.29×10^{1}	78.5
Aged Thruster	2A	4.06×10^{-1}	1.03×10^{-3}	1.3×10^{-3}	3.93×10^{2}	28.5
Refurbished Thruster	2A	8.14×10^{-3}	1.03×10^{-3}	1.3×10^{-3}	6.90	28.5

Table 21. QCM Data Comparison of Averaged $\langle \dot{m} \rangle_{10}$ Values

TC	T_{QCM}, °K	θ, deg	$\langle \dot{m} \rangle_{10}$, gm/cm^2·sec	
			Aged	Refurbished
2S	144	19.8	1.8×10^{-6}	2.5×10^{-6}
2A	144	19.8	2.9×10^{-6}	3.7×10^{-6}
↓	144	30	2.2×10^{-6}	1.5×10^{-6}
↓	125–130	19.8	5.6×10^{-6}	6.6×10^{-6}
↓	125–130	30	3.5×10^{-6}	2.5×10^{-6}
2A	100–104	19.8	6.4×10^{-5}	8.2×10^{-5}
2B	144	19.8	4.0×10^{-6}	4.3×10^{-6}
↓	144	30	3.6×10^{-6}	1.7×10^{-6}
↓	125–130	19.8	6.3×10^{-6}	8.4×10^{-6}
2B	100–104	19.8	8.2×10^{-5}	9.8×10^{-5}
2C	144	30	3.9×10^{-6}	2.4×10^{-6}
2C	125–130	19.8	8.3×10^{-6}	1.02×10^{-5}

NOMENCLATURE

$\tilde{C}_{Pi}$	Constant pressure molar heat capacity for species i
CONTAM II	Computer code for predicting plume contamination from liquid monopropellant and bipropellant rocket engines on spacecraft surfaces
$F(\theta,\phi)$	Scattering cross section function defined by Eq. (3)
f	Rayleigh scattering function defined by Eq. (9)
GHe	Gaseous helium at 20°K
h	Planck's constant
$\hat{I}_{RY}$	Rayleigh scattered intensity normalized to incident laser beam intensity and thruster combustion chamber number density
K	Proportionality constant defined by Eq. (2)
L	Length of observed laser beam
LHe, LN_2	Liquid helium, liquid nitrogen
MOCS	Method of Characteristics Solution
MULTRAN	A subprogram of CONTAM II
$\dot{m},\dot{m}_1$	Mass deposition rate and mass deposition rate of first thruster pulse, respectively; gm/cm^2-sec
$<\dot{m}>_{10},<\dot{M}>_{10}$	Average mass deposition rate of the last 10 pulses of a pulse sequence; gm/cm^2-sec and gm/sec-sr, respectively
N2H4	A subprogram of CONTAM II
n, n_o	Number density and combustion chamber number density respectively, cm^{-3}
n_i	Number density
$\bar{n}_i$	Index of refraction of species i
n_T	Local total number density
$\hat{n}_T$	Ratio n_T/n_o

$n(H_2)$, $n(N_2)$, $n(NH_3)$	Number density of hydrogen, nitrogen, and ammonia, respectively, cm^{-3}
$n_{N_2}^{cal}$	N_2 number density for Rayleigh scattering calibration
P	Total pressure (atmosphere)
P_c, P_o	Thruster combustion chamber pressure, psia
$\bar{P}_o$	Incident power of laser source
P_{IN}	Thruster inlet pressure, psia
QCM	Quartz Cyrstal Microbalance
R	Direct distance from the QCM to the thruster exit plane, cm
R	Universal gas constant
RVC	Research Vacuum Chamber
r_i	Molar refractivity of species i
S_i	Rayleigh scattering photon rate; Eq. (1)
$S_{N_2}^{cal}$	S_{N_2} for calibration condition
T, T_R	Static temperature and rotational temperature, respectively, °K
TC	Thruster test condition
T_{CATB}, T_{COMB}	Catalyst bed lower wall temperature (°F or °K), sometimes designated as T_{clw}
$T_{FUINLET}$	Fuel inlet temperature
T_o	Thruster combustion chamber temperature, °K
TP	Test period
T_{QCM}	Temperature of the QCM surface
X_i	Mole fraction of species i
X^{eq}	Equilibrium degree of dissociation
x	Axial distance from thruster nozzle throat normalized by the diameter of the throat

x	Horizontal distance between QCM and thruster axial centerline, inches axial distance from
z	Axial distance from QCM to thruster exit plane, in.
α_{ie}	Electronic polarizability of species i
γ	Specific heat ratio
δ	A constant for use in the Hill-Draper function (Ref. 5)
ϵ	Degree of dissociation of N_2H_4
θ	Off-axis angular position of the QCM relative to the thruster axial centerline
σ	Estimated data uncertainty
Φ	Defined by Eq. (17a)
ϕ	Mass flux angle of incidence on the QCM surface
σ_i	Rayleigh scattering cross section of species i
$(d\sigma/d\Omega)_i$	Rayleigh scattering differential cross section of species i
χ	Degree of dissociation of NH_3, X^{eq} is equilibrium value
Ω	Solid angle